



Central University of Technology, Free State

**INVESTIGATION ON UPSCALING
SELECTIVE LASER MELTING PROCESS PARAMETERS
USING 17-4PH STAINLESS STEEL POWDER**

MAKOANA NKUTWANE WASHINGTON

Dissertation submitted in fulfilment of the requirements for the degree
MASTER of ENGINEERING in MECHANICAL ENGINEERING

Supervisor: Prof. Ihar Yadroitsau

Co-supervisors: Dr. Heinrich Möller

Dr. Ina Yadroitsava

BLOEMFONTEIN

February 2018

DECLARATION OF INDEPENDENT WORK

I, MAKOANA NKUTWANE WASHINGTON, identity number _____ and student number _____, do hereby declare that this research project submitted to the Central University of Technology, Free State (CUT) for the Master of Engineering in Mechanical Engineering, is my own independent work; complies with the code of academic integrity, as well as other relevant policies, procedures, rules and regulations of the Central University of Technology, Free State; and has not been submitted previously to any institution by myself or any other person in fulfilment of the requirements for the attainment of any qualification.

SIGNATURE OF STUDENT:.....DATE:...../...../.....

ACKNOWLEDGEMENTS

The author would like to express sincere and special gratitude to the following people and organisations:

To the Almighty God for being with me throughout my life, and the strength he granted me to complete my studies. Without him, this study would not have been possible.

To my late mother, Mrs. Tebadi Leah Makoana, my brother, Charane Nicolus Makoana, my sisters, Itumeleng Malope Makoana and Lebongang Mamotalane Makoana, for their love, understanding and moral support they showed towards me during my studies.

To Prof. Ihar Yadroitsau (Igor Yadroitsev) and Dr. Ina Yadroitsava of Central University of Technology, Free State for their meaningful assistance, tireless guidance, patience, advice, valuable comments, suggestions and provisions that benefitted me so much in the completion and success of this study.

To Dr. Heinch Möller of the Council for Scientific and Industrial Research, Pretoria campus, for his support and tireless guidance, and most importantly, for his invaluable comments and suggestions.

To Mr. Danie Louw for the training he gave me on how to assemble and use the high power selective laser melting equipment independently.

And lastly, I would like to thank the Centre for Rapid Prototyping and Manufacturing, the Council for Scientific and Industrial, and the Department of Science and Technology for the important resources provided during this study.

EXECUTIVE SUMMARY

The use of Additive Manufacturing processes, like Selective Laser Melting, is gaining popularity in the manufacturing industry. This is due to its attractive benefits such as high geometrical flexibility and agile response to customisation. Unlike traditional manufacturing processes like casting and forging, which depend on patterns and dies to manufacture the parts, additive manufacturing processes produce parts directly from a three-dimensional computer-aided drawing of the part. The part is built using a laser beam and powder material layer by layer, thus drastically reducing the pre-processing time. Despite all the advantages of Additive Manufacturing, several challenges still remain to be overcome. One major drawback is that the actual production of parts is slow, with jobs taking one week or longer to complete. Therefore, improving the build rates of the current state-of-the-art additive manufacturing machines is inevitable. Literature reveals that the build rates of additive manufacturing processes can be potentially improved by using high-powered lasers with increased focused spot-size diameter in order to melt multiple layers at the same time. This study aims to investigate the aspects of upscaling selective laser melting process parameters on the characteristics of single tracks formed using different parametric combinations. For that purpose, two machines operating at different spot sizes and laser powers were used to produce the single tracks. The surface morphology and melt pool profiles were examined following standard metallographic examination techniques. The hardness was measured on the polished surface of the melt pool and the substrate material. The results obtained show that it is possible to produce continuous tracks using high laser powers and larger spot size. However, it was also observed that the maximum optimal scanning speed is higher when using a smaller spot size, and narrows down when using a larger spot size. There was no significant variation in the hardness of the solidified melt pool for different parametric combinations. Also, the hardness of the solidified tracks was found to be comparable to the hardness of the substrate material.

Table of contents

DECLARATION OF INDEPENDENT WORK.....	i
ACKNOWLEDGEMENTS	ii
EXECUTIVE SUMMARY	iii
LIST OF FIGURES	viii
LIST OF TABLES	xii
GLOSSARY.....	xiii
NOMENCLATURE.....	xiv
CHAPTER 1 - INTRODUCTION.....	1
1.1 Background	1
1.2 Aim and Objectives of the Study	2
1.3 Scope of the Study.....	3
1.4 Research Methodology.....	3
1.5 Expected Contributions	4
1.6 Structure of the Dissertation.....	5
CHAPTER 2 – LITERATURE REVIEW.....	6
Introduction	6
2.1 SELECTIVE LASER MELTING TECHNOLOGY	6
2.1.1 Key Process Parameters.....	7
2.1.2 Lasers in Selective Laser Melting	10
2.1.3 Beam Profiles	13
2.1.4 Physical Phenomena in Selective Laser Melting.....	14
2.1.4.1 Full Melting	15
2.1.4.2 Vaporisation.....	15
2.1.4.3 Marangoni Convection.....	16
2.1.4.4 Plateau-Rayleigh Instability.....	17
2.1.4.5 Wetting.....	18
2.1.4.6 Balling.....	20
2.1.4.7 Epitaxial Solidification and Anisotropy of Properties	20
2.1.4.8 Residual Stresses.....	22
2.2 PRECIPITATION HARDENING 17-4 SS	24

2.2.1 Background.....	24
2.2.2 Effect of Alloying Elements	25
2.2.2.1 Carbon.....	25
2.2.2.2 Silicon	25
2.2.2.3 Manganese	25
2.2.2.4 Phosphorus and Sulphur	25
2.2.2.5 Chromium	26
2.2.2.6 Nickel.....	26
2.2.2.7 Copper.....	26
2.2.2.8 Niobium/Tantalum.....	26
2.2.3 Solidification and Microstructure of 17-4PH Stainless Steel.....	26
2.2.3.1 δ -Ferrite.....	28
2.2.3.2 Retained austenite	28
2.2.3.3 Martensite	28
2.2.3.4 Precipitates.....	29
2.2.4 Heat Treatments and Mechanical Properties of 17-4 PH Stainless Steel	30
2.2.5 Physical Properties of 17-4 PH Stainless Steel	32
2.2.5.1 Density	32
2.2.5.2 Specific heat.....	33
2.2.5.3 Thermal conductivity	34
2.3 SELECTIVE LASER MELTING OF 17-4PH STAINLESS STEEL	34
2.3.1 Single tracks	34
2.3.2 Microstructure	35
2.3.3 Mechanical properties.....	37
2.4 Summary	38
CHAPTER 3 – MATERIALS AND METHODS.....	40
Introduction	40
3.1 Metal Powder Characterisation	40
3.1.1 Particle size distribution	40
3.1.2 Surface morphology	42
3.2 Manufacturing of samples.....	44
3.2.1 Low-power system	45
3.2.2 High-power system.....	46

3.3 Analysis equipment	47
3.3.1 Abrasive cut-off machine	47
3.3.2 Automatic mounting machine	48
3.3.3 Automatic grinding and polishing machine.....	48
3.3.4 Optical microscope	49
3.3.5 Microhardness tester.....	50
3.4 Numerical simulations of molten pool for single laser scan of the substrate.....	50
3.5 Summary	53
CHAPTER 4 – RESULTS AND DISCUSSION.....	54
Introduction	54
4.1 Characterisation of single tracks	54
4.1.1 “No powder” case	54
Low-power system.....	54
High-power system	56
4.1.2 “Powder” case.....	58
Low-power system.....	58
High-power system	60
4.2 Geometrical characteristics <i>versus</i> parameters	62
4.2.1 Width of the track	62
4.2.2 Penetration depth	66
4.2.3 Track height.....	69
4.2.4 Length of molten pool	69
4.3 Hardness <i>versus</i> parameters	70
4.4 Summary	71
CHAPTER 5 –CONCLUSIONS AND FUTURE WORK	73
5.1 Conclusions	73
5.2 Recommendations for future work.....	74
REFERENCES.....	75
APPENDICES	83
Appendix I: Top views of the single tracks “No powder” case.....	84
Appendix II: Top views of single tracks “Powder” case.....	88
Appendix III: Cross-section views of single tracks “No Powder” case	92

Appendix IV: Cross-section views of single tracks “ <i>Powder</i> ” case.....	96
Appendix V	92
Appendix VI.....	101

LIST OF FIGURES

Figure 1: Flow chart of the research methodology.	4
Figure 2: A schematic diagram showing the principle of SLM (Bremen <i>et al.</i> , 2012).	7
Figure 3: Various laser-, geometric- and material factors that have effect on energy input (Dahotre and Harimkar, 2008).	8
Figure 4: Algorithm for finding optimal process parameters for fully dense parts with SLM (Yadroitsev <i>et al.</i> , 2015).	9
Figure 5: Absorption as a function of wavelength for various metals (Kurzynowski <i>et al.</i> , 2012 adapted from Steen and Mazumder, 2010).	10
Figure 6: Schematic of a Yb-fibre laser (Lee <i>et al.</i> , 2017).	13
Figure 7: Intensity distribution of Gaussian beam (Schleifenbaum <i>et al.</i> , 2011).	13
Figure 8: Intensity distribution of top-hat-shaped beam (Schleifenbaum <i>et al.</i> , 2011).	14
Figure 9: Physical phenomena occurring during SLM (Das, 2003).	15
Figure 10: Schematic representation of Marangoni convection during laser melting: (a) flow orientation according to surface tension temperature coefficient; (b) effect of Prandtl number on a negative surface tension temperature coefficient (Mazumder, 1993).....	16
Figure 11: Schematic representation of Rayleigh instabilities: (a) a liquid cylinder in an unperturbed state; (b) inherent instabilities deform the surface of the cylinder, leading to regions of high- and low pressure (highlighted pinched regions have a higher pressure); (c) the cylinder breaks into droplets upon rupture of the pinched regions (Jerrard, 2011).	17
Figure 12: Example of Plateau-Rayleigh instabilities affecting a single line laser scan of M2-117 HSS steel powder (a) 50 W, 5 mm s ⁻¹ ; (b) 50 W, 20 mm s ⁻¹ ; (c) 150 W, 5 mm s ⁻¹ ; (d) 150 W, 20 mm s ⁻¹ (Niu and Chang, 1999).	18
Figure 13: Optical micrographs of Ti6Al4V single scan tracks ($P = 400$ W): (a) 80 mm/s, (b) 120 mm/s, (c) 160 mm/s, (d) 200 mm/s (Shi <i>et al.</i> , 2016).	19
Figure 14: Schematic of isothermal surface wetting: the left side represents low wettability, whereas the right side represents high wettability (Hebert, 2016).	19
Figure 15: Typical balling in SLM (Li <i>et al.</i> , 2012).	20
Figure 16: Spherical cap of a crystal nucleated on a planar substrate from a liquid (Kou, 1987).	21
Figure 17: ECCI image of cross-section of the SLM SS 316L track fabricated at 0.12 m/s, preheating temperature 80 °C (a), EBSD orientation map of the marked region of the track, 22	
Figure 18: Titanium part ripped from the build plate during SLM (https://www.engineering.com/3DPrinting/3DPrintingArticles/ArticleID/15202/7-Issues-to-Look-Out-for-in-Metal-3D-Printing.aspx).....	22
Figure 19: Simple schematic of the cause of residual stresses within SLM (Kempen, 2013). 23	

Figure 20: M2 HSS parts produced with a pre-heating temperature of 90 °C (left), 150 °C (middle), 200 °C (right)	24
Figure 21: Ternary Fe-Cr-C phase diagram at 17% Cr that has phase changes similar to 17-4PH. C ₁ and C ₂ are M ₂₃ C ₆ and M ₇ C ₃ carbides (Wanjara and Jahazi, 2008).....	27
Figure 22: Optical micrograph of ferrite stringers in a martensite matrix of 17-4 PH stainless steel (Facchini, 2010).....	27
Figure 23: Illustration of the transformation from austenite to martensite. “o” indicates the positions of the Fe atoms, “x” indicates the positions available for C atoms (Nishiyama, 1978).	29
Figure 24: Illustration describing martensite laths, blocks and packets (Abrahams, 2010). ...	29
Figure 25: Typical precipitation heat treatment diagram for precipitation hardening alloys (Abrahams, 2010). AC ₃ is the temperature at which transformation of ferrite to austenite is completed during heating.....	31
Figure 26: Density variation of 17-4 PH alloy with temperature (Sabau and Porter, 2008). ..	33
Figure 27: Specific heat of 17-4PH alloy as a function of temperature (Sabau and Porter, 2008).	33
Figure 28: Thermal conductivity of 17-4PH alloy as a function of temperature (Sabau and Porter, 2008).	34
Figure 29: Optical (a) and scanning electron (b) micrographs showing microstructure typical for SLM process and strongly oriented, fine austenite grains in 17-4PH steel (Rafi <i>et al.</i> , 2014).	36
Figure 30: Cross-sectional optical images of SLM 17-4PH; (a) as-built, and (b) heat treated (Yadollahi <i>et al.</i> , 2015).	37
Figure 31: A schematic of a laser diffraction particle size analyser (http://www.shimadzu.com/an/powder/support/practice/p01/lesson22.html)	40
Figure 32: Microtac Bluewave/S3500-SDC particle size analyser.....	41
Figure 33: The particle size distribution of 17-4PH powder.	41
Figure 34: A schematic of a Scanning Electron Microscope (http://www.ammr.org.au/myscope/sem/practice/principles/layout.php).	43
Figure 35: JEOL JSM6010/LA Plus Scanning Electron Microscope.....	43
Figure 36: SEM micrographs showing particle shape at different magnifications.....	44
Figure 37: Design of experiments.....	45
Figure 38: EOSINT M280 SLM system.	46
Figure 39: High-power SLM set-up.....	47
Figure 40: Struers DISOTOM-2 and the cut-off sample.	48
Figure 41: AMP 50 and the mounted sample.	48

Figure 42: Struers TegraPol-25.....49

Figure 43: Olympus BX51M microscope.....49

Figure 44: Schematic diagram showing melt pool profile and geometry.....49

Figure 45: Zwick-Roel ZHV μ microhardness testing machine.....50

Figure 46. Free tetrahedral mesh with refinement region along laser scanning direction...52

Figure 47. Temperature-dependent properties of 17-4PH stainless steel: density (a), thermal conductivity (b), heat capacity (c) (Rack, 1981; Comsol material database, 2015).52

Figure 48: Top view morphologies for the low-power system “no powder” case.....55

Figure 49: Corresponding cross-section views for the low-power system “no powder” case: with ripples on the track (a), with undercut profile (b) and strong humping effect (c).55

Figure 50: Summary of results obtained on the low-power system for “no powder” case.....56

Figure 51: Top view morphologies for the high-power system “no powder” case.....57

Figure 52: Corresponding cross-section views for the high-power system “no powder” case.57

Figure 53: Summary of results obtained on the high-power system “no powder” case.57

Figure 54: Powder layer deposited with the recoating blade.....58

Figure 55: Top view morphologies for the low-power system “powder” case: stable track (a), irregular track (b) and balling effect (b).59

Figure 56: Corresponding cross-section views for the low-power system “powder” case: stable track (a), irregular track (b) and balling effect (c).59

Figure 57: Summary of the results obtained for low-power system for the “powder” case...60

Figure 58: Powder layer deposited with a solid scraper for high-power studies.....60

Figure 59: Top view morphologies for the high-power system “powder” case: stable track (a), irregular track/balling effect (b) and spatter formation (c).....61

Figure 60: – Corresponding cross-section views for the high-power system “powder” case: stable track (a), irregular track/balling effect (b) and spatter formation (c).61

Figure 61: Summary of results obtained on the high-power system “powder” case.62

Figure 62: A depression in the molten pool below high laser beam and spatter formation (Khairallah *et al.*, 2016).62

Figure 63: Calculated effect of scanning speed on the width of the track “no powder” case at different laser power and spot size.....63

Figure 64: Effect of scanning speed on the width of the track “no powder” case for 19.9 kW/mm² (100 W and 900 W laser power).64

Figure 65: Effect of scanning speed on the width of the track “powder” case for 19.9 kW/mm².64

Figure 66: Effect of power density on the width of the track “no powder” case at laser scanning speed $V=1.4$ m/s.....	65
Figure 67: Effect of power density on the width of the track “powder” case at laser scanning speed $V=1.4$ m/s.....	65
Figure 68: Calculated effect of scanning speed on the penetration depth of the molten pool for “no powder” case at different laser power and spot size.....	66
Figure 69: Effect of scanning speed on the penetration depth “no powder” case for 19.9 kW/mm ²	66
Figure 70: Effect of scanning speed on the penetration depth “powder” case for 19.9 kW/mm ²	67
Figure 71: Effect of power density on the penetration depth “no powder” case at laser scanning speed $V=1.4$ m/s.....	67
Figure 72: Effect of power density on the penetration depth “powder” case at laser scanning speed $V=1.4$ m/s.....	68
Figure 73: Effect of interaction time on the penetration depth for “no powder” case.....	68
Figure 74. Length of the molten pool <i>versus</i> scanning speed.....	69
Figure 75: Hardness measurements taken on a cross-section of a single track manufactured using the 80 μ m spot size. $P= 100$ W, $V= 0.5$ m/s, $P_d= 19.9$ kW/mm ² (a) and 240 μ m spot size, $P= 900$ W, $V= 0.9$ m/s, $P_d= 19.9$ kW/mm ² (b).....	70

LIST OF TABLES

Table 1: Lasers for selective laser sintering/melting (Ready and Farson, 2001).....	11
Table 2: Some major manufacturers and types of lasers utilised (Pinkerton, 2016)	12
Table 3: Representative laser for AM (Lee at al., 2017).	12
Table 4: Chemical composition range of 17-4 PH stainless steel (https://www.upmet.com/products/stainless-steel/17-4-ph#Chemical-Properties)	24
Table 5: Standard heat treatment procedures for 17-4 PH stainless steel (ASTM A747, 2004; ASTM A564/A564M, 2004).....	31
Table 6: Minimum properties of 17-4 PH stainless steel, both cast and wrought (ASTM A747, 2004; ASTM A564/A564M, 2004).....	31
Table 7: Available experimental physical properties of 17-4 PH stainless steel (Rack, 1981; Sabau and Porter, 2008; and Koo, 2013).	32
Table 8: Typical mechanical properties of 17-4PH stainless steel manufactured by SLM (Gratton <i>et al.</i> , 2012; Mahmoudi <i>et al.</i> , 2017; Mower and Long, 2016; and EOS, material datasheet_17-PH).....	38
Table 9: Percentiles of the 17-4PH powder (weighted by volume).....	42
Table 10: Parameters employed on the low-power system	45
Table 11: Parameters employed on the high-power system.	46
Table 12: Hardness measurement for different parametric conditions.....	71

GLOSSARY

2D	Two Dimensional
3D-CAD	Three Dimensional-Computer-Aided Drawing
AM	Additive Manufacturing
BCC	Body Centred Cubic
BCT	Body Centred Tetragonal
CSIR, PTA	Council for Scientific and Industrial Research, Pretoria
CUT	Central University of Technology, Free State
DMLS	Direct Metal Laser Sintering
EOS	Electro Optical Systems
FCC	Face Centred Cubic
HV	Hardness Vickers
LENS	Laser Engineering Net Shaping
L-PBF	Laser-Powder Bed Fusion
LYS	Lower Yield Strength
PH	Precipitation Hardening
PSD	Particle Size Distribution
SEM	Scanning Electron Microscope
SLM	Selective Laser Melting
SS	Stainless Steel
UTS	Ultimate Tensile Strength
UYS	Upper Yield Strength

NOMENCLATURE

μ_s	Dynamic viscosity
A	Effective spot size area
C	Specific heat capacity
d	Average diagonal length of the indent
h	Hatch spacing
E	Modulus of Elasticity/Young's Modulus
E_d	Energy density
F	Force
I	Layer thickness
K_s	Thermal conductivity
P	Laser power
P_d	Power density
T_l	Liquidus temperature
T_s	Solidus temperature
T_v	Boiling point
v	Scanning speed
α_L	Mean coefficient of thermal expansion
δ	Delta ferrite
ρ_s	Density
σ_t	Tensile strength
σ_y	Yield strength

CHAPTER 1 - INTRODUCTION

1.1 Background

The issue of climate change, due to emission of greenhouse gases by human activities, is a well-known phenomenon throughout the world. As part of the mitigation strategy, government policies in different countries have been established for the purpose of controlling this effect (*i.e.* greenhouse effect). Industries such as Aerospace and Automotive have been persuaded to adopt measures to produce vehicles that consume fewer combustibles and emit less carbon dioxide. One logical way of minimising gas emissions is by integrating lighter components into the vehicle design. Therefore, design engineers spend a lot of time trying to optimise the geometry of the products during the product design cycle in order to minimise the weight of the final component, while still ensuring that the product will serve its purpose. This process is known as “topology optimisation” and often the final design is complex in terms of geometry.

In traditional manufacturing, such as casting, forging, and machining, complexity is costly. Every complex detail has to be produced through additional tool-path steps to remove undesired or excess material from the raw material. This results in significant material wastage which could lead to environmental issues. Additionally, traditional manufacturing processes require highly skilled operators, which may result in high production costs. Therefore, the extent to which traditional manufacturing processes can produce geometrically complex parts is limited. On the contrary, Additive Manufacturing (AM) processes add little or no extra consideration. Parts can be created that would be impractical or unachievable in other processes.

Selective Laser Melting (SLM), also known as Direct Metal Laser Sintering (DMLS) or Laser-Powder Bed Fusion (L-PBF), is an additive manufacturing (AM) process that utilises a laser beam to selectively melt powder particles in order to produce 3D structures. Additive manufacturing, as the name implies, builds up a part by adding material layer by layer, as opposed to removing material with traditional manufacturing. The AM technique reduces machining time drastically and, in some instances, eliminates it completely, thus substantially reducing material waste and manufacturing time.

The current generation of AM machines enables a wide variety of materials to be processed. Highly complex parts, and even integrated assemblies, can be manufactured. Hence, aerospace

parts are ideal for this process, as modern design allows for iterative, automatically generated geometrically complex structures that are both stronger and lighter than traditional designs. However, this process is optimised for low-volume, high-value production, ensuring that the process is highly attractive for industries such as aerospace.

Despite all the advantages of AM, several challenges must be overcome. One major drawback is that the actual production of big complex parts is quite slow, with jobs taking as much as one week or longer to complete. Its reputation as a fast production process comes from the time gained in pre-processing. By improving the build rates, the cost of AM will be driven down further. High residual stresses provoke structural and physical deformations during SLM processing. However, it was shown that changing process parameters, layer thickness and scanning strategy can reduce residual stresses. Parts produced by new AM methods, such as SLM, have to be tested and verified before use, especially when manufactured at different process parameters. From a hierarchical approach, primary units in SLM are single tracks. Hence, this study aims to investigate the aspects of upscaling SLM process parameters on single tracks.

The choice of 17-4PH stainless steel is industrially driven due to its outstanding combination of high strength, good corrosion resistance and good mechanical properties up to 300 °C.

1.2 Aim and Objectives of the Study

The aim of this study is to investigate the aspects of upscaling SLM process parameters on the process stability and mechanical properties. The specific technical objectives are summarised as follows:

- 1.2.1 Study the surface morphology of single tracks produced using different parametric combinations (i.e. laser power, scanning speed and spot size);
- 1.2.2 Analyse unfavourable effects such as inconsistent melt pool formation, humping and balling effect (spheroidization of the melt pool and formation of beads);
- 1.2.3 Measure geometrical characteristics of single tracks (i.e. width, penetration depth, and height) to investigate the effect of laser power, scanning speeds and spot size on the solidified melt pool;
- 1.2.4 Study the effect of laser power, scanning speed and spot size on the microhardness of the solidified melt pool;
- 1.2.5 Identify opportunities of increasing the SLM process efficiency.

1.3 Scope of the Study

The scope of work covered in this study includes:

- 1.3.1 Determination of powder characteristics of the 17-4PH powder at CSIR, PTA;
- 1.3.2 Conducting experiments on the low laser power (50–300 W) SLM system at CUT;
- 1.3.3 Conducting experiments on the high laser power (900–2700 W) SLM system at CSIR, PTA;
- 1.3.4 Metallographic examination and microhardness measurements at CSIR, PTA.

1.4 Research Methodology

The research methodology adopted in this study is briefly described below and depicted in Figure 1.

1. Reviewing the literature on the principles of SLM technology and the phenomena thereof; metallurgical background on 17-4PH stainless steel including chemical makeup, solidification and microstructure, physical and mechanical properties; and lastly, SLM of 17-4PH stainless steel.
2. Characterising the powder material used by applying laser diffraction technique and scanning electron microscopy.
3. Design of experiments using the experimental approach.
4. Numerical simulation of molten pool at chosen process parameters.
5. Sample preparation and examination using standard metallographic techniques.
6. Hardness measurements using Vickers microhardness testing machine.

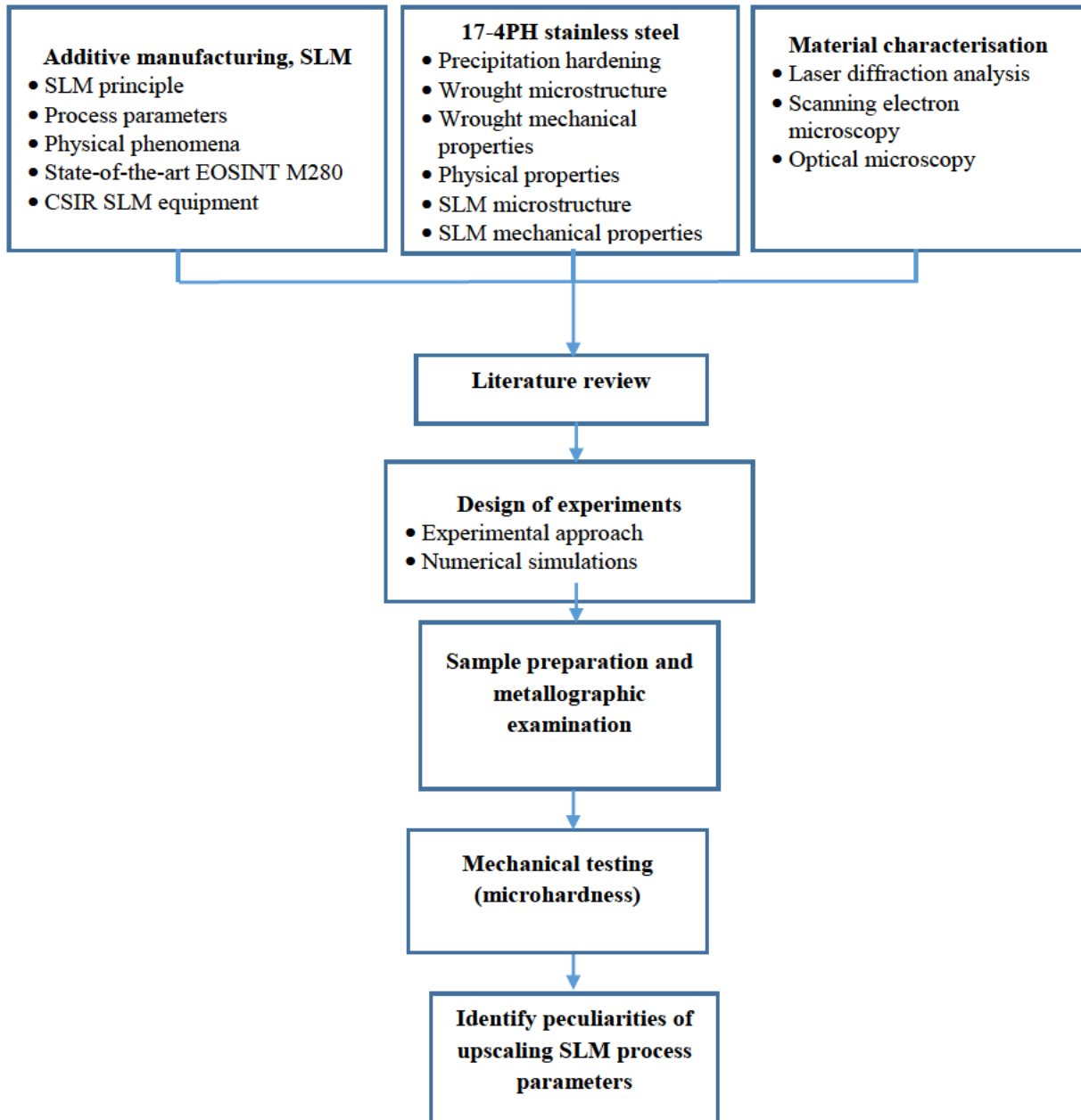


Figure 1: Flow chart of the research methodology.

1.5 Expected Contributions

This study will contribute to the existing body of knowledge by:

1. Generating data that can be used to inform decisions on upscaling of SLM process parameters.
2. Identifying the limitations and opportunities of improving the SLM process efficiency via the build rate.

1.6 Structure of the Dissertation

This dissertation comprises five chapters, the introduction being the first chapter. The background, objectives and the research methodology are presented in this chapter. The remaining chapters are organised as follows:

- Chapter 2 presents the literature review relating to the study. The basic knowledge on different topics related to this study is presented. The topics covered are: principles of SLM; key process parameters in SLM; type of lasers used in SLM; physical phenomena; microstructure and mechanical properties of traditional 17-4PH stainless steel. Literature on SLM of 17-4PH stainless steel is also reviewed.
- In Chapter 3, the materials used and the experimental methodology adopted are presented. The equipment used for material characterisation, single track formation, sample preparation and examination are fully described in this chapter. Method and material properties for numerical simulation are also presented.
- Chapter 4 presents the results obtained and a discussion on the characterisation of the single tracks formed. The effects of process parameters on the surface morphology and melt pool profile are analysed and discussed. The main effects are also presented with graphs. The simulation results are used to estimate the molten pool size and shape and to describe instabilities in the formation of single tracks during laser melting. Lastly, the effect of process parameters on the microhardness is presented and discussed.
- Chapter 5 summarises the results, and draws conclusions. Recommendations for future work are also made in this chapter.

CHAPTER 2 – LITERATURE REVIEW

Introduction

This chapter presents a literature review on the principles of SLM, starting from the building process, key process parameters, types of laser used in SLM. The physical phenomena, metallurgical background information on traditional 17-4PH stainless steel, traditional microstructures and mechanical properties are investigated. Lastly, a review on SLM of 17-4PH stainless steel is presented.

2.1 SELECTIVE LASER MELTING TECHNOLOGY

Selective Laser Melting (SLM), also known as Direct Metal Laser Sintering (DMLS) or Laser Powder Bed Fusion (L-PBF), is one of the AM technologies. These names are used interchangeably to refer to the same process that uses a high-powered laser beam as a source of energy to melt powder particles. This is done in order to build 3D structures layer by layer directly from a 3D CAD model. The process starts by generating a 3D CAD model of the part. The model is sliced into 2D layer mode and transferred into the machine. The powder is deposited by a scraper, rake, brush or roller moving over the powder bed, followed by a laser beam that scans the deposited layer. Upon completion, the building platform is lowered by a one-layer thickness and a new powder layer is deposited on top of the previously solidified layer. The process is repeated until the part is finished (Figure 2).

The building process usually takes place inside a tightly controlled inert atmosphere to avoid oxidation. Typically, the finished part is surrounded by infusible loose powder which can be removed. Post-processing of the finished part can include stress-relieving, annealing, machining or different surface treatments such as sandblasting and polishing (Seifi *et al.*, 2016). SLM is a still-maturing technology which offers great potential for manufacturing of geometrically complex-, valued-added-, and customer-oriented products. Because of the advantages offered by AM processes, many researchers across the world anticipate that this manufacturing technique will become a major player in the next industrial revolution. Research efforts have already been initiated to realise the potential for practical use of this technology in various domains such as automotive, biomedical, and energy applications (Bremen *et al.*, 2012).

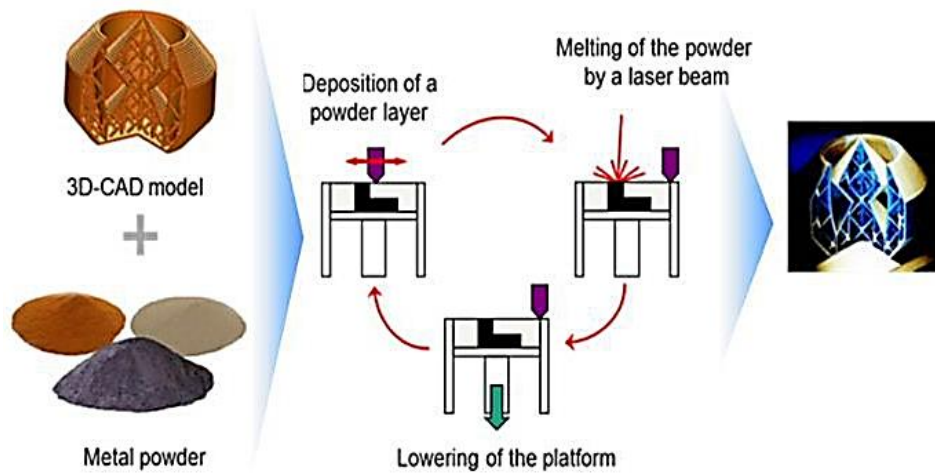


Figure 2: A schematic diagram showing the principle of SLM (Bremen *et al.*, 2012).

2.1.1 Key Process Parameters

During scanning, laser radiation transfers energy by electromagnetic waves to powder material. The interaction time of the laser beam with the powder depends on the scanning speed and the size of the spot of the laser beam. Thus, the result of scanning depends on the properties of material, laser power, scanning speed, spot size, *i.e.* on process parameters. These parameters are either controllable or predefined. Controllable parameters are those which control the heating, melting and solidification process (*i.e.* laser power, scan speed, beam diameter, layer thickness, *etc.*). Predefined parameters are also related to the process but cannot be changed during scanning (*i.e.* powder particle size distribution, absorptivity, reflectance, *etc.*). The final properties, such as geometry and mechanical properties of an SLM part, depend on the energy input, powder layer thickness, scanning and building strategies (Dahotre and Harimkar, 2008; Kruth *et al.*, 2003; Mani *et al.*, 2015). Figure 3 shows that different geometric-, laser- and material parameters affect the energy input. It should be noted that most of these parameters are strongly interdependent and are mutually interacting.

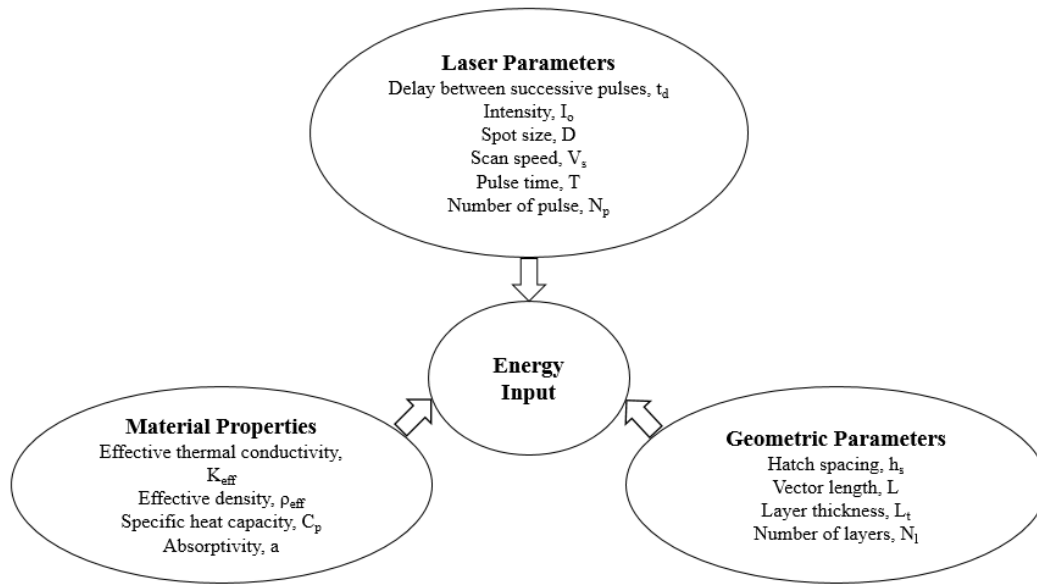


Figure 3: Various laser-, geometric- and material factors that have effect on energy input (Dahotre and Harimkar, 2008).

In SLM, the popular approach is that the production of a fully dense material goes through the proper combination of the four main process parameters as shown in Equation 1 (Mani *et al.*, 2015; Facchini, 2010; and Ciurana *et al.*, 2013):

$$E_d = \frac{P}{v \times h \times l} \dots \dots \dots \text{Equation 1}$$

- Where
- E_d – Total energy input per volume of each melted track (J/mm³)
 - P – Laser Power (W)
 - v – Scanning speed (mm/s)
 - h – Hatch spacing (mm)
 - l – Thickness of the single layer (mm)

Other approaches, such as systematic analysis of SLM parameters, are necessary to control the final product quality on every level – tracks and layers (Yadroitsev *et al.*, 2015). It was shown that to produce a continuous and stable single track, optimum laser power, laser spot size and scanning speed for different powder layer thicknesses must be used (Figure 4).

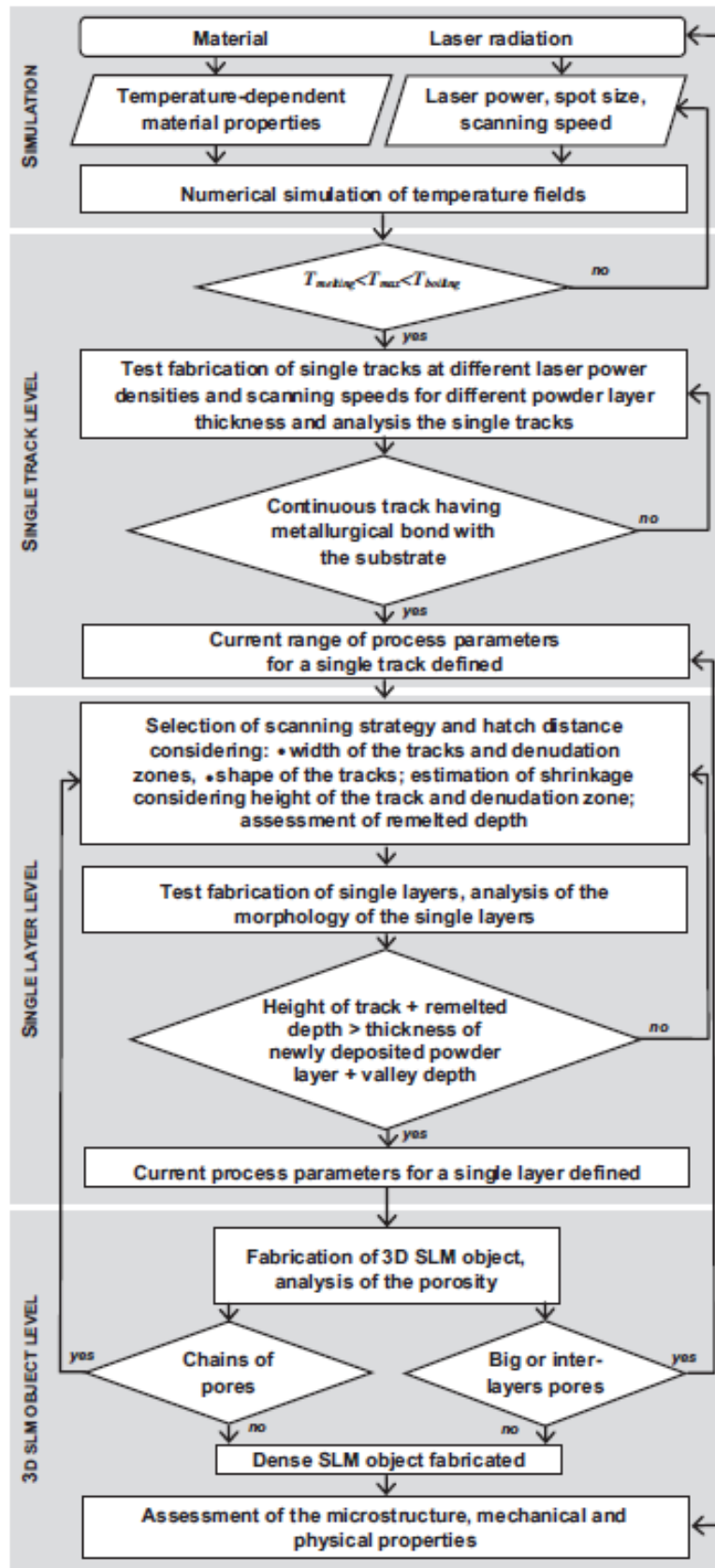


Figure 4: Algorithm for finding optimal process parameters for fully dense parts with SLM (Yadroitsev *et al.*, 2015).

The powder layer thickness has to be chosen in respect to the particle size of the powder used. The geometric characteristics of the tracks affect the choice of subsequent scanning strategies and hatch distances. Choosing a scanning strategy defines the layer's morphology, which in turn affects the subsequent layer thickness, regularity and continuity. The high quality of the synthesised single layer should guarantee that the thickness of the next powder layer deposited does not vary greatly, preventing further irregularity and balling effect. Numerical simulation of the temperature fields and analysis of pore shapes could provide comprehensive information to determine the optimal process parameters for manufacturing non-porous 3D DMLS objects (Yadroitsev *et al.*, 2015).

2.1.2 Lasers in Selective Laser Melting

One of the key elements in the SLM process is the selection of the type of laser radiation source. This is important because of the varied parameters of the energy absorption of different materials, mainly dependent on the wavelength of the laser source, as shown in Figure 5. CO₂ and Nd:YAG-lasers were commonly used in laser sintering/melting systems, with infrared (IR) fibre gaining popularity in recent years. CO₂ lasers have better absorption for sintering polymer powder, while lasers with wavelengths close to 1 μm, such as Nd:YAG and IR fibre lasers, are better suited for carbide ceramics and metals (Kruth *et al.*, 2003). Ready and Farson (2001) tabulated lasers for selective laser sintering/melting systems, showing the wavelength and advantages and disadvantages of each type (Table 1).

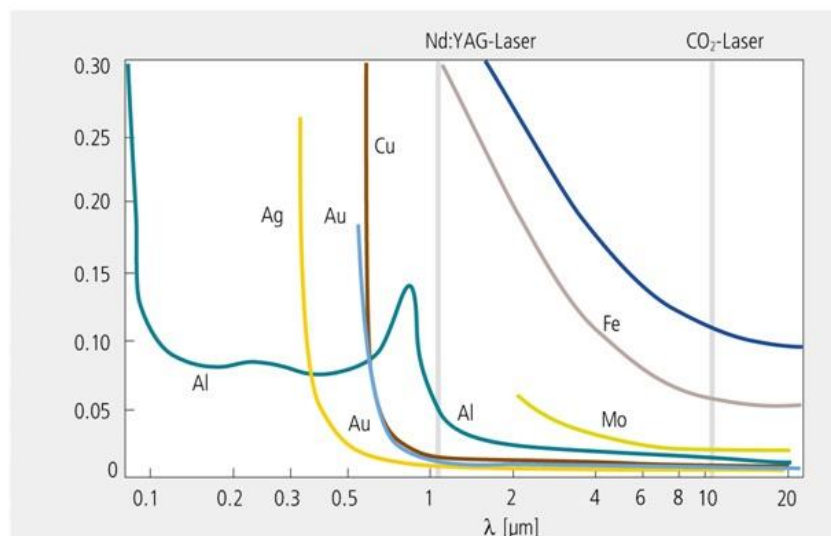


Figure 5: Absorption as a function of wavelength for various metals (Kurzynowski *et al.*, 2012 adapted from Steen and Mazumder, 2010).

Table 1: Lasers for selective laser sintering/melting (Ready and Farson, 2001)

Lasers	Wavelength (µm)	Advantages	Disadvantages
CO ₂	10.6	Low price/watt; fairly efficient; couples well with most materials; commonly available	Long wavelength requires semi-fragile optics and make large focus spot; harder to power control
Nd:YAG	1.064	couples well with metals; commonly available	High price/watt; does not couple well with most plastics; generally poor beam quality
NIR (Near-Infrared diode)	0.7-1.6	Easy power control; very efficient	Very poor beam quality
Fibre	1.55	Easy power control; easy to scale; excellent beam quality	
MIR (Mid-Infrared) SS/OPO	3-5	Combines advantages of CO ₂ and Nd:YAG laser	Output power low; under development

The development of AM systems into user-friendly, commercial units, plus the need for safety, means the type of laser installed is not always obvious. To clarify exactly which types of lasers are used in modern powder bed fusion system, Table 2 lists some systems and their lasers. It is clear that modern AM systems used to manufacture metallic parts are equipped with Yb-fibre lasers. Table 3 further shows the advantages of Yb-fibre laser over the other types of lasers.

A fibre laser is a laser in which the active gain medium is a rare-earth doped optical fibre. Amongst the various rare-earth doped gain fibres, Yb-fibres are most suitable for high power generation because of high quantum efficiency. This high quantum efficiency is the very reason why Yb-fibre lasers are widely used in material processing and have mostly replaced Nd:YAG lasers in SLM. They are pumped by the laser diodes in 950–980 nm wavelength and produce near-infrared laser beams in 1030–1070 nm output wavelength (Pinkerton, 2016; Lee *et al.*, 2017). Other advantages, due to the fibre-based gain medium and optical components, are high electrical-to-optical efficiency (~25%), excellent beam quality, robustness against environmental disturbances and system compactness. Figure 6 shows a schematic of a Yb-fibre laser.

Table 2: Some major manufacturers and types of lasers utilised (Pinkerton, 2016)

Manufacturer:systems	Laser
3D Systems Inc: ProX, sPro and ProX SLM systems	30–200 W CO ₂ laser (for thermoplastics) 50–500 W Yb-fibre laser (for metals)
EOS GmbH: EOSINT, EOS M and PRECIOUS M machines	30 W, 70 W or 2 x 50W CO ₂ lasers (for thermoplastics) 200W–1 kW Yb-fibre laser (for metals)
SLM Solutions GmbH: SLM systems	400 W–2x 1000 W Yb-fibre laser (for metals)
Renishaw: AM250	200 W or 400 W Yb-fibre laser

Table 3: Representative laser for AM (Lee at al., 2017).

Laser	CO₂ laser	Nd:YAG laser	Yb-fibre laser
Application	SLA, SLM, SLS, LENS	SLM, SLS, LENS	SLM, SLS, LENS
Operation wavelength	9.4 & 10.6 μm	1.06 μm	1.07 μm
Efficiency	5-20%	Lamp pump: 1-3% Diode pump: 10-20	10-30%
Output power (CW)	Up to 20 kW	Up to 16 kW	Up to 10 kW
Pump source	Electrical discharge	Flash lamp or laser diode	Laser diode
Operation mode	CW & Pulse	CW & Pulse	CW & Pulse
Pulse duration	Hundreds ns-tens μs	Few ns-tens ms	Tens ns-tens ms
Beam quality factor (mm.mrad)	3-5	0.4-20	0.3-4
Fibre delivery	Not possible	Possible	Possible
Maintenance period	2000 hrs	200 hrs (Lamp life) 10,000 hrs (Diode life)	Maintenance free (25,000 hrs)

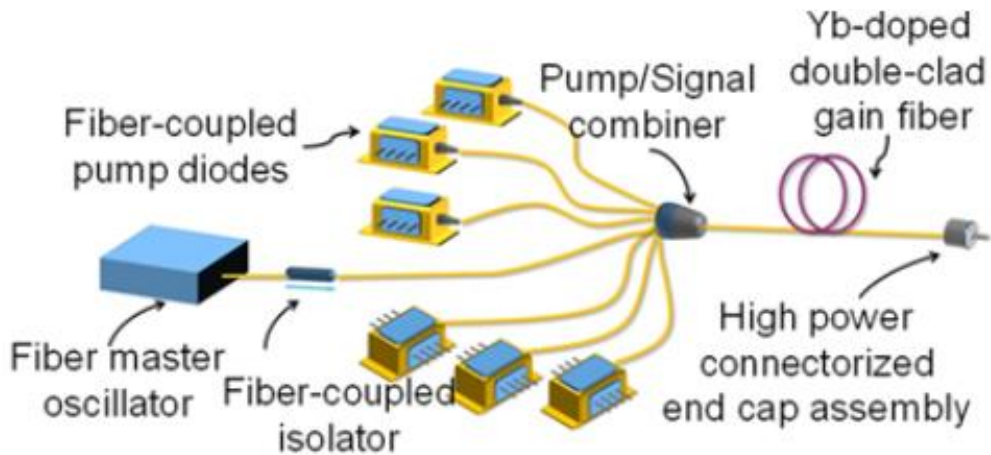


Figure 6: Schematic of a Yb-fibre laser (Lee *et al.*, 2017).

2.1.3 Beam Profiles

A laser beam profile refers to the spatial intensity profile at the laser beam spot. The most common ones used in SLM are Single-mode Gaussian- and Multi-mode top-hat-shaped laser beams. In a case of Gaussian beam, the intensity is extremely high in the centre of the beam (Figure 7), with a tendency to result in increased evaporation of the material, and also cause spattering which disturbs the process stability (Okunkova *et al.*, 2016; Schleifenbaum *et al.*, 2011; Matilainen *et al.*, 2014). Because of the Gaussian profile, the line spacing should be more frequent since the beam diameter is small. The top-hat-shaped beam diameter is usually larger than with the Gaussian beam profile and the intensity of the beam is more uniform throughout the whole beam diameter (Figure 8).

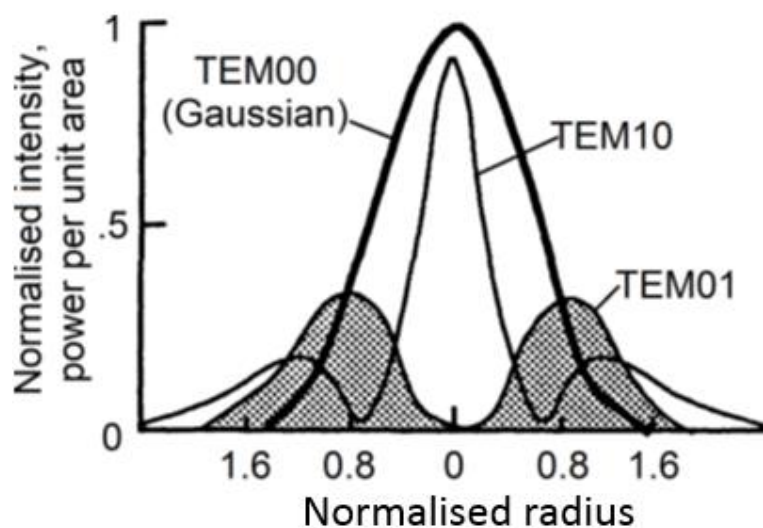


Figure 7: Intensity distribution of Gaussian beam (Schleifenbaum *et al.*, 2011).

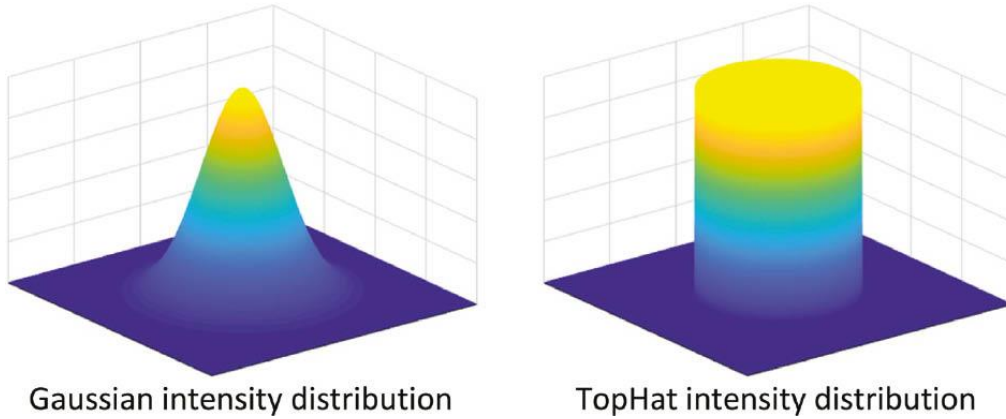


Figure 8: Intensity distribution of a Gaussian and TopHat intensity (Schleifenbaum *et al.*, 2011).

When considering Gaussian intensity distribution in any distance z along the propagation direction, the intensity distribution can be written as Equation 2 illustrates. For comparison, intensity distribution of ideally uniform laser beam (top-hat) is described in Equation 3 (Schleifenbaum *et al.*, 2011).

$$I_{(r,z)} = I_0 \cdot e^{-2r^2/w^2} \dots \dots \dots \text{Equation 2}$$

$$I_{(r,z)} \approx I_0 \dots \dots \dots \text{Equation 3}$$

where $I_{(r,z)}$ is rotationally symmetric Gaussian intensity distribution, r is the radial distance from the beam centre, I_0 is the maximum intensity of the beam, and w the beam radius.

2.1.4 Physical Phenomena in Selective Laser Melting

The principle operation of SLM is the laser beam scanning over the surface of a thin powder layer previously deposited on a substrate or previously re-melted layer. Line by line, a laser beam melts the material along a row of powder particles, thereby forming a dynamic molten pool. This process is rather complex and involves many different physical phenomena such as absorption and scattering of the radiation by the powder bed; radiation; convection and conduction heat transfers; phase transformation; fluid flows within the molten pool caused by the surface tension and density gradients; melting and re-solidification of a melt pool; wetting of the powder particles and substrate with the liquid; capillary effects; gravity, *etc.* (Figure 9). These complex phenomena are strongly material-dependent and are governed by a material's

chemistry and its optical, thermal and rheological properties (Das, 2003). A description of the most influential phenomena taking place during single track formation is given below.

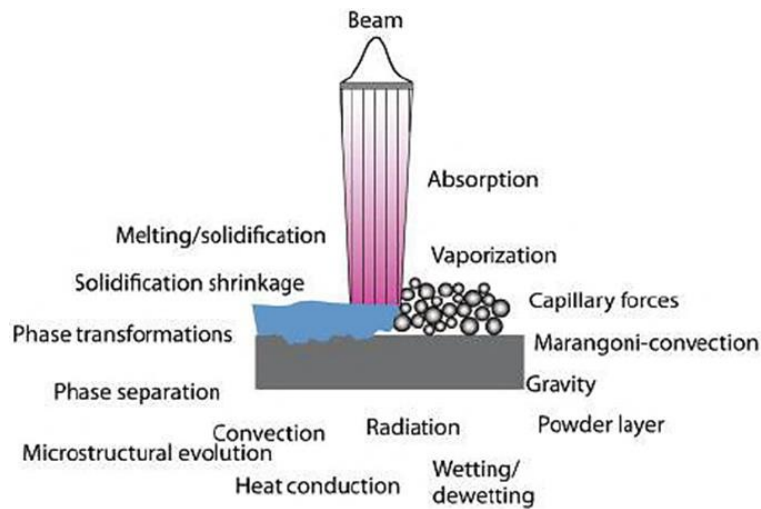


Figure 9: Physical phenomena occurring during SLM (Das, 2003).

2.1.4.1 Full Melting

Unlike laser sintering processes, SLM involves complete full phase transformation of the solid powder grains into liquid phase prior to cooling/solidification (Jerrard, 2011). The entire region of material exposed to the incident laser beam has to be melted to a depth exceeding the layer thickness. Thermal energy of subsequent scans of a laser is typically sufficient to re-melt a portion of the previously solidified solid structure; and thus, this type of full melting is very effective at creating well-bonded, high-density structures (Yadroitsau, 2009; Gibson *et al.*, 2014).

2.1.4.2 Vaporisation

When the laser beam interacts with the powder material, the temperature of the powder grains rises quickly above the melting point. The control of the maximum temperature reached is sometimes difficult and not precisely recognizable. If the temperature increases well above the melting point, the material can evaporate (Khairallah *et al.*, 2016).

2.1.4.3 Marangoni Convection

Marangoni convection, also known as Maragoni effect, describes the fluid flow behaviour in molten material caused by temperature gradients. This flow behaviour is important because it affects the geometrical characteristics of the melt pool. There are two key considerations in Marangoni convection: the surface tension temperature coefficient and the Prandtl number (*i.e.* a ratio of kinematic viscosity, ν , to thermal diffusivity, α). Figure 10 shows a schematic representation of Marangoni convection according to the sign of surface tension temperature coefficient.

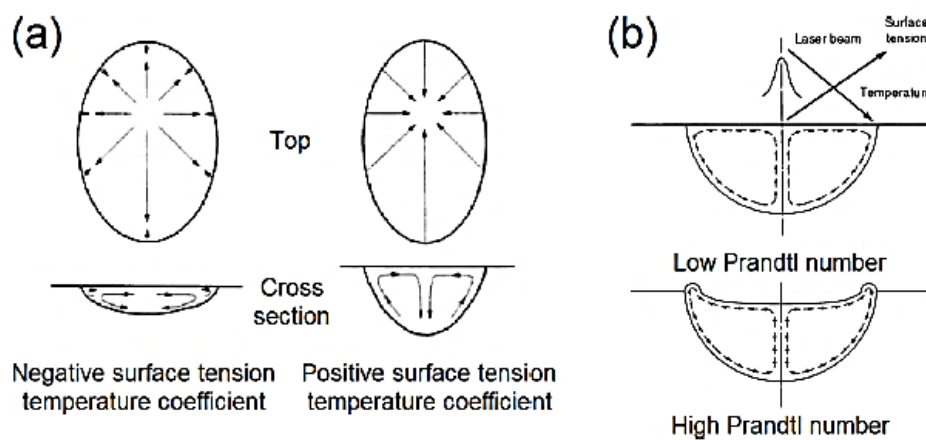


Figure 10: Schematic representation of Marangoni convection during laser melting: (a) flow orientation according to surface tension temperature coefficient; (b) effect of Prandtl number on a negative surface tension temperature coefficient (Mazumder, 1993)

Pure metals and most alloys have a negative surface tension temperature coefficient, which through addition of certain elements can be positive. A positive value results in the liquid being drawn to the centre of the top surface and then sinking (Mazumder, 1993). Increasing temperature increases surface tension, resulting in a narrower deep melt pool which can aid deeper penetration of a weld, therefore ensuring a deeper bond in the case of SLM. On the other hand, the Prandtl number denotes the form of heat flow. Calculation of the Prandtl number is shown in Equation 4.

$$Pr = \frac{\nu}{\alpha} = \frac{C\mu}{k} \dots \dots \dots \text{Equation 4}$$

where μ is the dynamic viscosity, k is the thermal conductivity, and C the specific heat capacity .

2.1.4.4 Plateau-Rayleigh Instability

Plateau-Rayleigh instability describes the behaviour of a liquid cylinder and the conditions under which this cylinder breaks into droplets. This phenomenon occurs primarily as a result of surface tension (Jerrard, 2011). Typically, a liquid cylinder will break into small droplets when a sinusoidal component has a wavelength greater than the cylinder's circumference (Chandrasekhar, 1981; Yadroitsev *et al.*, 2013). A schematic representation of Plateau-Rayleigh instabilities is illustrated in Figure 11.

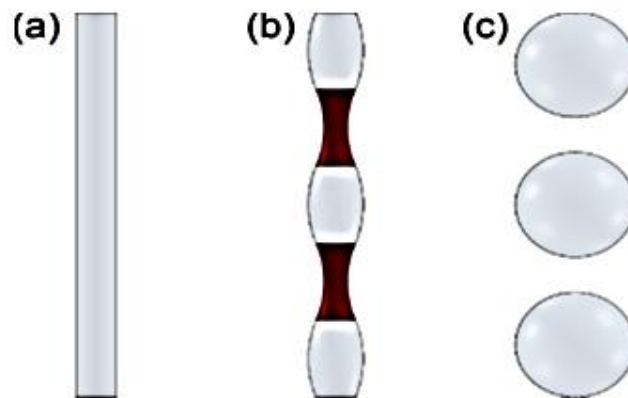


Figure 11: Schematic representation of Rayleigh instabilities: (a) a liquid cylinder in an unperturbed state; (b) inherent instabilities deform the surface of the cylinder, leading to regions of high- and low pressure (highlighted pinched regions have a higher pressure); (c) the cylinder breaks into droplets upon rupture of the pinched regions (Jerrard, 2011).

Rayleigh instabilities are common in SLM due to the formation of a dynamic molten pool using a laser (Figure 12). In SLM, temperature gradients are comparatively high and result in Marangoni effects. Plateau-Rayleigh instabilities within SLM are further influenced by the internal and surface motion of the liquid. According to Yadroitsev *et al.* (2010), a larger area of interface between the liquid and substrate results in a more stable weld bead. Therefore, a weld bead must have satisfactory penetration of the material below in order to counter Plateau-Rayleigh instabilities.

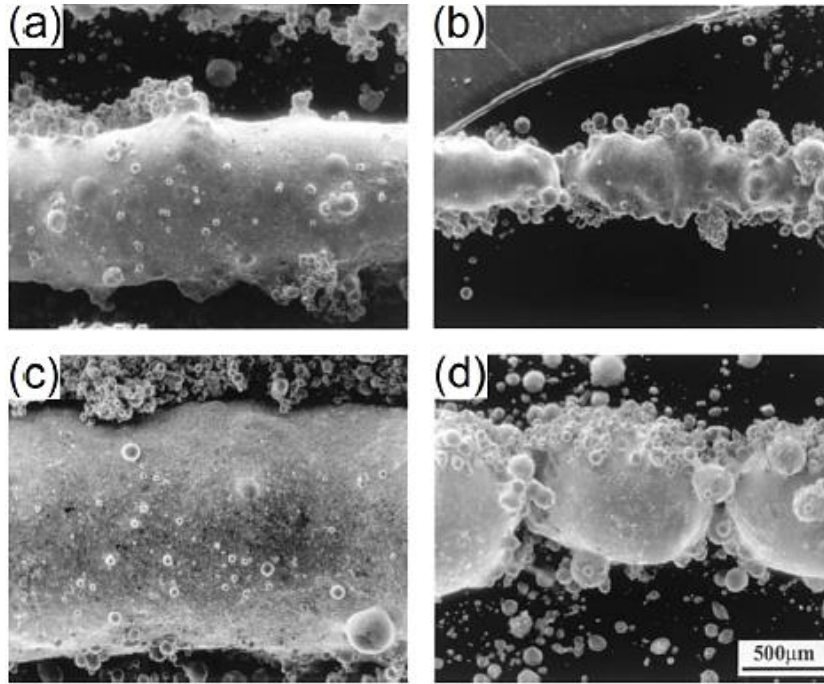


Figure 12: Example of Plateau-Rayleigh instabilities affecting a single line laser scan of M2-117 HSS steel powder (a) 50 W, 5 mm s⁻¹; (b) 50 W, 20 mm s⁻¹; (c) 150 W, 5 mm s⁻¹; (d) 150 W, 20 mm s⁻¹ (Niu and Chang, 1999).

2.1.4.5 Wetting

Wetting refers to the ability of a liquid to maintain contact with a solid surface as a result of intermolecular interactions when the two are brought together (Facchini, 2010). Since SLM involves full melting of material in consecutive layers that must bond to allow successful consolidation, wetting is perhaps the most influential phenomenon and is studied extensively in SLM. Figure 13 shows optical micrographs of single tracks produced at different scanning speeds. With the increase of scanning speed, the melt pool leads to unfavourable wetting, flowing, spreading characteristics, and corresponding balling phenomenon (Shi *et al.*, 2016). The degree of wetting is determined by the contact angle of the liquid and the surface with which it makes contact (Das, 2003; Jerrard, 2011). In a typical wetting situation, the equilibrium of a liquid in contact with a non-interacting solid and gaseous phase is shown in Figure 14, governed by the Young's equation (Equation 5). The liquid will wet the substrate as $\cos(\theta)$ approaches 1, or equivalently, if $\gamma_{sv} - \gamma_{sl} > \gamma_{lv} \cos(\theta)$. This corresponds to the case on the left (Das, 2003).

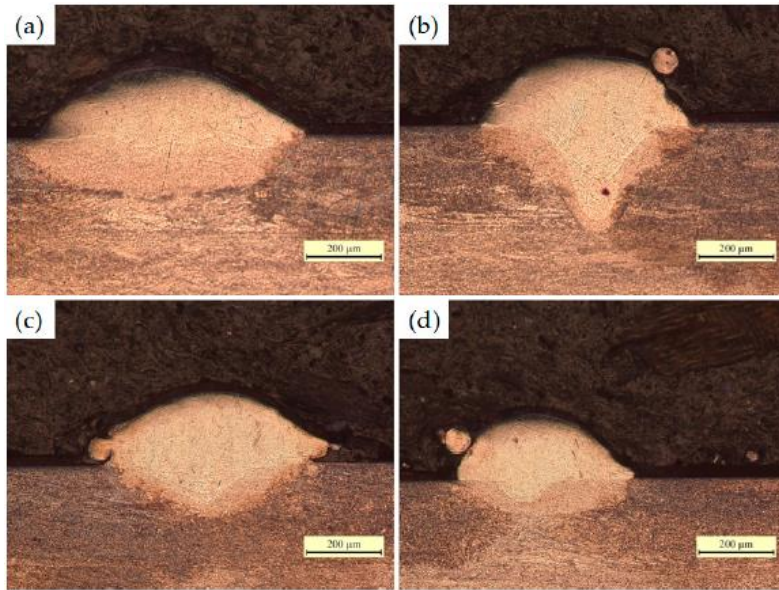


Figure 13: Optical micrographs of Ti6Al4V single scan tracks ($P = 400 \text{ W}$): (a) 80 mm/s, (b) 120 mm/s, (c) 160 mm/s, (d) 200 mm/s (Shi *et al.*, 2016).

In direct laser melting of metals, oxidation at elevated temperatures can adversely affect wetting, leading to poor interlayer connection (Das, 2003; Jerrad, 2011; and Hebert, 2016). Hence, the use of an inert gas or vacuum to enforce a low-oxygen-content atmosphere is standard practice in SLM-type processes, as well as supplying sufficient laser energy to re-melt part of the previous layer in order to break up any potential oxide layer formation.

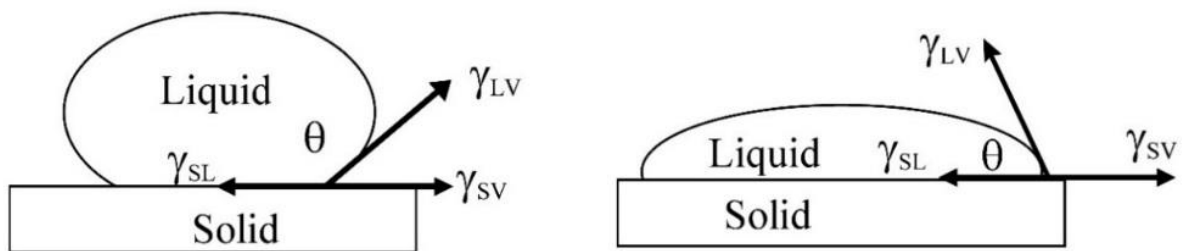


Figure 14: Schematic of isothermal surface wetting: the left side represents low wettability, whereas the right side represents high wettability (Hebert, 2016).

$$\gamma_{sv} = \gamma_{sl} + \gamma_{lv} \cos(\theta) \dots \dots \dots \text{Equation 5}$$

where γ_{sv} is the solid-gas surface energy, γ_{sl} the solid-liquid surface energy, γ_{lv} the liquid-gas surface energy, and θ is the equilibrium wetting angle.

Wetting in SLM is usually homologous (*i.e.* wetting of a solid substrate by molten liquid of the same material). As such, θ_s , the angle of solid formation compared to the base plate is calculated as the arcsine of the Stefan number, S , as per Equation 6.

$$S = \frac{C(T_f - T_t)}{L} \dots\dots\dots \text{Equation 6}$$

where C is the material's specific heat capacity, T_f is the temperature of fusion, T_t is the target temperature and L is the latent heat of fusion.

2.1.4.6 Balling

Balling is associated with Plateau-Rayleigh instabilities as a result of liquid material attempting to find optimum geometry upon break-up of a liquid cylinder, and poor wetting of the solid substrate beneath (Das, 2003). In other words, the material is attempting to reach an optimum value between surface area and volume due to surface tension and wetting. Therefore, balling can be considered as the culmination of phenomena occurring in SLM (Figure 15).

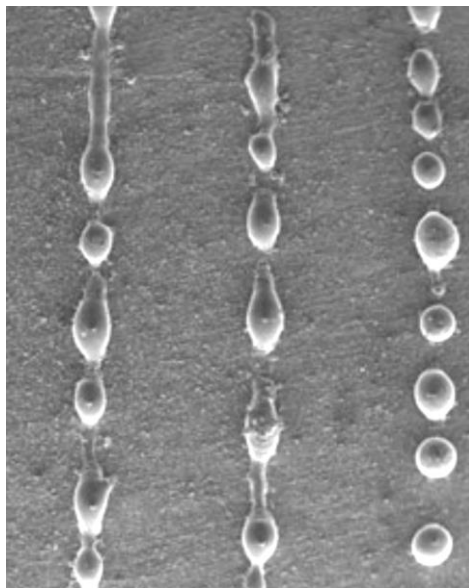


Figure 15: Typical balling in SLM (Li *et al.*, 2012).

2.1.4.7 Epitaxial Solidification and Anisotropy of Properties

One of the implications of re-melting concerns the occurrence of grain growth during solidification of a new layer at the interface between solid and molten metal. Solidification is epitaxial, through a mechanism of heterogeneous nucleation (Kou, 1987). Figure 16 shows the nucleation of a crystal from a liquid on a flat substrate with which the liquid is in contact. The

parameters γ_{LC} , γ_{LS} , and γ_{CS} are the surface energies of the liquid–crystal interface, liquid–substrate interface, and crystal–substrate interface, respectively. The energy barrier ΔG for the crystal to nucleate on the substrate is:

$$\Delta G = [4\pi\gamma_{LC}^3 T_m^2 / 3(L\Delta T)^2] \cdot (2 - 3\cos\theta + \cos^3\theta) \dots\dots\dots \text{Equation 7}$$

where T_m is the equilibrium melting temperature, L the latent heat of melting, ΔT the undercooling below T_m , and θ the contact angle (Kou, 1987; and Das, 2003). If the liquid wets the substrate completely, the contact angle θ is zero and so is ΔG . This means that the crystal can nucleate on the substrate without having to overcome any energy barrier required for nucleation. The energy barrier can be significant if no substrate is available or if the liquid does not wet the substrate completely.

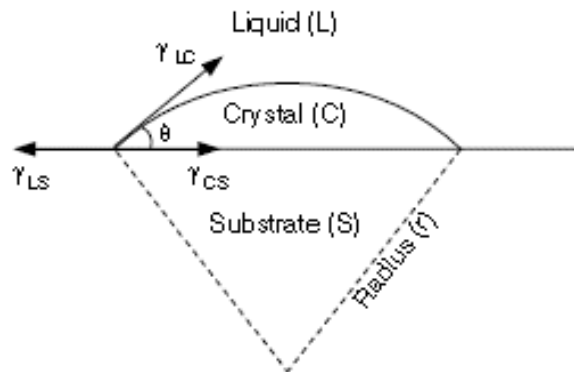


Figure 16: Spherical cap of a crystal nucleated on a planar substrate from a liquid (Kou, 1987).

In SLM, the existing base-metal grains at the fusion line act as the substrate for nucleation (Das, 2003). Since the liquid metal of the melt pool is in close contact with these substrate grains and wets them completely ($\theta = 0$), crystals nucleate from the liquid metal upon the substrate grains without difficulties. Nucleation occurs by arranging atoms from the liquid metal upon the substrate grains without altering their existing crystallographic orientations (Kou, 1987). Such a growth initiation process, shown schematically in Figure 17, is called epitaxial growth or epitaxial nucleation. Anisotropy in the microstructure causes different properties in different directions, *i.e.* anisotropy of mechanical properties.

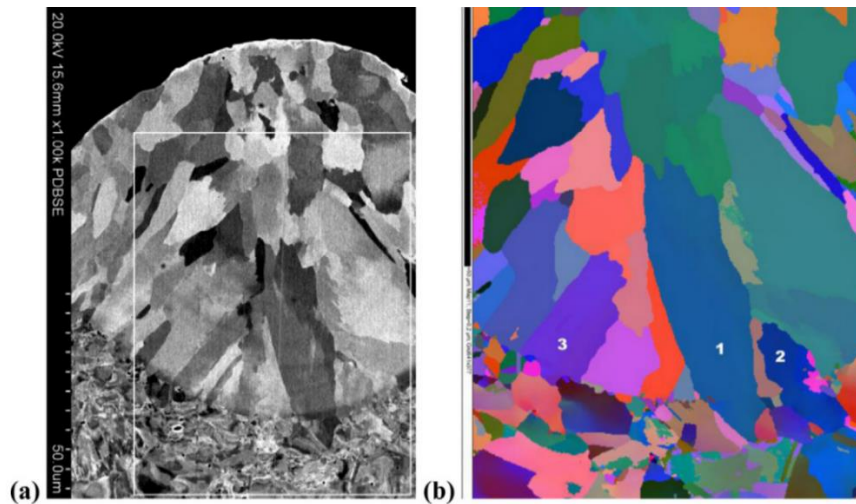


Figure 17: ECCI image of cross-section of the SLM SS 316L track fabricated at 0.12 m/s, preheating temperature 80 °C (a), EBSD orientation map of the marked region of the track, 1-2-3 grains illustrate epitaxial growth of colonies from the substrate (b) (Yadroitsev *et al.*, 2013).

2.1.4.8 Residual Stresses

Another implication of thermocycling, linked with rapid heating and cooling, is the process susceptibility to residual stresses which can cause distortions, cracks, and delamination in SLM parts. Figure 18 shows a titanium part ripped from the build plate during SLM due to residual stress build-up.

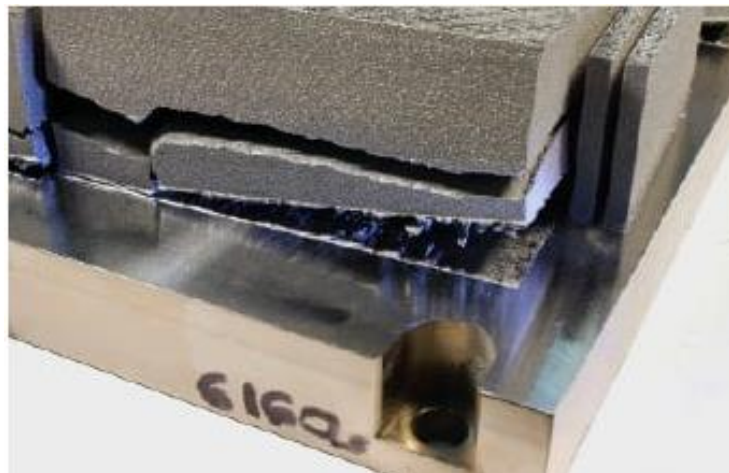


Figure 18: Titanium part ripped from the build plate during SLM (<https://www.engineering.com/3DPrinting/3DPrintingArticles/ArticleID/15202/7-Issues-to-Look-Out-for-in-Metal-3D-Printing.aspx>)

In SLM, there are two main mechanisms by which residual stresses may develop: (i) stresses in the solid substrate just underneath the present layer being melted and (ii) stresses due to the

cooling down of the molten top layers (Merzelis and Kruth, 2006; Kempen *et al.*, 2013). The first phenomenon is commonly referred to as the Temperature Gradient Mechanism (TGM), and arises from the large thermal gradient between the upper layers being heated by the laser and the lower layers in the part (Figure 19). Due to the high temperature in the upper layers, those heated layers expand quicker than the cooler lower layers. This induces compressive stresses (σ_{comp}) in the upper layers that may rise above the yield strength of the material and cause plastic deformation (ϵ_{pl}) of the upper layers. When those plastically deformed layers cool down, their compressive state is converted into residual tensile stresses (σ_{tens}). Those residual stresses may induce cracking of the part. In the second phenomenon, the molten top layer tends to shrink during cooling, but the shrinkage is inhibited by the underlying bulk layers, thus introducing tensile stresses in the top layers, and compressive stresses below.

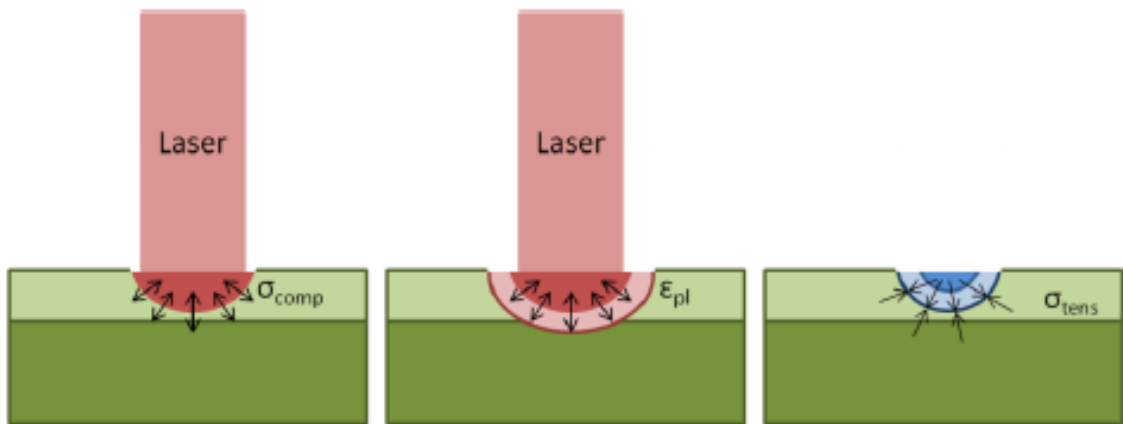


Figure 19: Simple schematic of the cause of residual stresses within SLM (Kempen, 2013)

Heat treatment is a traditional method to reduce stresses in metallic parts, which are normally used in welding, casting, forging, *etc.* However, post-heating cannot prevent warping and cracking caused by thermal stress during the SLM process. These can be prevented by weakening local temperature gradients by: (i) optimising and controlling the process (e.g. laser power and beam transverse speed), (ii) re-scanning of each layer, (iii) pre-heating the base plate and the previously solidified layers, and (iv) selecting proper building- and scanning strategies. So far it has been shown that the best way to reduce thermal stress is by uniform pre-heating of the baseplate (Das, 2003; Merzelis and Kruth, 2006; Kempen *et al.*, 2013; Shamsaei *et al.*, 2015; and Liu *et al.*, 2016). Figure 20 (Kempen *et al.*, 2014) shows SLM samples that were produced at different pre-heating temperatures.

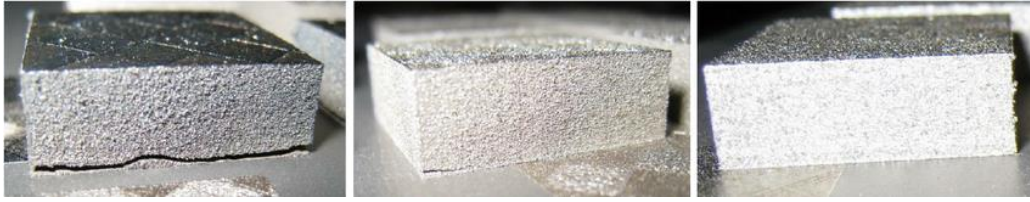


Figure 20: M2 HSS parts produced with a pre-heating temperature of 90 °C (left), 150 °C (middle), 200 °C (right)

2.2 PRECIPITATION HARDENING 17-4 SS

2.2.1 Background

Precipitation hardening stainless steels (SS) evolved from martensitic stainless steels with the aim of improving the mechanical properties of martensitic stainless steels, especially the fracture toughness while also increasing the corrosion resistance. These grades of stainless steel obtain their strength from precipitation reactions. They contain alloying additions which can form fine nanometre-scale precipitates during heat treatment. When stresses are applied to these alloys, the precipitates act as obstacles to dislocation movement, subsequently increasing strength (Yoo *et al.*, 2006). The corrosion resistance is due to the addition of Chromium (Cr).

These stainless steels are classified according to their microstructure upon the initial annealing treatment: martensitic, semi-austenitic and austenitic. The 17-4 PH stainless steel has a martensitic structure, with copper being its strengthening agent for the precipitation hardening mechanism. The 17 and 4 denote the approximate weight percent of Cr and Ni, respectively. Due to the combination of high strength and good corrosion properties at high temperatures up to 300 °C, the 17-4 PH stainless steel is widely used in the aeronautical, aerospace, chemical and petrochemical industries and also in the marine and energy sectors. Table 4 reports the nominal chemical composition of 17-4 PH stainless steel.

Table 4: Chemical composition range of 17-4 PH stainless steel
(<https://www.upmet.com/products/stainless-steel/17-4-ph#Chemical-Properties>)

C	Si	Mn	P	S	Cr	Ni	Cu	Nb	Fe
≤ 0.07	≤ 1.00	≤ 1.00	≤ 0.040	≤ 0.02	15.0- 17.5	3.00- 5.00	3.00- 5.00	≤ 0.45	Balance

2.2.2 Effect of Alloying Elements

2.2.2.1 Carbon

Carbon (C) is generally responsible for hardening steels by forming carbides with iron or other alloying elements. However, the carbon content coupled with the high Chromium (Cr) may have a detrimental effect on the corrosion resistance of the material by forming chromium carbides (Cr_{23}C_6) along the grain boundaries and causing a decrease in toughness. In 17-4 PH, the carbon is intentionally kept to extremely low levels (<0.07% wt. max) to suppress the formation of Cr_{23}C_6 . Additionally, elements with greater carbide stability are introduced into the system (Barlow, 2010).

2.2.2.2 Silicon

Silicon (Si) is added to 17-4 PH to improve the fluidity of the molten metal during the casting operation but can have a negative effect by acting as a ferrite stabiliser. Increased amounts of ferrite will reduce the strength of the material. To counteract this effect, the quantities of Cr and Ni are balanced with the Si to act as austenite stabilizer and prevent the formation of ferrite (Okamoto, 1962).

2.2.2.3 Manganese

Manganese (Mn) is usually added to this alloy to assist in de-oxidation during melting, and also act as austenite stabiliser, while also forming MnS to prevent the formation of the more detrimental FeS phase which can cause hot cracking (Thompson *et al.*, 1991).

2.2.2.4 Phosphorus and Sulphur

Phosphorus (P) and Sulfur (S) are generally seen as impurities and concentrations of these elements are kept to a minimum. Phosphorus tends to segregate towards grain boundaries, where it lowers the surface energy and reduces grain cohesion. In addition, both trace elements have been suggested to promote dendritic segregation and possibly enhance phosphorus diffusion to grain boundary sites (Christein *et al.*, 2003; and Tavares *et al.*, 2017).

2.2.2.5 Chromium

Chromium (Cr) is responsible for the passive behaviour of all stainless steels. It forms an adherent and insoluble surface film that prevents diffusion of oxygen into the surface of the material to prevent rusting (oxidation) of the iron in the matrix.

2.2.2.6 Nickel

Nickel (Ni) is used as a toughening agent, as well as an austenite stabiliser. The addition of Ni increases the fracture toughness and decreases the ductile to brittle transition temperature (Cunat, 2004).

2.2.2.7 Copper

Copper (Cu) is the precipitation hardening agent. The low weight percent ensures that it is fully soluble within austenite. When the material is austenitised and quenched, it results in a supersaturated martensite matrix, which when aged will result in the formation of fine copper precipitates.

2.2.2.8 Niobium/Tantalum

The metallurgical effects of Niobium (Nb) and Tantalum (Ta) are essentially identical in behaviour, and sometimes one is substituted for the other on a supply and cost basis. Both are added to suppress the formation of Cr_{23}C_6 in 17-4 PH. Nb and Ta have higher carbide stability than Cr at higher temperatures, hence they tend to form preferentially as compared to chromium carbides. This promotes retention of corrosion resistance and decreasing hardness losses at higher aging temperatures. These desirable MC carbides also provide tempering resistance during aging (Cunat, 2004; de Oliveira *et al.*, 2017).

2.2.3 Solidification and Microstructure of 17-4PH Stainless Steel

The solidification of 17-4 PH stainless steel can be traced with the Fe-Cr-C equilibrium phase diagram shown in Figure 21. The alloy starts to solidify as body centred cubic (BCC) δ -ferrite, followed by the transformation to face centred cubic (FCC) austenite, and ends with the formation of BCC α -ferrite and M_{23}C_6 carbides. However, Figure 21 is an equilibrium diagram and does not predict the formation of body centred tetragonal (BCT) martensite. The final microstructure of cast or wrought 17-4 PH stainless steel usually consists of a martensitic

matrix with small amounts of δ -ferrite in the form of stringers and small amounts of retained austenite (Figure 22). Cooling rates between the critical martensite start temperature (M_s) and martensite finish temperature (M_f) influence the ratios of retained austenite and martensite in the quenched product (Abrahams, 2010; Facchini, 2010; Cheruvathur *et al.*, 2016).

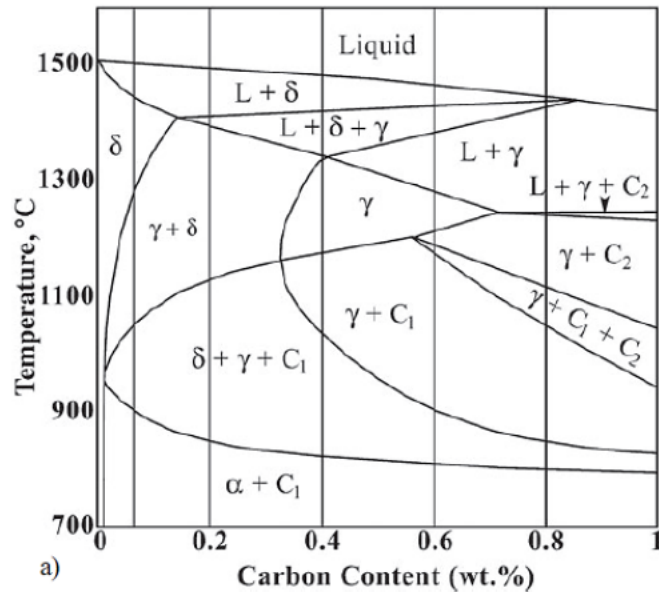


Figure 21: Ternary Fe-Cr-C phase diagram at 17% Cr that has phase changes similar to 17-4PH stainless steel. C_1 and C_2 are $M_{23}C_6$ and M_7C_3 carbides (Wanjara and Jahazi, 2008).



Figure 22: Optical micrograph of ferrite stringers in a martensite matrix of 17-4 PH stainless steel (Facchini, 2010).

2.2.3.1 δ -Ferrite

δ -Ferrite is known to decrease the ductility and impact strength, which increases the susceptibility of crack during thermo-mechanical treatments. It is, therefore, important to eliminate as much of the δ -ferrite in the finished component as possible, through a homogenization heat treatment (Vasudevan *et al.*, 2003; Wanjara and Jahazi, 2008; and Abrahams, 2010).

2.2.3.2 Retained austenite

Retained austenite refers to austenite that remains untransformed upon solidification, typically found along martensite lath boundaries. The amount found in the final microstructure depends on the martensite finish (M_f) temperature and the rate at which it is cooled to that temperature. If the M_f temperature is below the temperature that the material is cooled to, there will be a certain amount of retained austenite because the martensite transformation will not be completed. Also, when 17-4 PH stainless steel is cast or welded, microsegregation can lead to regions of the material that are enriched in austenite stabilising elements which can contribute to the retention of austenite. Retained austenite typically decreases the yield and tensile strength of the material while increasing the impact toughness (Nakagawa and Miyazaki, 1999; Wang *et al.*, 2006). Its formation can be suppressed by using a solution treatment with a cooling rate as slow as normalising.

2.2.3.3 Martensite

Martensite is the dominant phase present in the matrix of 17-4 PH stainless steel. When austenite is quenched, it transforms to martensite through a shear mechanism, shown in Figure 23. When FCC austenite shears to a BCC structure, carbon and nitrogen atoms get trapped in the octahedral sites resulting in the elongation of a BCC structure to form a BCT crystal structure. The microstructure of martensite comprises of packets, blocks and laths (Figure 24). Prior austenite grains form packets which contain blocks that comprise of laths. The laths are separated by low-angle boundaries and blocks are separated by high-angle boundaries. During heat treatment, the block boundaries migrate and the grains recrystallise to relieve stresses and improve toughness (Nishiyama, 1978; and Abrahams, 2010).

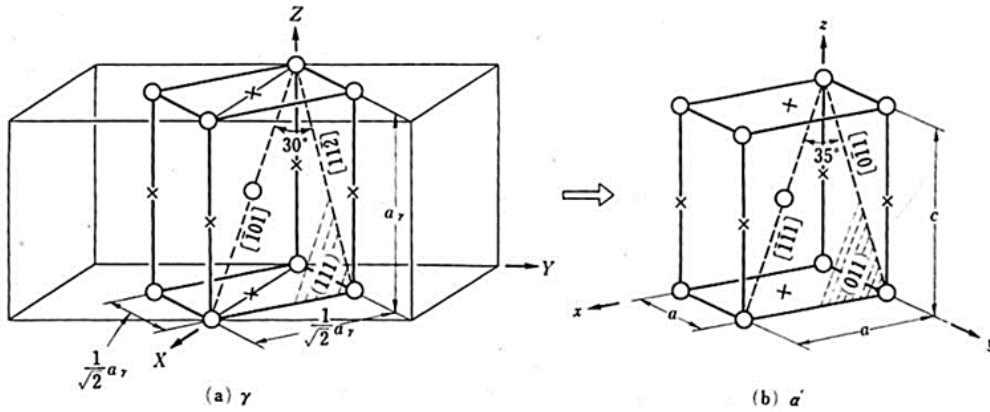


Figure 23: Illustration of the transformation from austenite to martensite. “o” indicates the positions of the Fe atoms, “x” indicates the positions available for C atoms (Nishiyama, 1978).

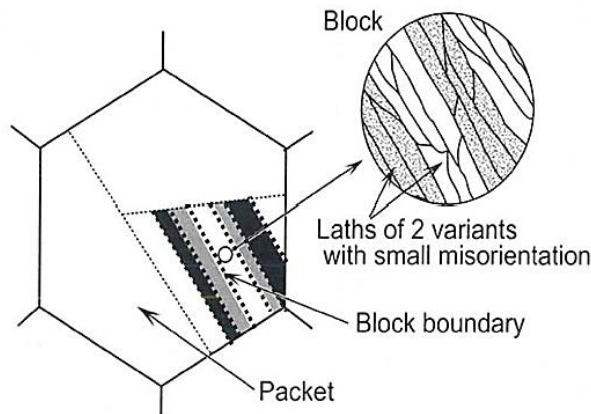
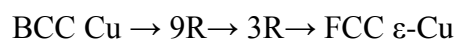


Figure 24: Illustration describing martensite laths, blocks and packets (Abrahams, 2010).

2.2.3.4 Precipitates

The initial martensitic microstructure of 17-4PH stainless steel formed after solidification is supersaturated with copper, which precipitates out of solution during aging treatment at high enough temperatures for long enough periods of time. These precipitates are normally in the nanoscale and as a result they cannot be viewed under light optical microscope. A Transmission Electron Microscope (TEM) is normally used to reveal the precipitates. The precipitation of Cu takes place through a sequential process shown as follows:



Copper clusters, which form due to segregation during solidification, will initially precipitate as coherent nanometre-sized BCC-Cu particles. As the particles increase in size, they form a twinned 9R structure. Further increase in size leads to the untwinned ellipsoid 3R structure,

and finally, when the particles exceed 30 nm, they take the form of FCC-Cu (Antony, 1963; Marandel *et al.*, 1975; Hsiao *et al.*, 2002; and Guo *et al.*, 2003).

Cr_{23}C_6 and niobium carbide (NbC) precipitates can also form during the aging of this alloy and will increase the overall strength of the material as well. However, excessive formation of Cr_{23}C_6 and formation of Cr_{23}C_6 along grain boundaries can lead to embrittlement. Varying the heat treatment can change the amount of each of these constituents and therefore the mechanical properties of the alloy (Guo *et al.*, 2003).

2.2.4 Heat Treatments and Mechanical Properties of 17-4 PH Stainless Steel

Figure 25 depicts the typical heat treatment cycle for precipitation of hardening alloys. The three steps shown are homogenisation, solution annealing and secondary aging. The homogenisation step is performed at a temperature well above AC_3 to remove the segregation that occurs during solidification and slow cooling to room temperature. Solution annealing is performed at a temperature above AC_3 to transform the microstructure completely to austenite, which will be rapidly cooled, typically in water, to produce a fully martensitic microstructure. Finally, the alloy is aged at a temperature below AC_3 to allow the formation of precipitates and also to temper the martensitic matrix (Abrahams, 2010).

The specific aging time and temperature will determine the size and coherency of the precipitates formed, which will determine the overall strength of the material. The 17-4 PH stainless steel, whether wrought or cast, is usually aged at temperatures between 482–621 °C for various periods of times (Hsiao *et al.*, 2002; Guo *et al.*, 2003; and Abrahams, 2010). The minimum properties expected in cast and wrought materials differ greatly; in the near peak-aged condition, wrought 17-4 PH minimums are higher than that of cast 17-4 PH stainless steel. The standard heat treatment codes and the corresponding mechanical properties of 17-4 PH stainless steel are listed in Table 5 and Table 6 respectively.

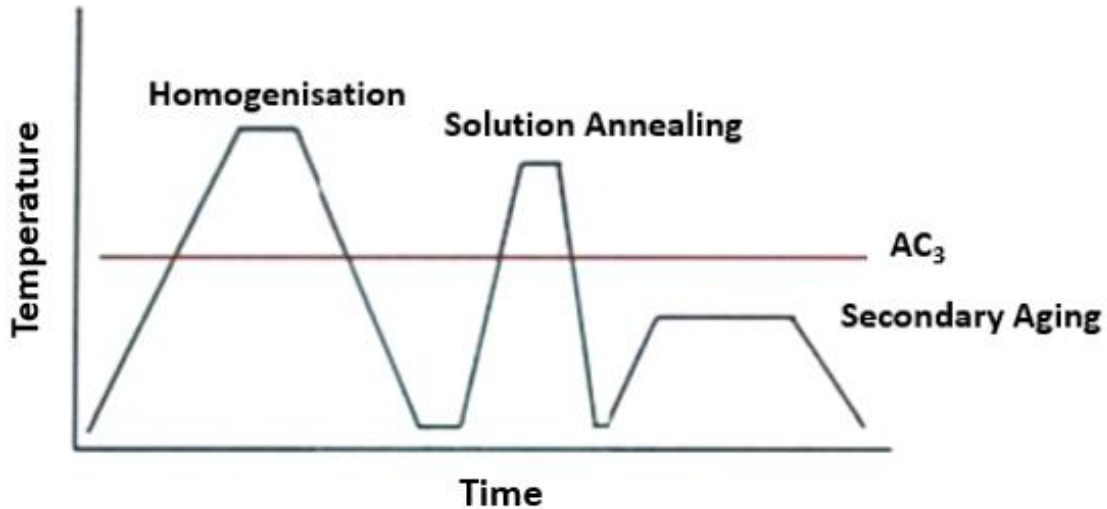


Figure 25: Typical precipitation heat treatment diagram for precipitation hardening alloys (Abrahams, 2010). AC_3 is the temperature at which transformation of ferrite to austenite is completed during heating.

Table 5: Standard heat treatment procedures for 17-4 PH stainless steel (ASTM A747, 2004; ASTM A564/A564M, 2004)

Condition	Solution heat treatment °C	Aging treatment °C	Time at temperature, hours	Type of cooling
A	1038	-	15-30 min	Air
H900	1038	482	1	Air
H925	1038	496	4	Air
H1025	1038	551	4	Air
H1075	1038	580	4	Air
H1150	1038	621	4	Air

Table 6: Minimum properties of 17-4 PH stainless steel, both cast and wrought (ASTM A747, 2004; ASTM A564/A564M, 2004)

Condition	σ_y/σ_t min Cast (MPa)	σ_y/σ_t (MPa), minimum, wrought	Elongation (%), cast/wrought
A	Not hardened		
H900	1000/1172	1172/1310	5/10
H925	1034/1207	1069/1172	5/10
H1025	965/1034	1000/1069	9/12
H1075	793/1000	862/1000	9/13
H1150	655/862	724/931	10/16

2.2.5 Physical Properties of 17-4 PH Stainless Steel

A physical property is defined as a characteristic of matter that may be observed and measured without changing the chemical identity of the substance. There are two classes of physical properties; intensive- and extensive properties. An intensive property does not depend on the amount of matter in a sample, rather it is a characteristic of the material. Examples of this include melting point and density. Extensive properties do depend on sample, and examples include shape, volume and mass. In this study, we focus on the intensive properties shown in Table 7.

Table 7: Available experimental physical properties of 17-4 PH stainless steel (Rack, 1981; Sabau and Porter, 2008; and Koo, 2013).

Name	Symbol	Value
Liquidus temperature	T_l	1440 °C
Solidus temperature	T_s	1404 °C
Boiling point	T_v	≥ 2860 °C
Density	ρ_s	~ 7750 kg/m ³
Thermal conductivity (100 °C)	k_s	18.3 Wm ⁻¹ K ⁻¹
Specific heat (20 °C)	C_p	460 J/(kg K)
Dynamic viscosity	μ_s	0.03354 g/cm/s
Mean Coefficient of Thermal expansion (21–427 °C)	α_L	11.3×10^{-6}
Modulus of Elasticity	E	196 GPa
Thermal diffusivity (20 °C)	a	5.13×10^{-6} m ² /s

2.2.5.1 Density

Most alloys usually have different densities varying with temperatures, thus density in SLM is one of the important material properties due to the effect of thermal expansion during the heating and cooling cycles. The density of solid 17-4PH stainless steel is 7750 kg/m³ at room temperature. However, the density decreases gradually with increasing temperature. Figure 26 shows how the temperature affects the density of 17-4 PH stainless steel.

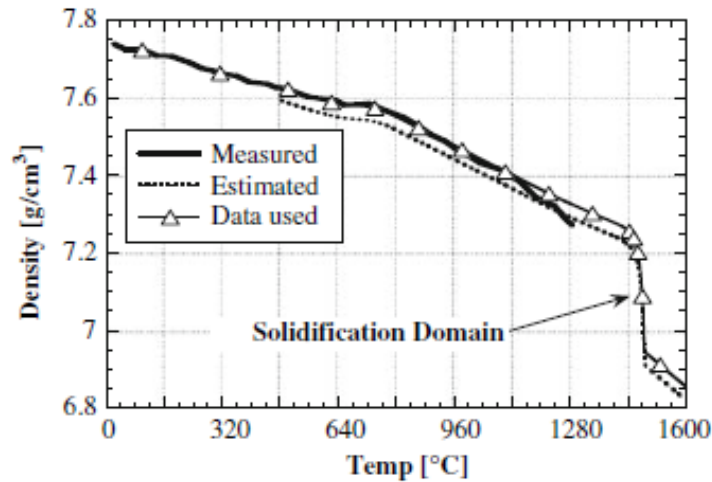


Figure 26: Density variation of 17-4 PH stainless steel with temperature (Sabau and Porter, 2008).

2.2.5.2 Specific heat

Metals and alloys are temperature-sensitive materials. Therefore, a physical quantity called heat capacity is useful to measure the effect of thermal energy accumulation. In general, heat capacity denotes an ability to absorb heat energy for a one-degree change in temperature. The physical quantity is often divided by mass; heat capacity per unit mass is expressed as specific heat capacity. This property is also temperature dependent (Figure 27).

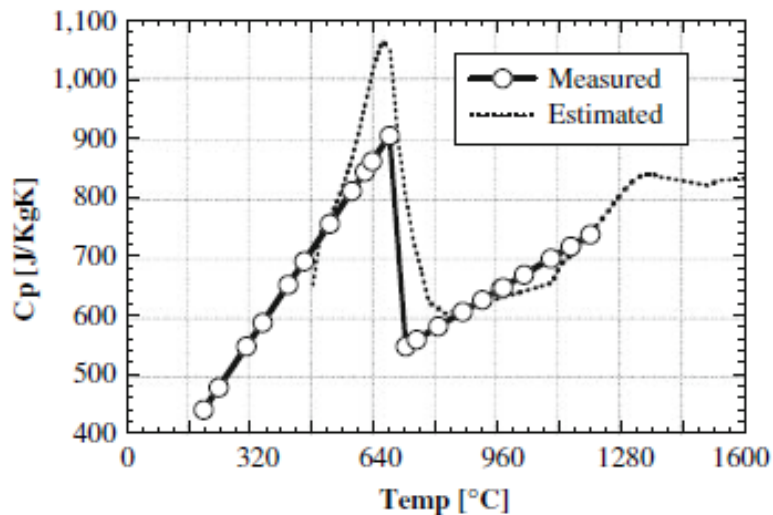


Figure 27: Specific heat of 17-4PH stainless steel as a function of temperature (Sabau and Porter, 2008).

2.2.5.3 Thermal conductivity

Thermal conductivity is the ability of a material to conduct thermal energy from one material to another. Therefore, thermal conductivity is relevant to the rate of heat conduction through a material in SLM. Heat conduction rate usually varies with increasing temperature thus, thermal conductivity is a highly temperature-dependent property. Figure 28 shows the change in thermal conductivity of 17-4 PH stainless steel with increasing temperature.

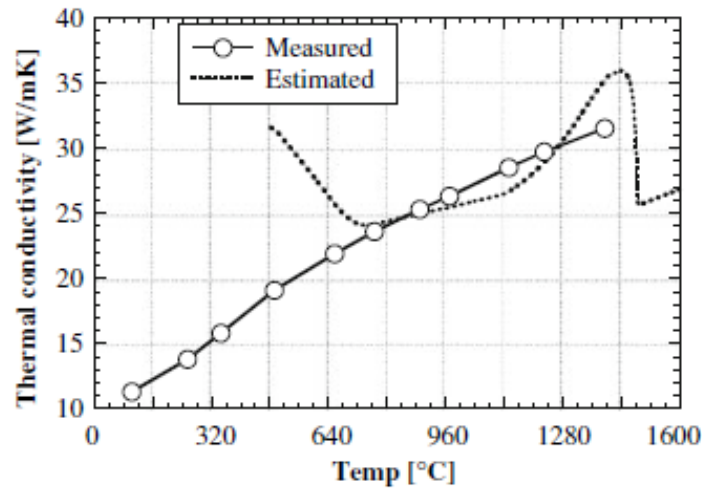


Figure 28: Thermal conductivity of 17-4PH stainless steel as a function of temperature (Sabau and Porter, 2008).

2.3 SELECTIVE LASER MELTING OF 17-4PH STAINLESS STEEL

2.3.1 Single tracks

In SLM, the initial units formed are single tracks which overlap to create a single layer and from the sequence of layers a 3D object is manufactured. The feature of track instability depends on the laser power, scanning speed, powder layer thickness, substrate material, physical properties and granulomorphometry of the powder used (Yadroitsev and Smurov, 2010; Smurov *et al.*, 2014; Antony and Arivazhagan, 2015; Yadroitsava *et al.*, 2015; and Kusama *et al.*, 2017). Thus, the properties of parts manufactured by SLM strongly depend on the properties of each single track and each single layer. Therefore, understanding the mechanisms of formation of single laser-melted tracks and instabilities of the molten pool is imperative. However, currently there are few studies published on single tracks of 17-4 PH steel. Most are rather focused on investigating the microstructure and mechanical properties of 17-4 PH.

Averyanova *et al.* (2012) investigated the effect of main process parameters (*i.e.*, laser spot size of 70 μm , laser power $P=35\text{--}50$ W, scanning speed $v=50\text{--}150$ mm/s, layer thickness of 20-50 μm , and hatch spacing 100-160 μm) on the build characteristics of 17-4PH stainless steel single tracks and single layers using a design of experiments approach. With regard to single line analyses, the layer thickness was found to have a significant impact on the height of the single track, while the height of the dilution zone (remolten depth) was affected by the laser power. The width of the tracks showed dependence on the laser power, scanning speed and interaction between these parameters, while the effect of layer thickness on the width was found to be nonsignificant. It should be noted that the powder layer chosen was thin and the apparent density of the powder material was very low. Secondly, the width of the molten pool was mainly determined by laser spot size (Yadroitsau, 2009).

Matilainen *et al.* (2015) investigated keyhole phenomena during single track formation of 17-4PH stainless steel at $P= 200\text{--}325$ W laser power with spot size of 100 μm and layer thickness of 20 μm using a high-speed active illumination imaging system. It was found that as the energy density (defined as the ratio of laser power to product of layer thickness), scanning speed, hatch distance and interaction time increase, the penetration depth also increases, while the width-to-depth ratio decreases. The dependence of geometrical characteristics was found to be a function of linear energy density. The same conclusion was reached by Gong *et al.* (2014) in the case of Ti-6Al-4V. When laser power energy is very high, the laser interaction time was found to have an effect on keyhole formation, since the penetration depth increases as the laser interaction time increases (Matilainen *et al.*, 2015; Yadroitsava *et al.*, 2015).

Therefore, behaviour of individual tracks and their geometric characteristics depend on the process parameters, physical, chemical and granulomorphometrical properties of the powder.

2.3.2 Microstructure

Mechanical properties of SLM parts depend primarily on their microstructure (e.g. grain size and morphology), which in turn is influenced by the thermal history during manufacturing *i.e.*, cooling rates, thermal gradients, and reheating cycles. Factors such as high localised heat inputs, very short interaction times, and local heat transfer conditions influence the microstructure. Also, the rapid cooling rates associated with SLM result in a non-equilibrium solidification process and enhance the limitation of solid solubility, refinement of grains, and

possible formation of a new metastable phase. However, large temperature gradients and complex heat transfer formed in a molten pool can cause preferential grain growth and heterogeneous structure (Song *et al.*, 2015; and Hebert, 2016).

Overlaps between molten pool boundaries can be clearly observed in 17-4PH stainless steel manufactured by SLM (Figure 29). The cross-sectional molten pool of a single track presented an arc-shaped configuration, which can be attributed to Gaussian energy distribution of the laser beam (Song *et al.*, 2015). Multi-line and multi-layer single tracks accumulated to form a 3D object that is totally different from the traditional processing. In addition, fine cellular and dendritic structures with a grain size less than 1 μm was observed within each laser track, as shown in Figure 29b. The microstructure can be controlled by adjusting the main parameters, such as laser power, scanning speed, scanning strategy, processing atmosphere, amongst others.

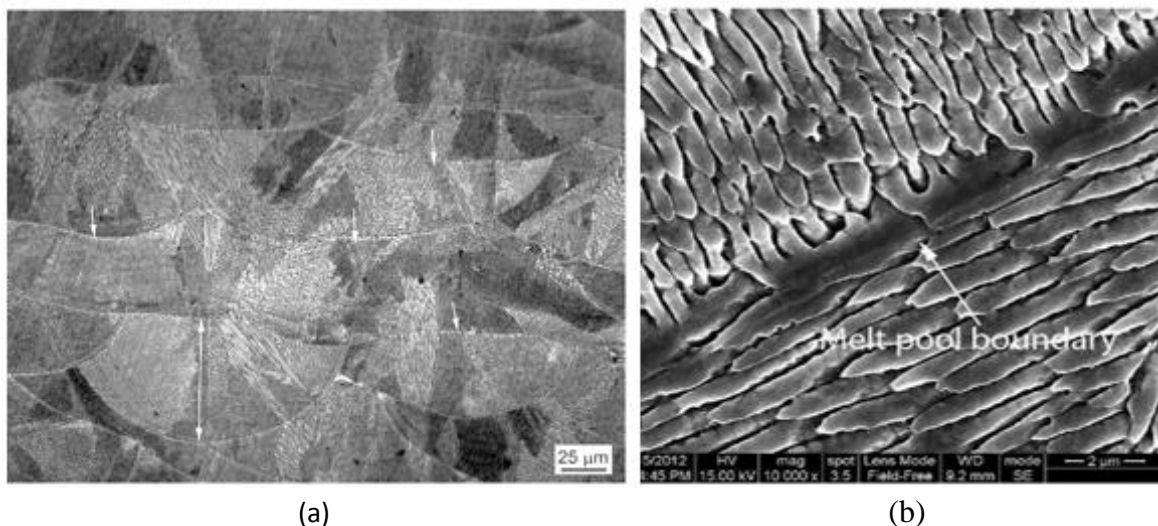


Figure 29: Optical (a) and scanning electron (b) micrographs showing microstructure typical for SLM process and strongly oriented, fine austenite grains in 17-4PH stainless steel (Rafi *et al.*, 2014).

Analysing and characterising of 17-4PH stainless steel SLM parts have been of interest recently. It is established that depending upon powder composition, processing atmosphere, process parameters, and heat treatment, the microstructure and phase compositions of 17-4PH stainless steel parts produced by SLM could be very different to those using conventional methods (Jerrard *et al.*, 2009; Starr *et al.*, 2012; Murr *et al.*, 2012; Gu *et al.*, 2013; Rafi *et al.*, 2014; Yadollahi *et al.*, 2015; and Hu *et al.*, 2017). Figure 30 shows a comparison between the as-built microstructure and the recrystallised microstructure of 17-4PH stainless steel obtained

after heat treatment. After solution annealing for 30 min at 1040 °C and air cooling to room temperature, followed by aging H900 at 482 °C, the fully recrystallised microstructure was achieved (Figure 30b). The boundaries of single layers and tracks had completely vanished.

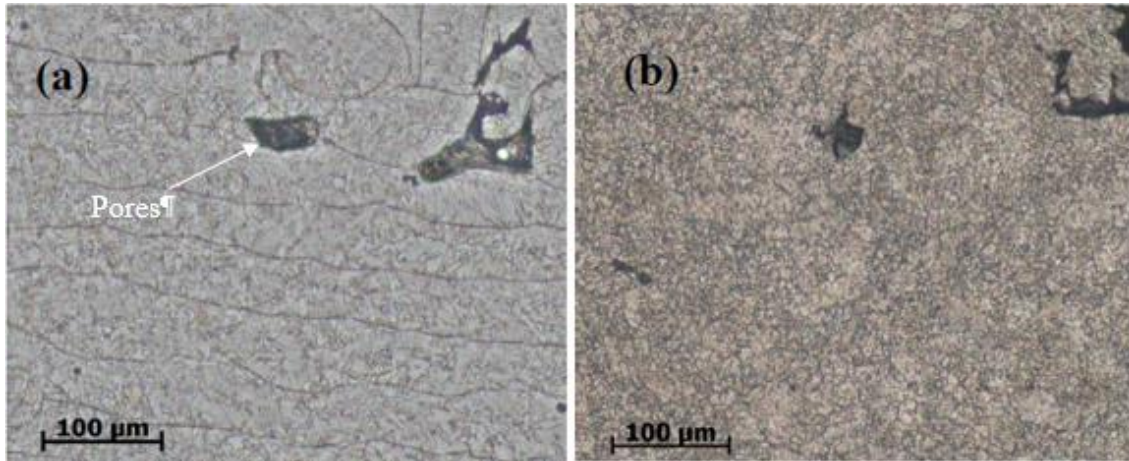


Figure 30: Cross-sectional optical images of SLM 17-4PH stainless steel; (a) as-built, and (b) heat treated (Yadollahi *et al.*, 2015).

2.3.3 Mechanical properties

Given the complex microstructure of SLM parts (i.e. complex crystal growth direction), the parts manufactured by SLM present unique mechanical properties. Their mechanical properties and performance are still being investigated and understood. Much of the literature on SLM focuses on mechanical properties and specifically on tensile behaviour and hardness. Tensile tests to measure yield strength, ultimate tensile strength and elongation are the most commonly used tests to compare SLM mechanical properties to traditionally processed materials (i.e. cast and wrought).

In most cases, the tensile strength of SLM parts are similar or exceed those of wrought and cast materials mainly because of the structure refinement linked to the rapid cooling rates experienced during the manufacturing process. Like wrought materials, the mechanical properties are also found to depend on the building orientation during manufacture. The strong anisotropy is believed to be associated with the residual stresses in the part, and the unique microstructure of SLM parts (Shifeng *et al.*, 2012; Vrancken *et al.*, 2014). Nevertheless, heat treatment has to be proven to effectively reduce anisotropy. Table 8 shows typical mechanical properties of SLM manufactured 17-4PH stainless steel in various conditions.

Table 8: Typical mechanical properties of 17-4PH stainless steel manufactured by SLM (Gratton *et al.*, 2012; Mahmoudi *et al.*, 2017; Mower and Long, 2016; and EOS, material datasheet_17-PH)

Mechanical properties	As-built	Stress relieved (1 hour at 650 °C)
UTS in the horizontal direction, XY	min 850 MPa typical 930 ± 50 MPa	typical 1100 MPa
UTS in the vertical direction, Z	min 850 MPa typical 960 ± 50 MPa	typical 980 MPa
LYS in the horizontal direction, XY	min 530 MPa typical 586 ± 50 MPa	typical 590 MPa
LYS in the vertical direction, Z	min 530 MPa typical 570 ± 50 MPa	typical 550 MPa
UYS in the horizontal direction, XY	min 595 MPa typical 645 ± 50 MPa	typical 634 MPa
UYS in the vertical direction, Z	min 580 MPa typical 630 ± 50 MPa	typical 595 MPa
Young's modulus	170 ± 30 GPa	typical 180 GPa
Elongation at break in the horizontal direction, XY	min 25% typical 31 ± 5%	typical 29%
Elongation at break in the vertical direction, Z	min 25% typical 35 ± 5%	typical 29%
Hardness as built	approx. 230 ± 20 HV1	
Hardness polished	approx. 250–400 HV1	

2.4 Summary

This chapter presented the literature review on different topics such as the physical phenomena and key process parameters in SLM and their effects on the manufactured parts, and the metallurgical background information on traditional 17-4PH stainless steel. It was shown that the SLM process is complex and involves a combination of many different physical phenomena which affect the final properties of the manufactured part. Some of these physical phenomena presented are full melting of the powder and substrate material, vaporisation, Marangoni

convection, Plateau-Rayleigh instability, wetting, balling, epitaxial solidification and anisotropy, and residual stresses. It must be pointed out that understanding the link between these physical phenomena and the SLM process parameters is crucial since the final properties of the manufactured part greatly depend on them. With regard to 17-4PH stainless steel, the literature shows that traditional 17-4PH stainless steel is widely used in the aeronautical, aerospace, chemical and petrochemical industries, as well as the marine and energy sectors, due to its outstanding combination of high strength and good corrosion properties at high temperatures, up to 300 °C. It was also shown that the microstructure of traditional 17-4PH stainless steel is different to the one obtained in the SLM as-built condition because of highly localised heat inputs, very short interaction times and local heat transfer conditions in the SLM process. These SLM conditions promote a non-equilibrium solidification process and enhance the limitation of solid solubility, refinement of grains and the formation of metastable phases. Lastly, it was revealed that mechanical properties of 17-4PH stainless steel, traditional and SLM, can be varied by applying different heat treatments such as stress-relieving, solution annealing and age-hardening. The mechanical properties obtained after age-hardening treatment are superior due to the formation of fine copper precipitates inside the matrix.

CHAPTER 3 – MATERIALS AND METHODS

Introduction

This chapter presents the characteristics of the material used in the study and the framework that outlines the methods that were followed. The equipment used to analyse the results is briefly described as well.

3.1 Metal Powder Characterisation

Gas-atomised 17-4PH stainless steel powder supplied by EOS GmbH was used to conduct the experiments. The characteristics of the powder, such as the particle size distribution (PSD) and surface morphology, were examined as follows:

3.1.1 Particle size distribution

The particle size distribution of the powder was determined using laser diffraction technique. This technique measures the particle size distribution by measuring the angular variation in the intensity of light scattered as a laser beam passes through a dispersed particulate sample. Large particles scatter light at small angles relative to the laser beam and small particles scatter light at large angles, as illustrated in Figure 31. The angular scattering intensity data is then analysed to calculate the size of the particles responsible for creating the scattering pattern, following the Fraunhofer diffraction theory stating that the intensity of light scattered by a particle is directly proportional to the particle size (Beuselinck *et al.*, 1998; and Storti and Balsamo, 2010). The particle size is reported as a volume equivalent sphere diameter. The equipment used in this study is shown in Figure 32.

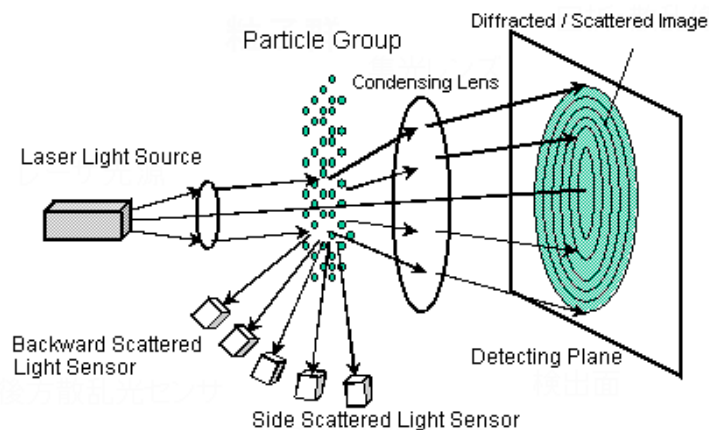


Figure 31: A schematic of a laser diffraction particle size analyser (<http://www.shimadzu.com/an/powder/support/practice/p01/lesson22.html>)

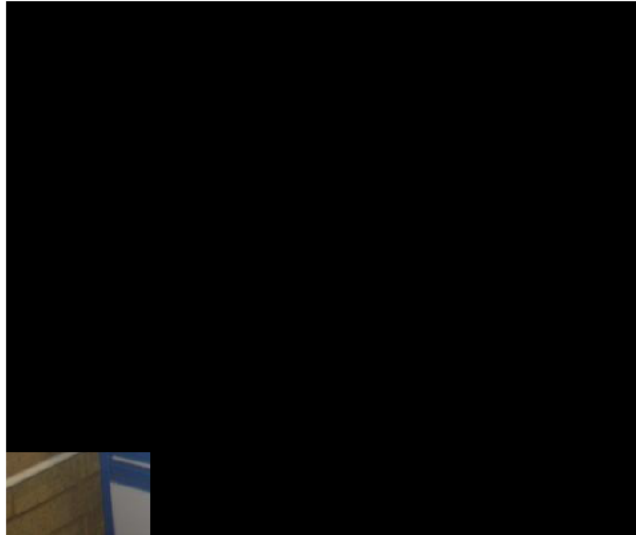


Figure 32: Microtac Bluewave/S3500-SDC particle size analyser

Figure 33 shows the particle size distribution of the powder. The particle size distribution was found to range from 20 μm to approximately 100 μm . The percentile distribution presented in Table 9 shows that the 10th, 50th and 90th percentiles of equivalent diameters are 30.5 μm , 43.0 μm and 64.1 μm respectively. The size, shape and distribution of the powder particles play an important role in SLM. The ratio of the larger to smaller particles in the powder can dictate the flowability (Kurzynowski *et al.*, 2012).

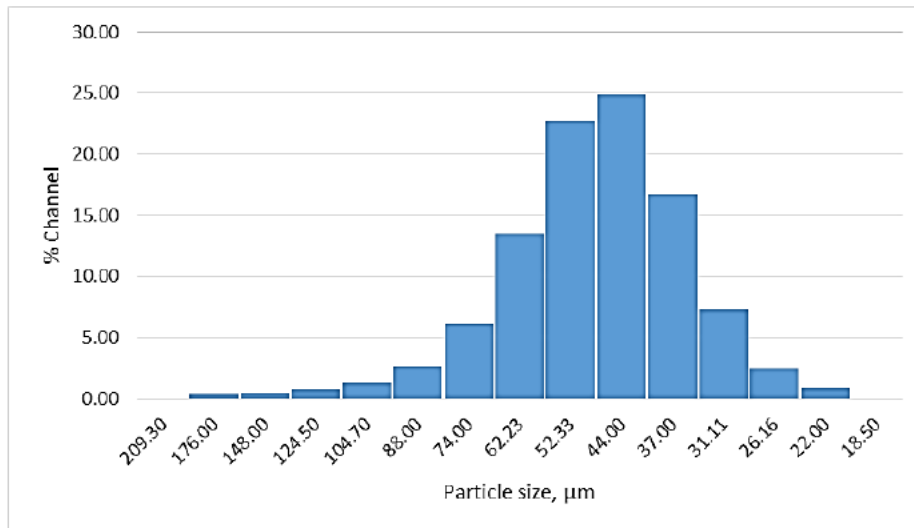


Figure 33: The particle size distribution of 17-4PH powder.

Table 9: Percentiles of the 17-4PH powder (weighted by volume)

Percentile (%)	Particle size (µm)
10	30.5
20	34.4
30	37.4
40	40.2
50	43.0
60	46.1
70	49.8
80	54.8
90	64.1
95	75.5

3.1.2 Surface morphology

The morphology of the powder was revealed using JEOL JSM6010/LA Plus scanning electron microscope (SEM). In SEM, the specimen is exposed to a narrow electron beam from an electron gun, which rapidly moves over or scans the surface of the specimen (Figure 34). This causes the release of a shower of secondary electrons and other types of radiation from the specimen surface. The intensity of these secondary electrons depends upon the shape and the chemical composition of the irradiated object. These electrons are collected by a detector which generates electronic signals that can be used to obtain information about the surface topography and composition of the material (Reichelt, 2007). The equipment used is shown in Figure 35.

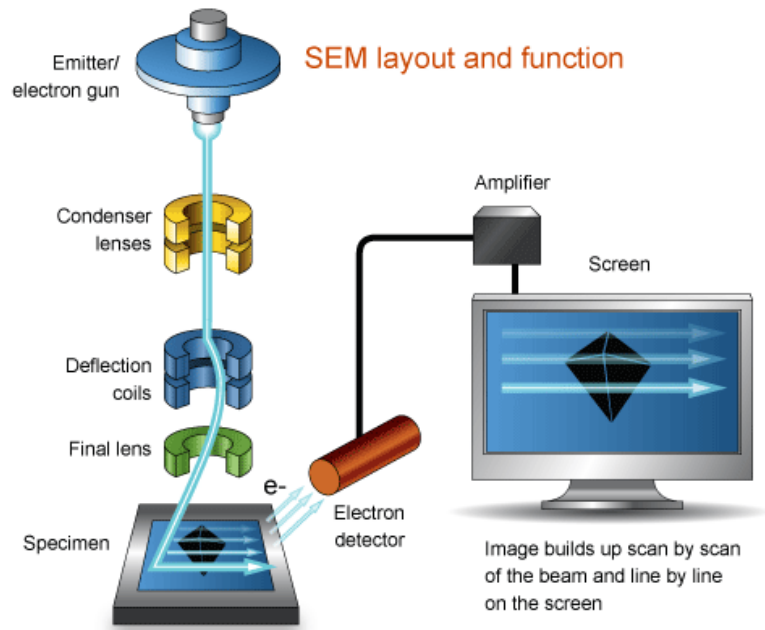


Figure 34: A schematic of a Scanning Electron Microscope (<http://www.ammrf.org.au/myscope/sem/practice/principles/layout.php>).

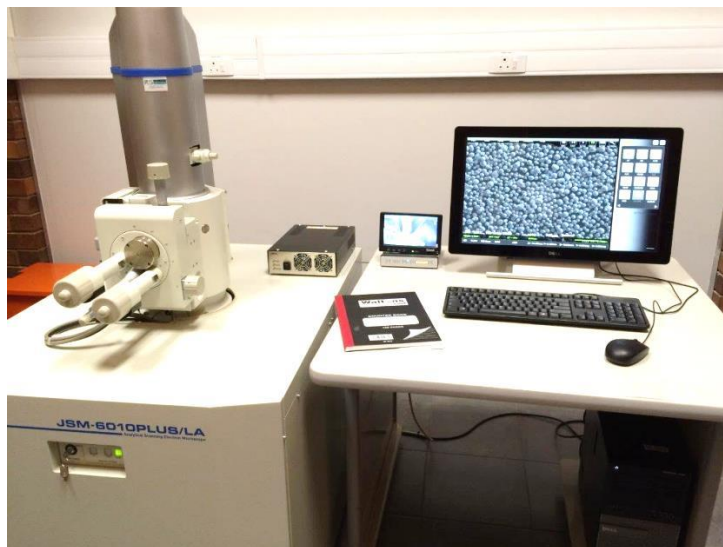


Figure 35: JEOL JSM6010/LA Plus Scanning Electron Microscope.

The 17-4PH powder is shown at different magnifications in Figure 36. Most particles were spherical in shape and have a smooth surface, typical of powders produced by the gas-atomisation process. The spherical morphology is preferred in SLM since it improves powder flowability and packing density (Cacace *et al.*, 2017).

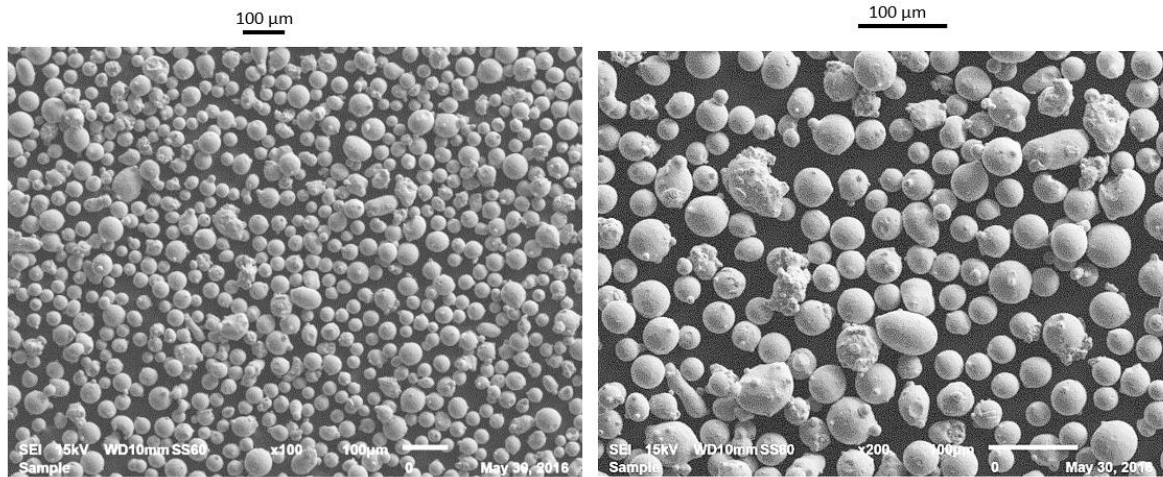


Figure 36: SEM micrographs showing particle shape at different magnifications.

Analysis of SEM photos did not show particles bigger than 100 μm in diameter in comparison with Figure 33, where very big particles were found by PSD analyser (>100 μm). Generally, d_{50} was 43 μm which is near 36–44 μm suggested by EOS for this type of powder (https://www.eos.info/eos_binaries0/eos/5d5320af77f01059/04ec9803958f/EOS-Stainless-Steel-17-4PH_IndustryLine_EN.pdf).

3.2 Manufacturing of samples

The purpose of this study was to investigate stability of single tracks during SLM of 17-4PH stainless steel by keeping constant laser power density, which is the ratio of laser power to spot area (Equation 8), by increasing the spot size and laser power. These data can be used further for increasing process efficiency of SLM.

$$P_d = P/A \dots \dots \dots \text{Equation 8}$$

where P_d is the laser power density, P is the laser power, and A is the effective spot size area.

Two SLM systems, equipped with 80 μm and 240 μm fixed spot size respectively, were used for this purpose. The 80 μm spot size was achieved by using a commercial SLM machine, EOSINT M280, with laser powers varying between 100 to 300 W. The 240 μm spot size was achieved by using an in-house made SLM set-up, with laser powers varying between 900 to 2700 W. In both cases the scanning speed was varied between 0.4 to 2.8 m/s. For comparison purposes, it was decided to preserve the power density in both cases. Figure 37 shows the design that was employed. The experiments were carried out in a controlled atmosphere (i.e.,

argon gas) containing less than 500 ppm oxygen. Further details of these experiments are provided in the following sections.

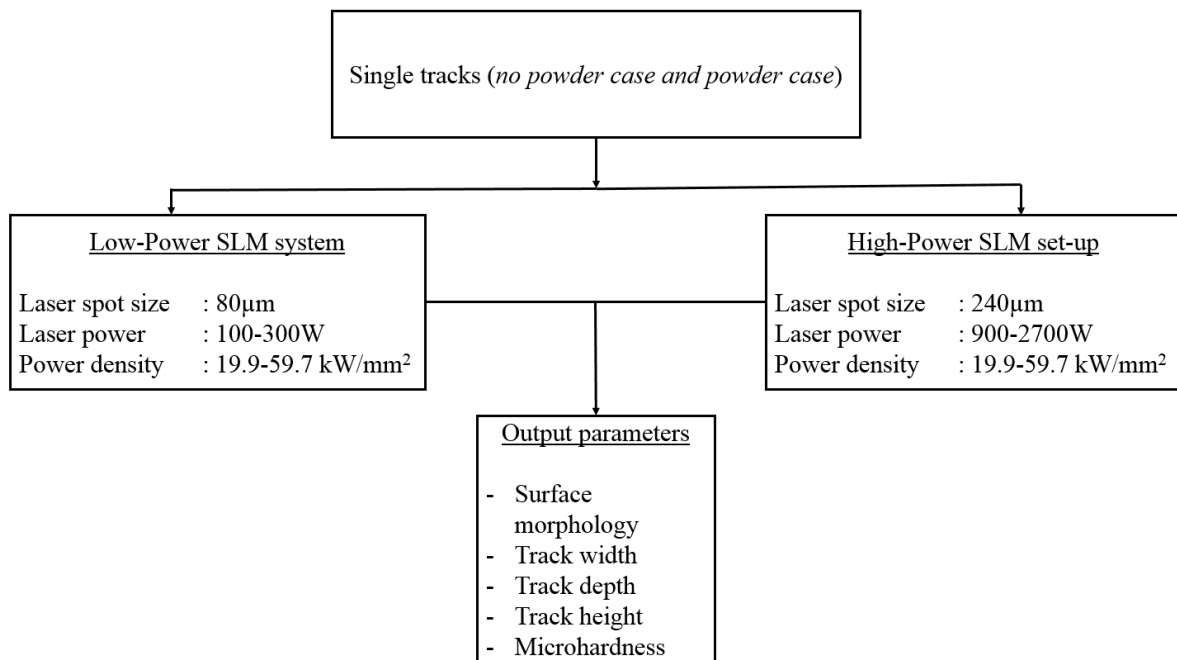


Figure 37: Design of experiments.

3.2.1 Low-power system

EOSINT M280, shown in Figure 38, is a commercial system equipped with a single-mode continuous-wave Ytterbium fibre laser, operating at 1075 nm wavelength and a spot size of 80 µm. The nominal power of the system is 400 W. The parameters that were used to manufacture the tracks are shown in Table 10.

Table 10: Parameters employed on the low-power system

Laser power (W)	<i>100</i>	<i>150</i>	<i>200</i>	<i>300</i>
Laser power density (kW/mm²)	<i>19.9</i>	<i>29.8</i>	<i>39.8</i>	<i>59.7</i>
Scanning speed (m/s)	0.4	0.6	0.8	1.2
	0.5	0.8	1.0	1.4
	0.6	1.0	1.2	1.6
	0.7	1.2	1.4	1.8
	0.8	1.4	1.6	2.0
	0.9	1.5	1.8	2.2
	1.0	1.6	2.0	2.4
	1.2	1.8	2.2	2.6
1.4	2.0	2.4	2.8	



Figure 38: EOSINT M280 SLM system.

3.2.2 High-power system

The high-power SLM equipment shown in Figure 39 is equipped with a multi-mode continuous-wave Ytterbium fibre operating at a wavelength of 1071 nm and a fixed spot size of 240 μm . The nominal power of this system is 5000 W. The parameters that were used with this machine are shown in Table 11.

Table 11: Parameters employed on the high-power system.

Laser power (W)	<i>900</i>	<i>1350</i>	<i>1800</i>	<i>2700</i>
Laser power density (kW/mm²)	<i>19.9</i>	<i>29.8</i>	<i>39.8</i>	<i>59.7</i>
Scanning speed (m/s)	0.4	0.6	0.8	1.2
	0.5	0.8	1.0	1.4
	0.6	1.0	1.2	1.6
	0.7	1.2	1.4	1.8
	0.8	1.4	1.6	2.0
	0.9	1.5	1.8	2.2
	1.0	1.6	2.0	2.4
	1.2	1.8	2.2	2.6
1.4	2.0	2.4	2.8	

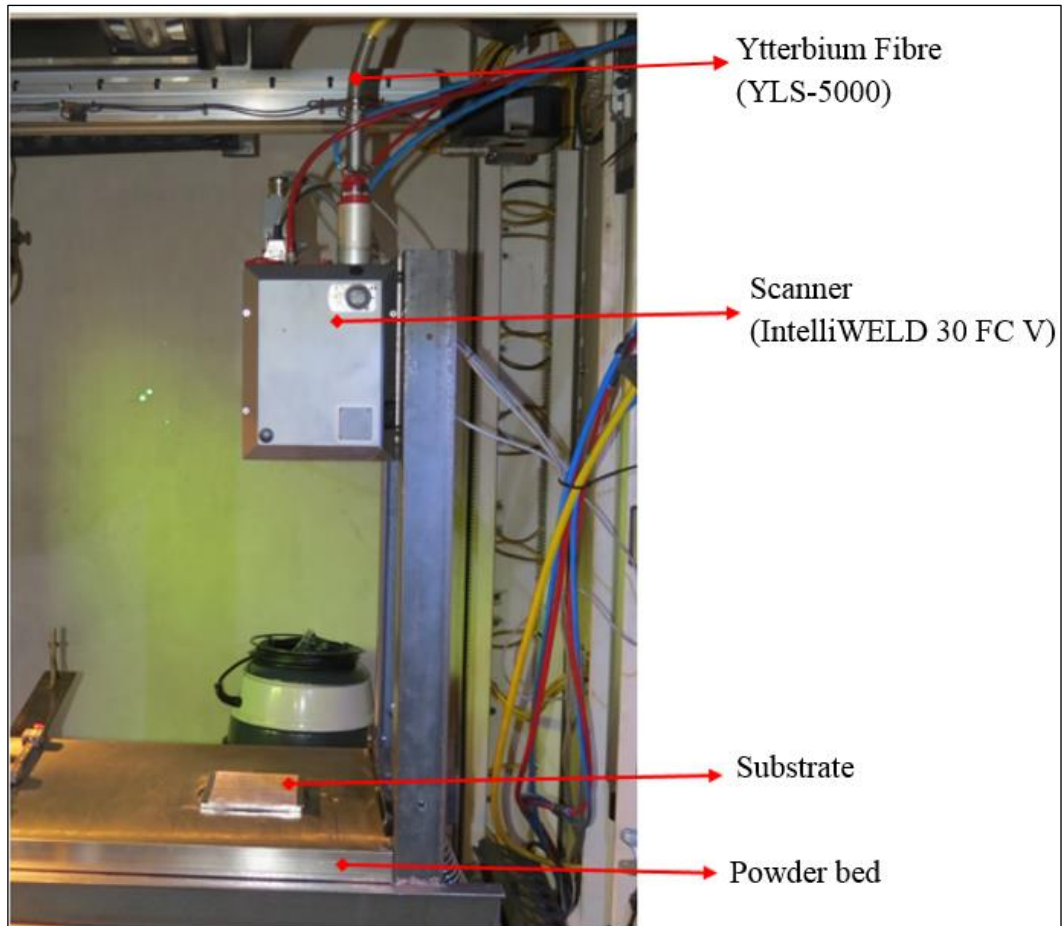


Figure 39: High-power SLM set-up.

3.3 Analysis equipment

The base plate used to manufacture the tracks, also 17-4PH stainless steel, was first sectioned into templates using an abrasive cut-off machine. These samples were then prepared using standard metallographic techniques in order to examine the surface morphology and melt pool profiles of tracks.

3.3.1 Abrasive cut-off machine

Struers DISCOTOM-2 was used for rapid cutting. The cutting operation was performed with a rotating wheel made of Al_2O_3 (i.e. Corundum H-type), the cut and wheel being cooled with a recirculating coolant. Figure 40 shows the machine and the cut-off sample.



Figure 40: Struers DISCOTOM-2 and the cut-off sample.

3.3.2 Automatic mounting machine

The cut-off samples were mounted on the AMP 50 automatic mounting press using a transparent thermoplastic. The mounting temperature was set between 150 °C and 200 °C for 400 s, after which the sample was cooled to temperatures below 40 °C. Figure 41 shows the machine and the mounted sample.



Figure 41: AMP 50 and the mounted sample.

3.3.3 Automatic grinding and polishing machine

The samples were ground and polished using Struers TegraPol-25 shown in Figure 42. Grinding and rough polishing was accomplished by using 80 to 1200 grit SiC papers, while fine polishing was performed on a micro-cloth using 9 to 3 μm water-based diamond suspension followed by colloidal silica for final polishing. Modified Fry's reagent (i.e. 150 ml H_2O + 25 ml HNO_3 + 1 g CuCl_2) was used to etch the samples. Each sample was etched using the swabbing technique for five seconds.



Figure 42: Struers TegraPol-25.

3.3.4 Optical microscope

Olympus BX51M microscope, shown in Figure 43, was used to photograph the morphology and geometrical characteristics of the single tracks. The width, depth and height of the single tracks were measured with Stream Essentials software, which was also used for imaging. Figure 44 shows a schematic diagram for track dimension measurements.



Figure 43: Olympus BX51M microscope.

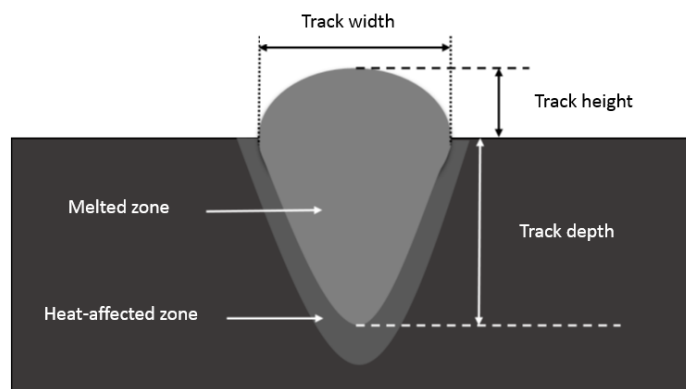


Figure 44: Schematic diagram showing melt pool profile and geometry.

3.3.5 Microhardness tester

Zwick-Roell ZHV μ , shown in Figure 44, is an automatic microhardness testing machine which was used to determine the hardness of the melt pool after solidification. The hardness is measured by indenting the sample with a diamond indenter that is, in the form of a prism. The diamond is pressed onto the surface of the material at a test load of 0.025 kg (HV0.025), with a dwell time of 10 seconds. The size of the impression is measured with the aid of a calibrated microscope and inserted into Equation 9 to determine the Vickers number (Dieter, 1986 and ASTM E385-11e1 Standard).

$$HV = 0.1891 \cdot F/d^2 \dots \dots \dots \text{Equation 9}$$

where F is the test load in N, and d is the arithmetic average value of the diagonal lengths of the indent in mm.

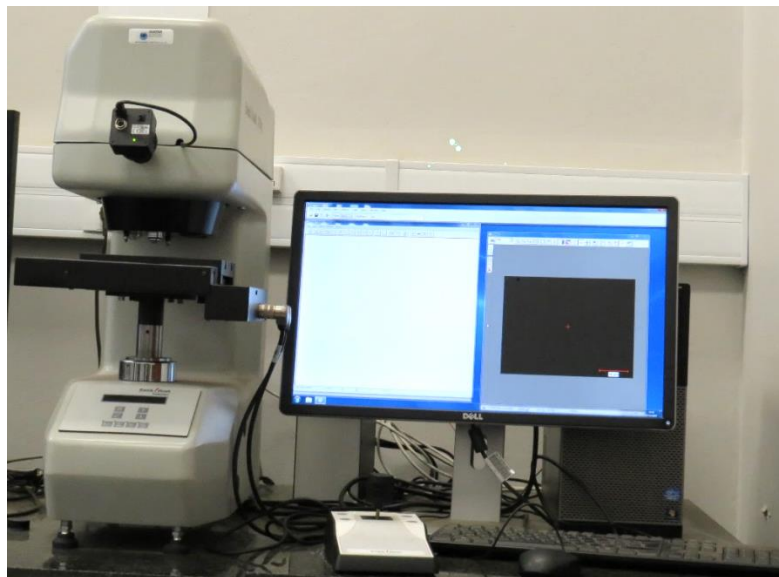


Figure 45: Zwick-Roel ZHV μ microhardness testing machine.

3.4 Numerical simulations of molten pool for single laser scan of the substrate

Temperature-dependent properties of the materials were used for numerical simulations of single lines produced by laser beam with Gaussian energy distribution on the solid substrate. The energy supplied by the laser beam with Gaussian distribution is defined by Equation 10

$$Q = Q_0(1 - R) \frac{2}{\pi r_0^2} e^{-\frac{2(x^2+y^2)}{r_0^2}} \dots\dots\dots\text{Equation 10}$$

where Q_0 is the total laser power; R is the surface reflectivity of material for given wavelength; r_0 is characteristic radius of laser beam; $x=x_0+Vt$, V – laser scanning speed.

The heat balance is

$$\rho c \left(\frac{\partial T}{\partial t} + V \nabla T \right) = \nabla (k \nabla T) + Q \dots\dots\dots\text{Equation 11}$$

where T is temperature, t is time and V is laser scanning speed, c is specific heat capacity, ρ is density of material, k is thermal conductivity. For numerical simulation, time-dependent “Heat Transfer in Solids” module of Comsol (ver. 5.2) was chosen in order to solve the heat balance equation.

Except for the top surface, all other boundaries are assumed to be thermally insulated. The heat flux on the top surface simulates convective cooling. Heat losses due to convection is expressed by Equation 12

$$k \frac{\partial T(x, y, L_z, t)}{\partial z} \Big|_{top} = h_c (T - T_0) \dots\dots\dots\text{Equation 12}$$

where $T_0 = 293$ K is initial temperature, $h_c = 10$ W/(m²K) is convection coefficient.

In order to obtain accurate results, the density of the mesh in the region around the irradiation and in the top region of the sample (100 μm) was higher than in the sample as a whole (refined mesh). Minimum element size in the mesh size was 0.5 μm. This approach for numerical simulation of molten pool by moving the laser beam was described in detail by Yadroitsev *et al.* (2015).

Temperature-dependent properties of 17-4PH stainless steel (Figure 47) were used for numerical simulations of single lines produced by the laser beam with Gaussian energy distribution on the solid substrate.

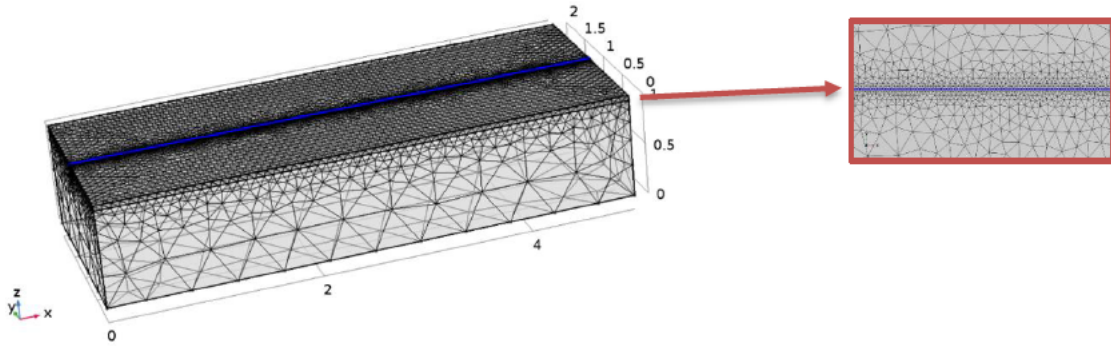


Figure 46. Free tetrahedral mesh with refinement region along laser scanning direction.

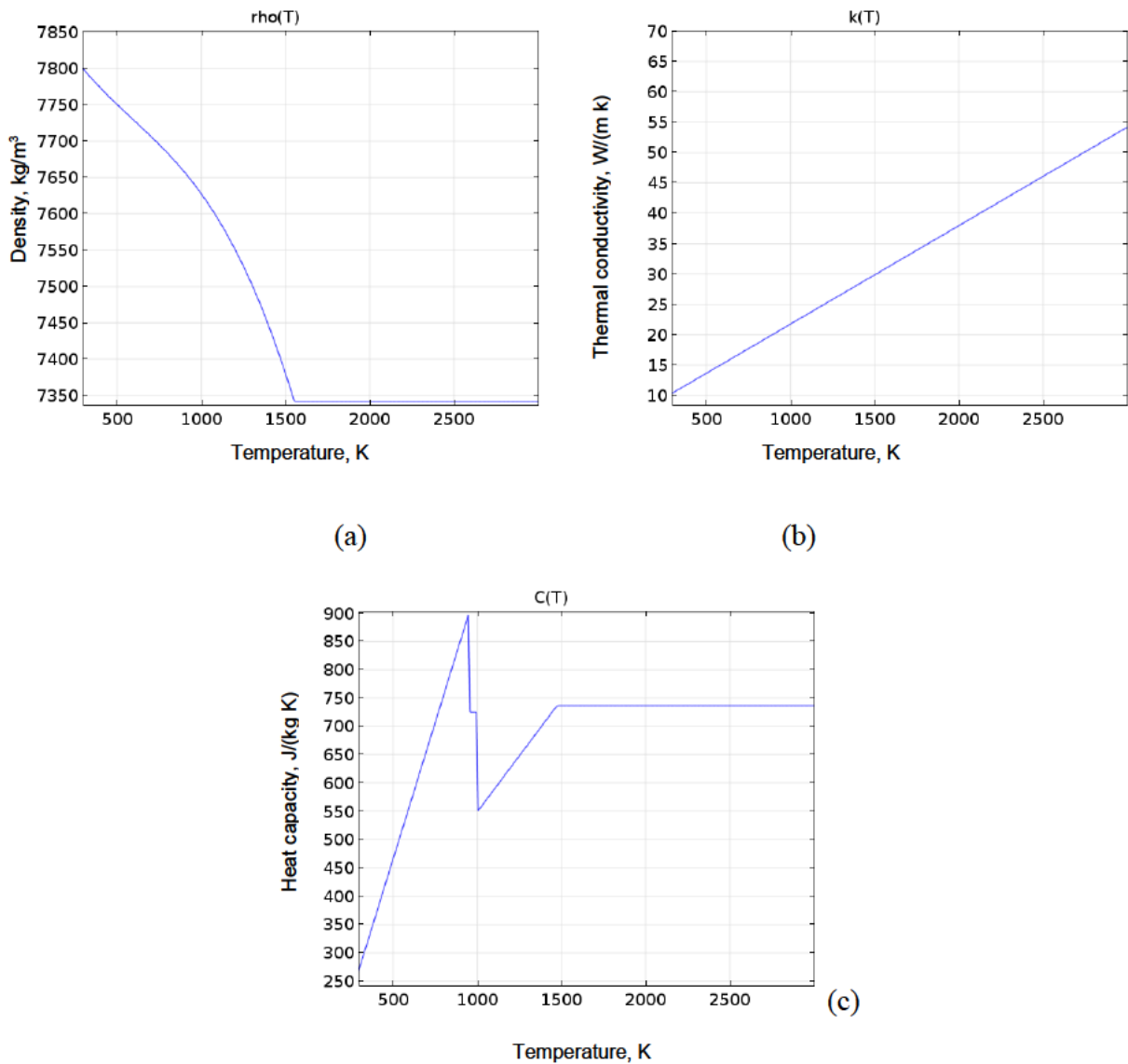


Figure 47. Temperature-dependent properties of 17-4PH stainless steel: density (a), thermal conductivity (b), heat capacity (c) (Rack, 1981; Comsol material database, 2015).

3.5 Summary

In this chapter, the materials and the framework that outlines the methods employed in the study were presented. The powder material used was gas-atomised 17-4PH stainless steel supplied by EOS GmbH. This material was characterised by applying laser diffraction technique and scanning electron microscopy. The laser diffraction results revealed that the 10th, 50th and 90th percentiles of equivalent diameters were 30.5 μm , 43.0 μm and 64.1 μm respectively; while the images from scanning electron microscopy showed that most particles were spherical in shape and had smooth surfaces. The two SLM systems which were used to conduct the experiments were also described. The first system is a commercial EOSINST M280 system, operating at 80 μm fixed spot size with a nominal power of 400 W. The other system is an in-house made SLM set-up operating at 240 μm fixed spot size with a nominal power of 5000 W. The equipment used to analyse the samples was also described. This equipment includes the abrasive cut-off machine which was used to section the substrates into smaller samples, an automatic mounting machine used to mount the sample with a transparent thermoplastic, an automatic grinding and polishing machine, an optical microscope used to reveal the molten pool and measure dimensions, and a microhardness testing machine used to measure the hardness of the molten pool and the substrate material. Lastly, the methods used for numerical simulations of molten pool for single laser scan of the substrate were presented.

CHAPTER 4 – RESULTS AND DISCUSSION

Introduction

In this chapter, the results obtained from the low- and high-power SLM systems used to manufacture the single tracks are presented and discussed. Analysis of results include characterisation of single tracks, both for the “no powder-” and “powder” cases; evaluating the effect of process parameters on the geometrical characteristics; and lastly, the effect of process parameters on the microhardness of the solidified tracks.

4.1 Characterisation of single tracks

4.1.1 “No powder” case

For the “no powder” case, the tracks were formed by re-melting and solidification of the base plate material. Generally, the surface morphology would change with varying the processing parameters. The following subsections present the results that were obtained from the low- and high-power SLM systems used in this study.

Low-power system

For the low-power system, three distinctive morphologies were observed when the laser power and scanning speed were varied. These morphologies are presented in Figure 48, with the corresponding melt pool profiles shown in Figure 49. Continuous tracks, showing ripples in an elongated pointed form, were formed when the laser power and scanning speed were varied between 100-150 W and 0.4-1.0 m/s respectively. Increasing the scanning speed beyond 1.0 m/s provoked the formation of undercutting-like defects, as seen in laser welding. This defect is characterised by dark parallel grooves along the side of the track, which can form either continuously or sporadically. The formation of undercuts is complex and occurs by various mechanisms, mainly based on temperature gradients and melt flow dynamics (Frostevarg and Kaplan, 2014). Expressed humping effect, characterised by severe undercuts and periodic droplets along the length of the track, was also observed at higher laser powers (i.e. 200–300 W) and scanning speeds above 1.2 m/s. This effect is believed to be caused by the superimposed production of melt back-flow accompanied by laser-induced plume and higher surface tension induced by the narrow melt pool width, which results in capillary instability of the liquid cylinder (Yadroitsev *et al.*, 2010; Soderstrom and Mendez, 2013).

Figure 50 summarises the results obtained for the different parametric conditions. In SLM, parameters which result in the formation of undercuts and humping cannot not be included in the optimal window, as these defects are more likely to provoke the formation of undesired pores in the final part.

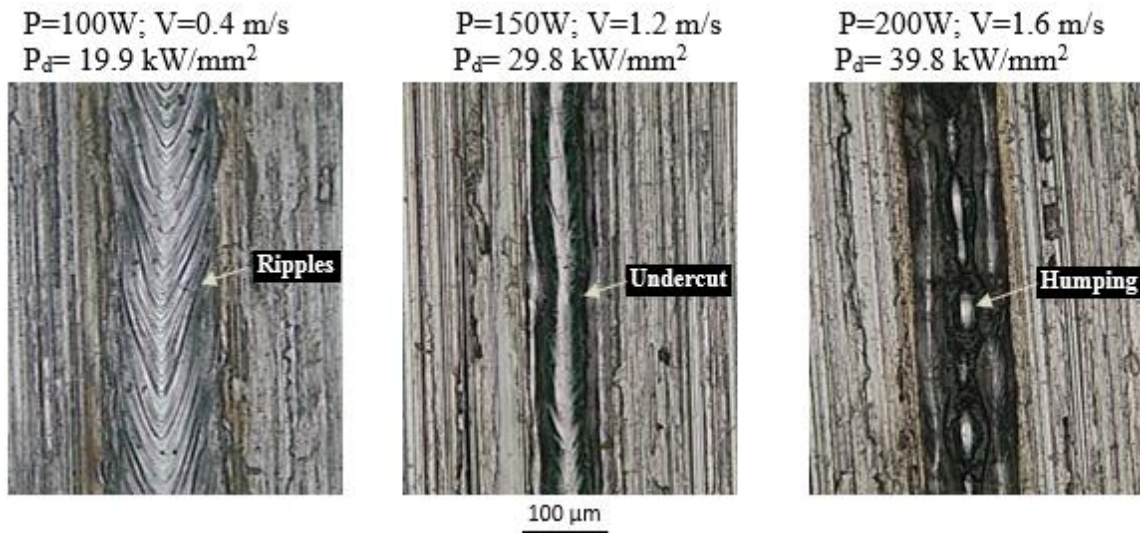


Figure 48: Top view morphologies for the low-power system “no powder” case.

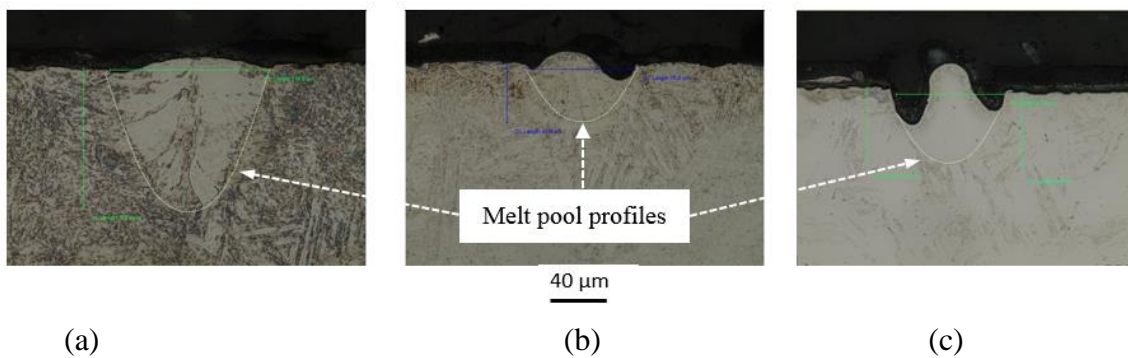


Figure 49: Corresponding cross-section views for the low-power system “no powder” case: with ripples on the track (a), with undercut profile (b) and strong humping effect (c).

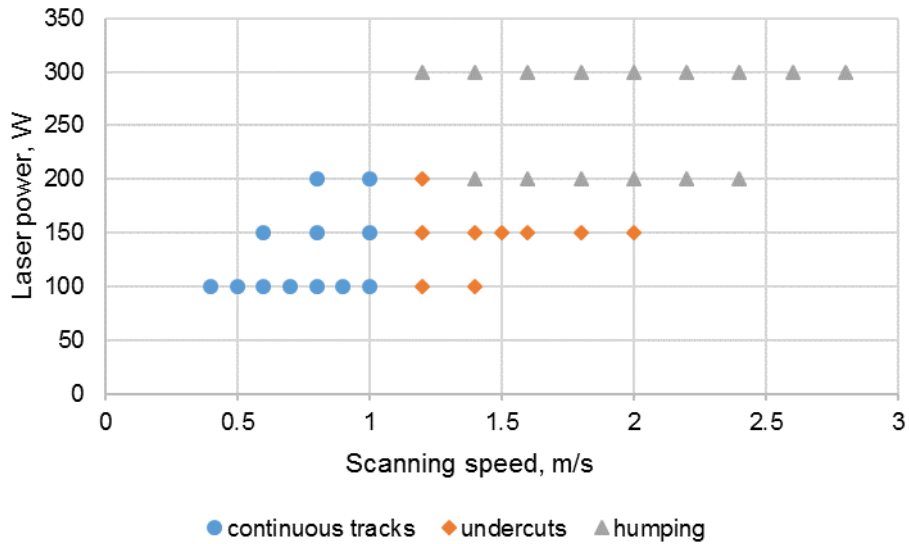


Figure 50: Summary of results obtained on the low-power system for “no powder” case.

High-power system

The three morphologies that are described above were also observed, with an additional morphology that was not observed previously. These morphologies are presented in Figure 51, while Figure 52 shows the corresponding melt pool profiles. Continuous tracks were formed at a laser power and scanning speed of 900 W and 0.4–0.6 m/s respectively. Further increase in the laser power and scanning speed resulted in the formation of undercuts and humping effect. The tracks produced at 1350 W all had humping effect, whereas 2700 W laser power generated spatter formation of the molten pool. As Khairallah *et al.* (2016) indicates, strong temperature gradients under the laser beam and complex hydrodynamic flows in the melt pool result in this shape of the track. The results obtained for different parametric conditions are summarised in Figure 53.

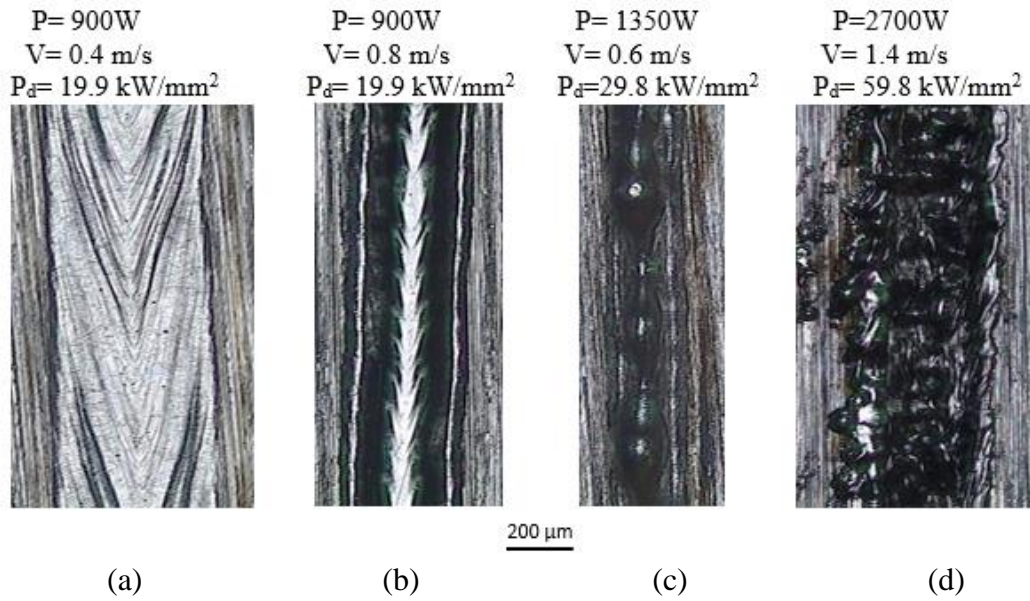


Figure 51: Top view morphologies for the high-power system “no powder” case.

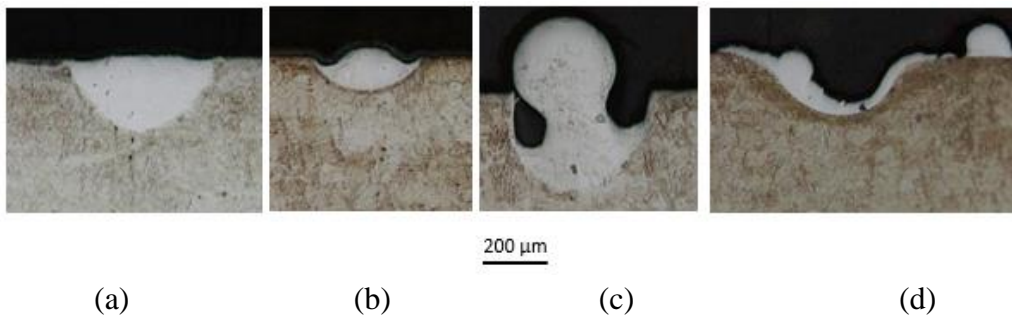


Figure 52: Corresponding cross-section views for the high-power system “no powder” case.

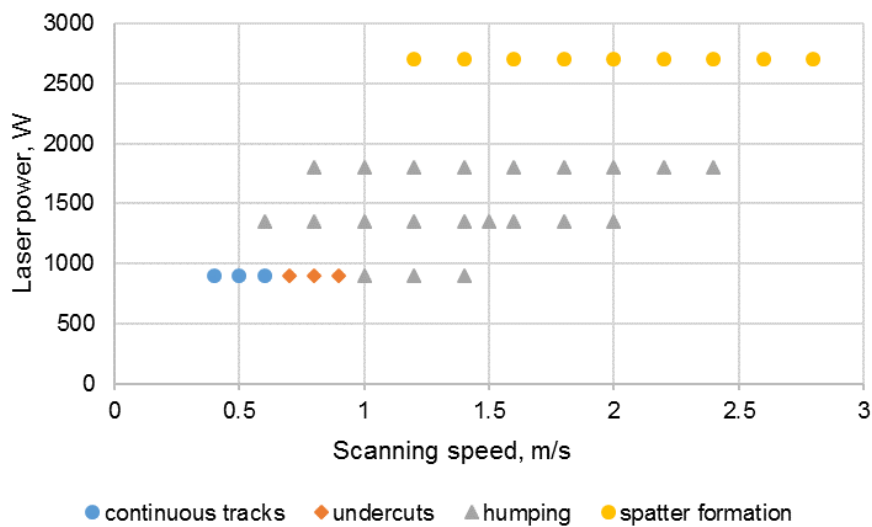


Figure 53: Summary of results obtained on the high-power system “no powder” case.

4.1.2 “Powder” case

For the “powder” case, single tracks were formed by melting powder and the base plate material, which formed a unified melt pool and solidified together. The layer thickness was kept at 50–75 μm for both systems.

Low-power system

Powder was delivered by lowering the base plate by 50 μm from the focal plane. This system uses a recoating blade to spread the layer (Figure 54). It is difficult to guarantee that the base plate was completely flat and perfectly levelled. Therefore, the layer thickness of the powder may have varied slightly above or below 50 μm .

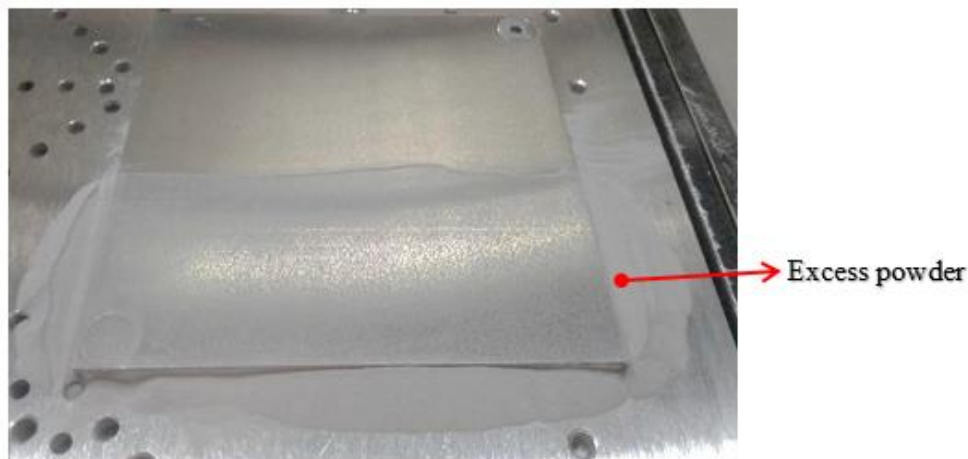


Figure 54: Powder layer deposited with the recoating blade.

Although the single tracks produced show similar surface morphologies and melt pool profiles, the surface roughness of the tracks was worse because of small particles sticking to the sides of the track. The surface morphologies observed are presented in Figure 55, with Figure 56 showing the corresponding melt pool profiles. At 100–200 W, the tracks produced were fairly continuous as the scan speed varied between 0.4–1.2 m/s. Non-uniform tracks, believed to be caused by strong dynamical melt flow, were observed at higher scanning speeds greater than 1.2 m/s. Childs *et al.* (2004) and Yadroitsev (2010) attribute the formation of non-uniform tracks in SLM to the Plateau-Rayleigh capillary instability of the molten liquid, while Dai and Gu (2015) believe that the thermo-capillary force and the recoil pressure induced by evaporation are the major causes. Yan *et al.* (2017) argued that single track nonuniformity is due to surface tension driven by the random attachment of molten pool to the partially melted

particles near the boundaries. Therefore, the formation of nonuniform tracks involves a combination of complex phenomenon. Balling effect was observed at 200–300 W, as the high scanning speed varied between 1.4–2.8 m/s. A summary of the results obtained is shown in Figure 57.

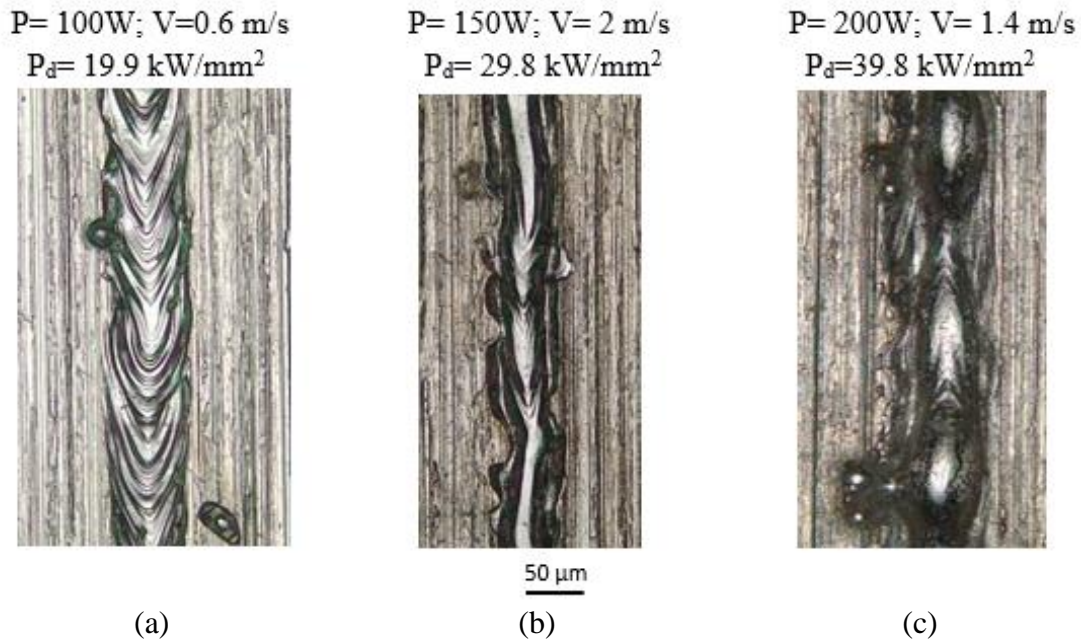


Figure 55: Top view morphologies for the low-power system “*powder*” case: stable track (a), irregular track (b) and balling effect (b).

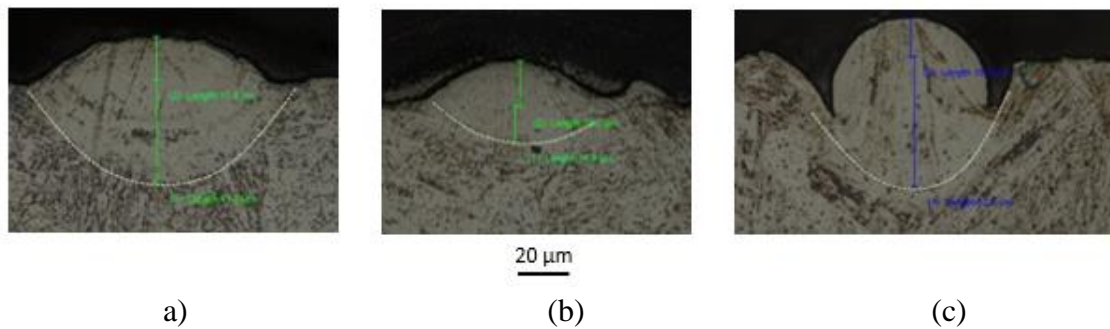


Figure 56: Corresponding cross-section views for the low-power system “*powder*” case: stable track (a), irregular track (b) and balling effect (c).

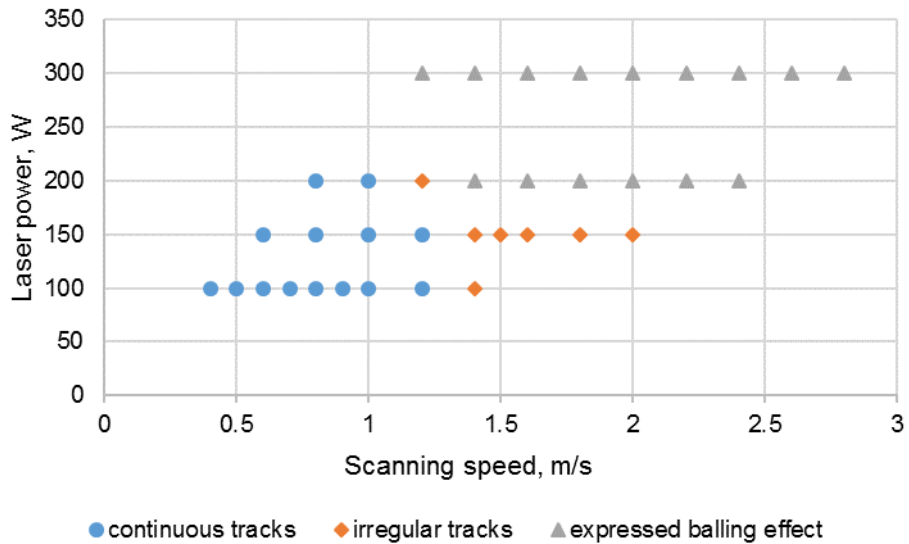


Figure 57: Summary of the results obtained for low-power system for the “powder” case.

High-power system

A solid scraper was used to manually deposit the 75 μm layer shown in Figure 58. The thickness was controlled by using shim stock sheets glued to the base plate to act as spacers against which the blade was pressed during the scraping. It is difficult to guarantee that the layer deposited was exactly 75 μm since this was done manually, and therefore human error is considered.

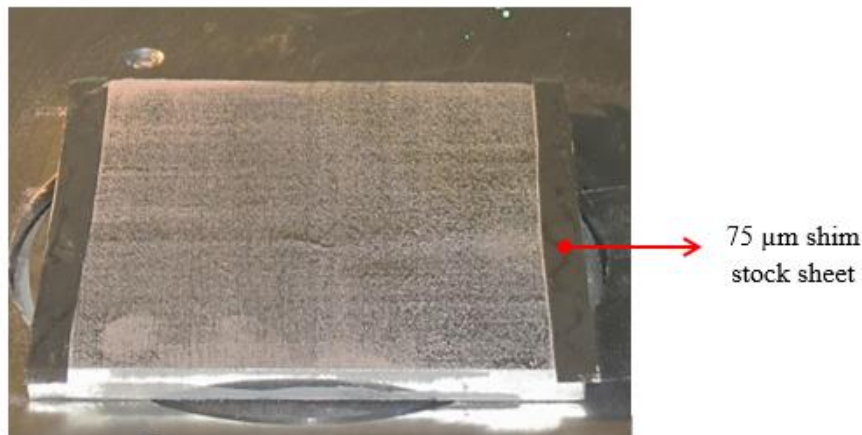


Figure 58: Powder layer deposited with a solid scraper for high-power studies.

Continuous tracks were only formed at 900 W when the scanning speed was varied from 0.4–0.5 m/s. All the other tracks formed revealed humping effect and severe material displacement, especially at 2700 W (Figure 59). The corresponding melt pool profiles are shown in Figure 60, while Figure 61 presents a summary of the results obtained for the various laser power

scanning-speed combinations. It is clear from Figure 57 and Figure 61 that the maximum scanning speed for continuous track formation is reduced for a bigger spot size. That is, at 240 μm spot size the maximum scanning speed is 0.5 m/s, whereas at 80 μm spot size the maximum scanning speed is 1.2 m/s. Since the 240 μm spot size is three times bigger, time of interaction (*i.e.* laser beam-matter) also increases three times at the same scanning speed. Longer periods of interaction together with high laser power lead to increasing temperature up to boiling point. Recoil pressure creates the indentation and spattering of the molten pool (Figure 62). These results corroborate with the findings of Miyamoto *et al.* (2003) and Miyamoto *et al.* (2004), who also discovered that humping occurs at much higher welding speeds when using a smaller spot size. Thomy *et al.* (2017) also highlighted that this unwanted effect is often observed at welding speeds as low as 0.17 m/s in macro welding with CO₂ lasers or solid state lasers, where, in general, spot diameters well exceed 150 μm .

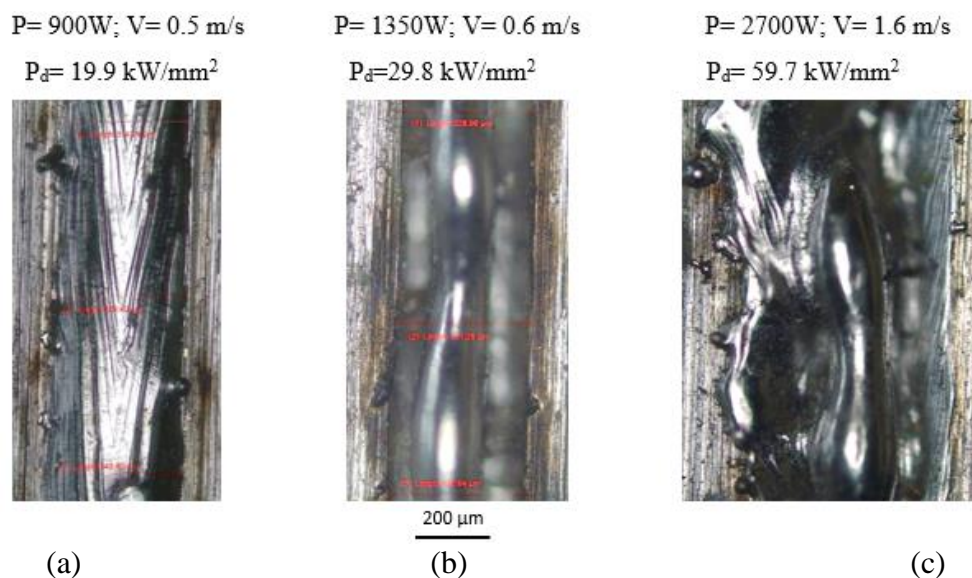


Figure 59: Top view morphologies for the high-power system “*powder*” case: stable track (a), irregular track/balling effect (b) and spatter formation (c).

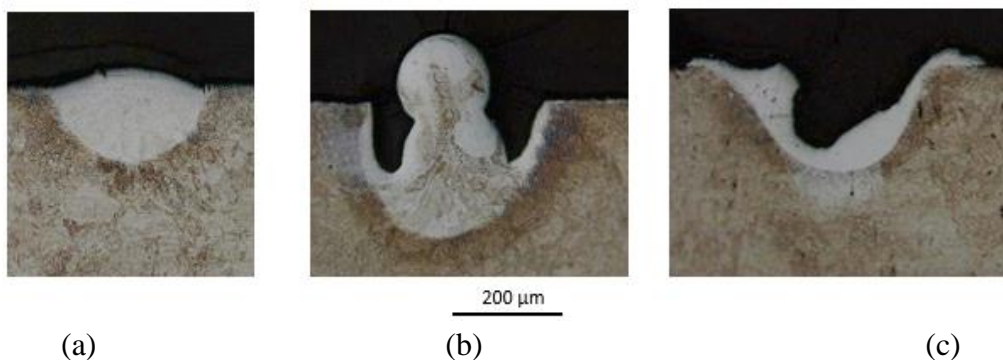


Figure 60: – Corresponding cross-section views for the high-power system “*powder*” case: stable track (a), irregular track/balling effect (b) and spatter formation (c).

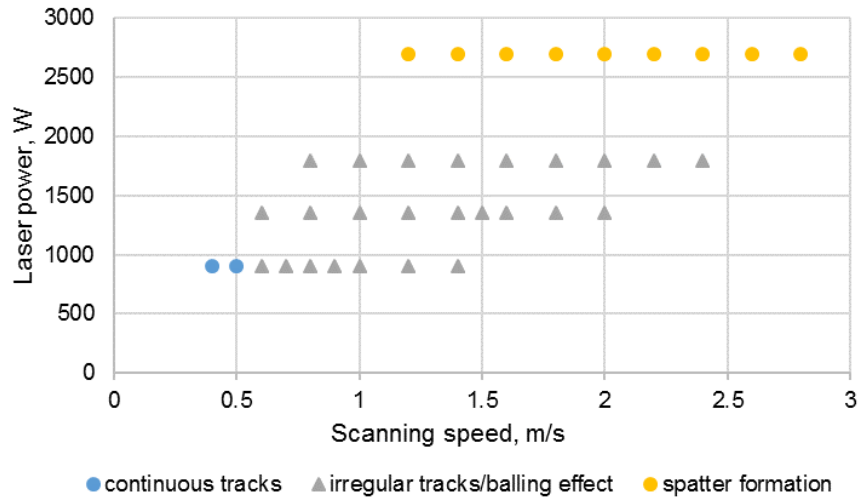


Figure 61: Summary of results obtained on the high-power system “*powder*” case.

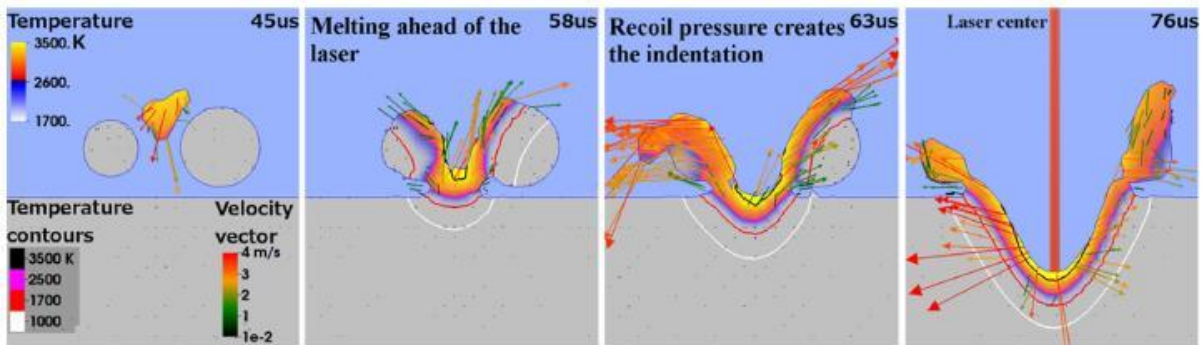


Figure 62: A depression in the molten pool below high laser beam and spatter formation (Khairallah *et al.*, 2016).

4.2 Geometrical characteristics *versus* parameters

The geometrical characteristics of the solidified melt pool, such as the width and penetration depth, were measured using the optical microscope. Single tracks produced on the low- and high-power systems are compared.

4.2.1 Width of the track

Numerical simulations showed that the width of the molten pool diminishes with scanning speed (Figure 63).

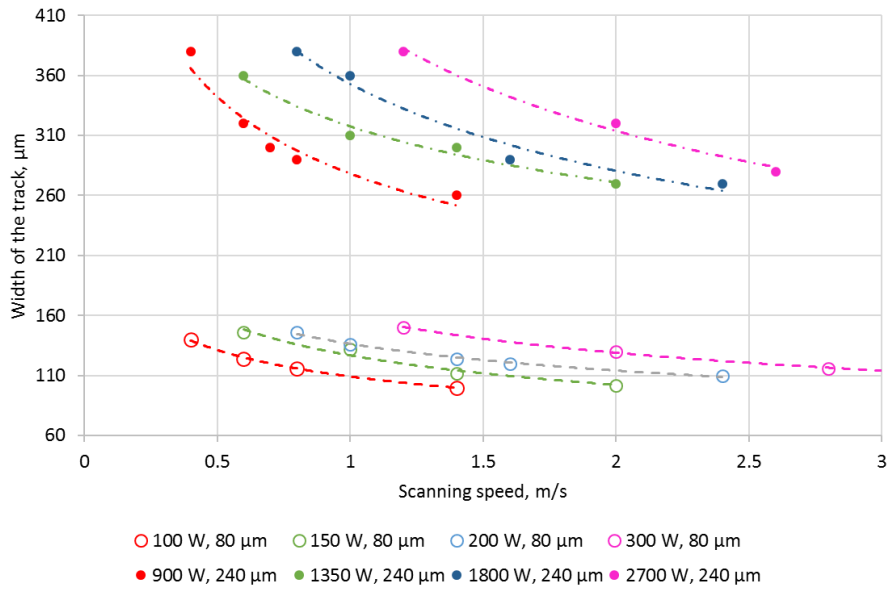


Figure 63: Calculated effect of scanning speed on the width of the track “no powder” case at different laser power and spot size.

Experimentally, the effect of scanning speed on the width of the track was evaluated by comparing single tracks manufactured at the same laser power density. Tracks manufactured at a power density of 19.9 kW/mm^2 are presented (laser power 100 W, 80 μm spot size and 900 W, spot diameter of 240 μm). Similarly, the effect of power density was evaluated by comparing single tracks manufactured at the same scanning speed of 1.4 m/s. Three measurements were taken on each track, and the results are presented in Figure 64 – Figure 67. The effect of scanning speed on the width of the track was generally the same for the “no powder” case and “powder” case; the width of the tracks is mainly defined by laser power and spot size. The width of the tracks also diminished with scanning speed, since scanning speed determines the time of laser beam–material interaction. It has to be mentioned that experiments with higher laser power (900–2700 W) were done on a thicker powder layer, so more powder particles were involved in the formation of molten pool in this case (Figure 65).

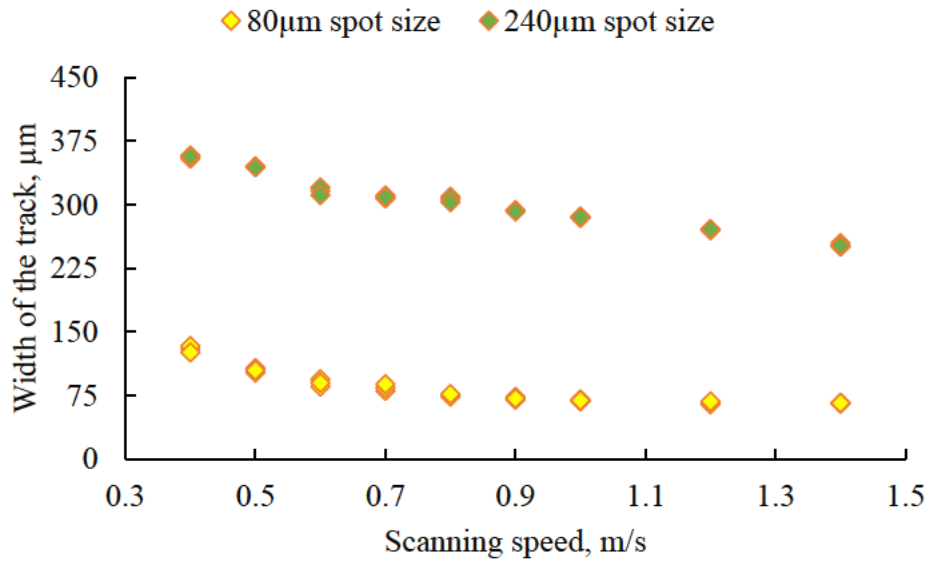


Figure 64: Effect of scanning speed on the width of the track “no powder” case for 19.9 kW/mm² (100 W and 900 W laser power).

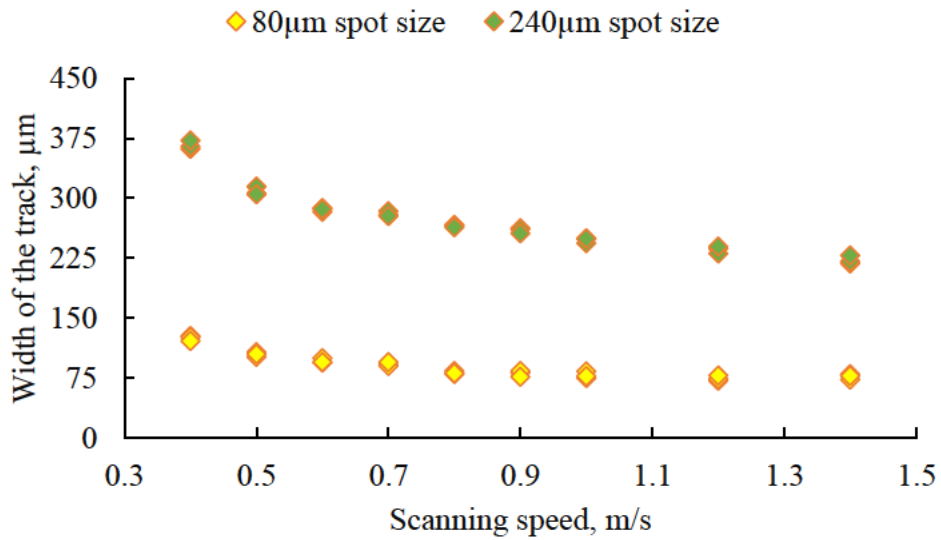


Figure 65: Effect of scanning speed on the width of the track “powder” case for 19.9 kW/mm².

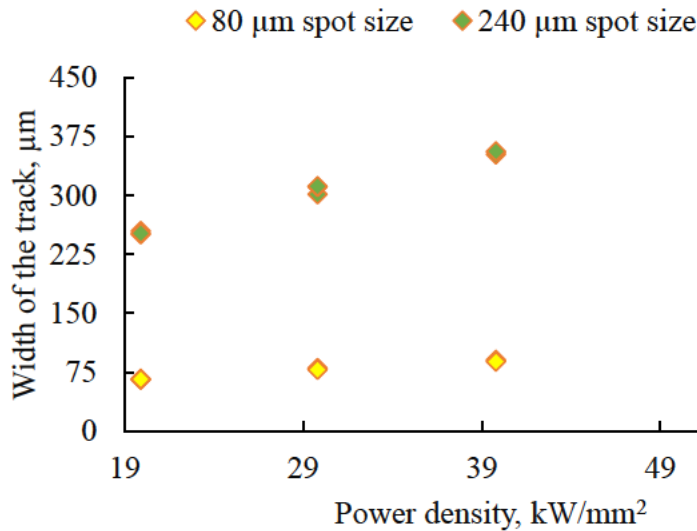


Figure 66: Effect of power density on the width of the track “no powder” case at laser scanning speed $V=1.4$ m/s.

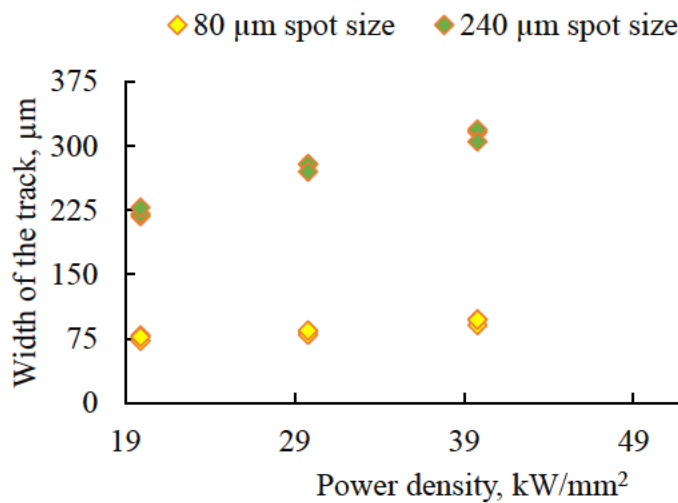


Figure 67: Effect of power density on the width of the track “powder” case at laser scanning speed $V=1.4$ m/s.

From the above results it can be seen that increasing the scanning speed leads to a decrease in the width of the track. The reason for this is mainly because the laser–material interaction time decreases as the scanning speed increases, thus the size of the molten pool also decreases. On the contrary, increasing the power density increases the width of the track. This is because increasing the power density increases the energy input, which in turn increases the size of the molten pool.

4.2.2 Penetration depth

Numerical simulations showed that the penetration depth of the molten pool also diminishes with scanning speed (Figure 68).

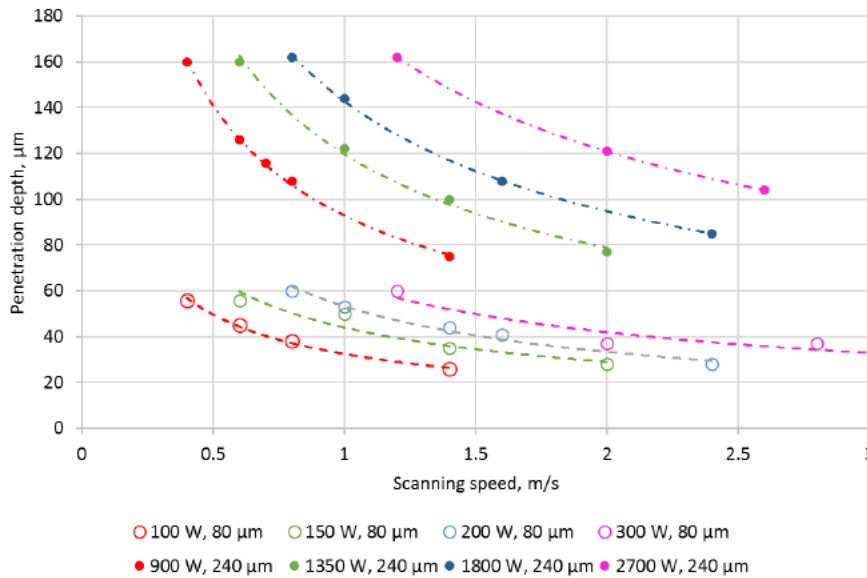


Figure 68: Calculated effect of scanning speed on the penetration depth of the molten pool for “no powder” case at different laser power and spot size.

The effect of scanning speed, powder density and spot size on the penetration depth is presented as follows.

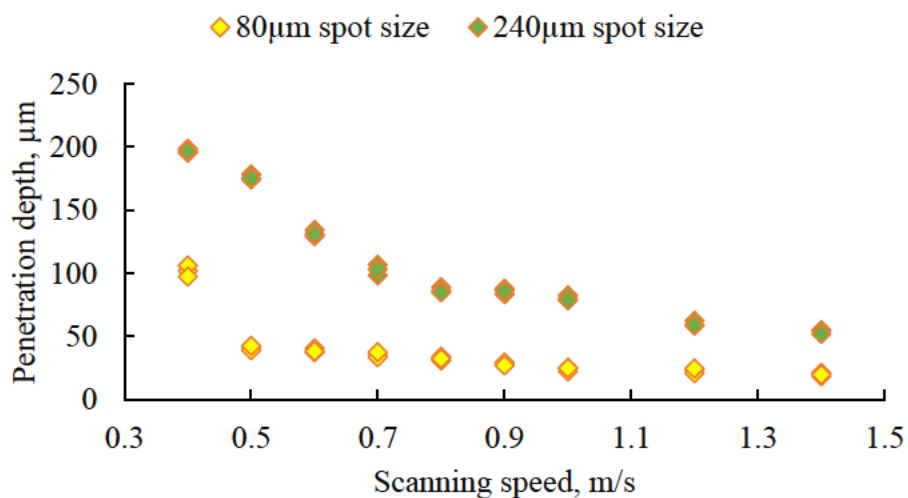


Figure 69: Effect of scanning speed on the penetration depth “no powder” case for 19.9 kW/mm².

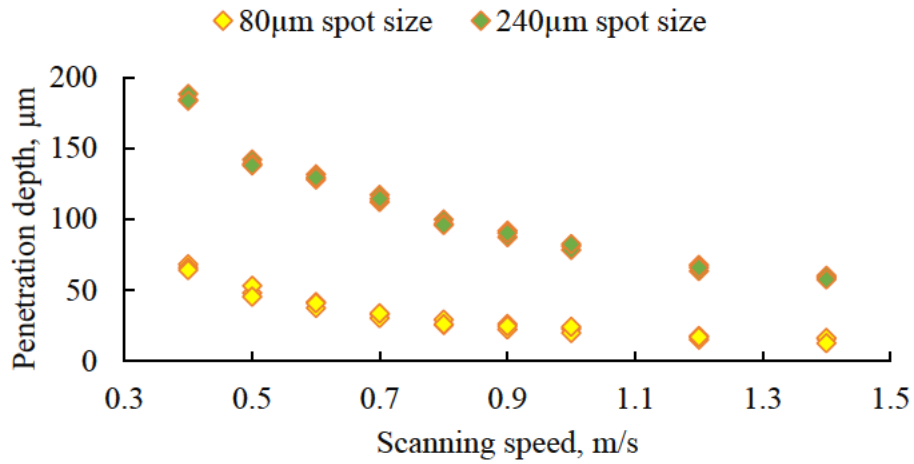


Figure 70: Effect of scanning speed on the penetration depth “*powder*” case for 19.9 kW/mm².

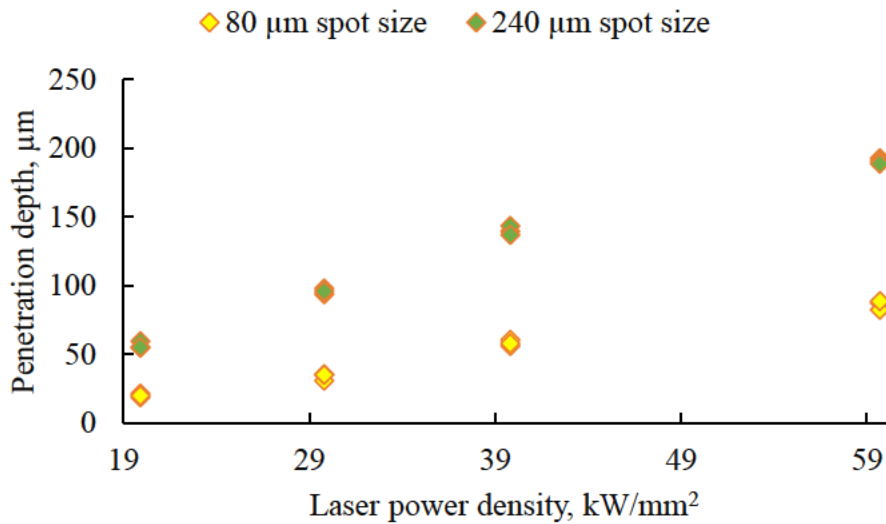


Figure 71: Effect of power density on the penetration depth “*no powder*” case at laser scanning speed $V=1.4$ m/s.

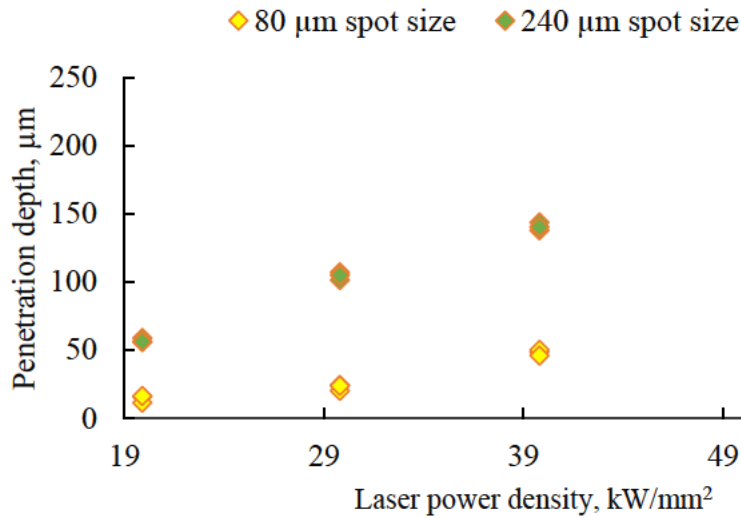


Figure 72: Effect of power density on the penetration depth “*powder*” case at laser scanning speed $V=1.4$ m/s.

The above results indicate that both laser power and interaction time significantly affect the penetration depth (Figure 68-72).

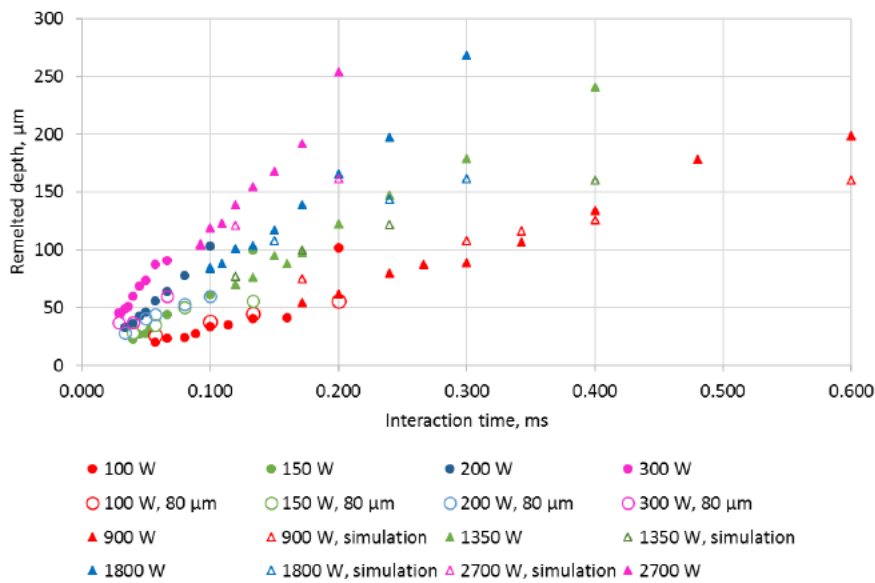


Figure 73: Effect of interaction time on the penetration depth for “*no powder*” case.

For constant laser power density, an increase in scanning speed leads to a decrease in penetration depth since the laser beam and material interact for a short time.

4.2.3 Track height

The track height is primarily determined by the thickness of the deposited layer and its apparent density. The height of the tracks was found to vary significantly. This is believed to be caused by non-homogeneity in the deposited layers, and strong melt pool hydrodynamics at high laser powers and scan speed which resulted in irregularities such as humping and nonuniformity.

4.2.4 Length of molten pool

At chosen process parameters, the length of the molten pool, at similar laser power densities for different laser spot size, varied significantly (Figure 74). Analysis of the length of molten pool *versus* scanning speed shows that the determining factor in the molten pool length is laser power. It should be assumed that a higher laser power leads to a higher temperature gradient, which, in turn, contributes to strong flows in the molten pool and splashes.

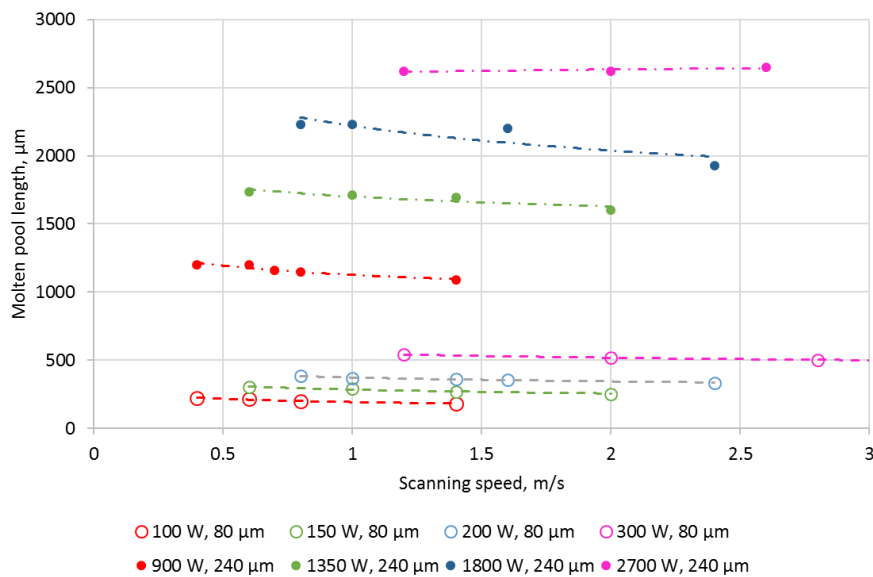


Figure 74. Length of the molten pool *versus* scanning speed.

For laser melting, laser power and spot size played the decisive role in the molten pool size. Higher laser power resulted in very long molten pool and even high penetration depths did not stabilise the melted track. An increase in the volume of molten pool provoked flows and thereafter instability of the molten pool and irregularities in solidified tracks.

4.3 Hardness *versus* parameters

Hardness is a commonly investigated property for almost all parts manufactured by SLM. Often the hardness of laser-processed parts is comparable or superior to those produced by conventional methods, mainly as a result of the high cooling rates which lead to refinement of the microstructure. In this study, the hardness of the solidified melt pool was measured using a Vickers microhardness tester. The indentations were applied on the polished surface of the melt pool and the substrate material, for the “*powder*” case samples. Hardness measurements were taken at least twice inside the melt pool and twice on the substrate material, as shown in Figure 75. The total number of indentations inside the melt pool was dependent on the size of the solidified remolten zone.

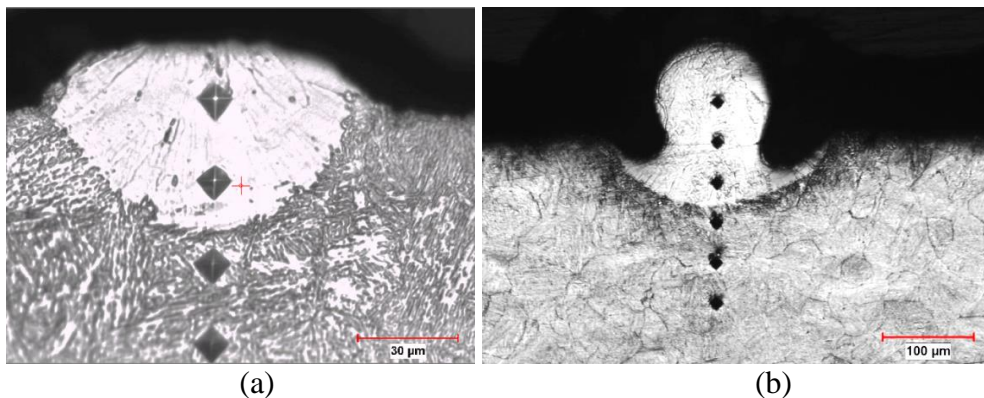


Figure 75: Hardness measurements taken on a cross-section of a single track manufactured using the 80 µm spot size. $P=100\text{ W}$, $V=0.5\text{ m/s}$, $P_d=19.9\text{ kW/mm}^2$ (a) and 240 µm spot size, $P=900\text{ W}$, $V=0.9\text{ m/s}$, $P_d=19.9\text{ kW/mm}^2$ (b).

Table 12 presents the hardness measurements obtained on the cross-sections of single tracks that were manufactured on the low- and high-power systems. It is well established that the chemical composition of the material, the processing environment (i.e. atmosphere) and the cooling rate are the main factors affecting the hardness of SLM parts. In this study, the powder material and the processing environment were the same for all the parametric conditions. Therefore, the variation in hardness is believed to be due to the differences in the cooling rates, which are primarily dependent on the processing parameters.

Table 12: Hardness measurement for different parametric conditions.

	80 μm spot size											
Power density, kW/mm ²	19.9			29.8			39.8			59.7		
Scanning speed, m/s	0.4	0.5	0.6	0.6	0.8	1.0	0.8	1.0	1.2	1.2	1.4	1.6
Hardness measurements, Vickers	386	378	364	400	393	400	378	351	364	338	378	371
	375	371	371	385	400	385	344	357	351	378	385	378
	240 μm spot size											
	396	370	413	407	391	407	386	402	402	370	413	-
	407	413	402	407	375	391	375	396	380	375	391	-
	413	402	-	402	396	-	365	-	-	-	402	-

The microhardness measurements were found to be similar for the various process conditions examined. Regardless of the parametric conditions (i.e. spot size, scanning speed and power density), no significant trend in microhardness for the tested samples could be identified. This is an indication that the difference in cooling rates, caused by the change in processing parameters, had little effect on the microhardness of the remolten zone. It was also noted that the hardness measurements were comparable and in some instances slightly higher than the hardness specification for traditional 17-4PH in the solution annealed condition A (i.e. 345–372 HV). The slight increase in hardness is possibly due to the rapid cooling rates that result in the refinement of the microstructure. It is desired that the mechanical properties of SLM parts, such as hardness, are comparable to or better than those produced by conventional methods. The hardness of the melt pool was found to be comparable to the hardness of the substrate material: there is no significant variation between the hardness of the melt pool and that of the substrate material.

4.4 Summary

The purpose of this study was to investigate the aspects of upscaling the SLM process parameters on the characteristics of single tracks formed. To achieve this, two SLM systems, operating at different spot sizes (i.e. 80 and 240 μm), were utilised. With regard to characterisation of the single tracks, the results obtained show that it is possible to form continuous tracks using either 80 μm or 240 μm spot sizes. However, the maximum optimal scanning speed for single track formation is reduced for the bigger spot size. At 80 μm spot size, the maximum optimal scanning speed is 1.2 m/s whereas at 240 μm the maximum optimal scanning speed is 0.5 m/s. This clearly shows that although it is possible to improve the SLM

process efficiency by using a bigger spot size, a compromise is made on the maximum optimal scanning speed. Nevertheless, using a bigger spot size can be positive for the efficiency of the SLM process, since this will also help to increase the hatch spacing. It is well-known that the larger hatch spacing will help to reduce the time it takes to scan each layer, thus positively impacting the process efficiency.

It was also shown that the width of the track and penetration depth decreases as the scanning speed increases, and increases with the laser power density. In SLM, the wider track width can help to increase the hatch spacing, which in turn will also reduce the time it takes to produce each layer. The penetration depth, on the other hand, can influence the process efficiency *via* the layer thickness: an increase in penetration depth can allow for an increase in the layer thickness, which will also improve the build rate. The penetration depths achieved with the bigger spot are mostly greater than the layer thickness (i.e. $>75 \mu\text{m}$) applied in this study. With regard to the hardness measurements, no significant trend in microhardness for the tested samples can be identified, that is regardless of the parametric conditions (i.e. spot size, scanning speed and power density), the hardness measurements appear to be similar. Nevertheless, the hardness of the melt pool was found to be comparable to the hardness of the substrate material, which was manufactured by rolling and heat-treating to condition A (i.e. solution annealing).

CHAPTER 5 –CONCLUSIONS AND FUTURE WORK

5.1 Conclusions

The following conclusions can be drawn from this study:

1. The formation of single tracks has a threshold character, that is, there are stability zones where the single tracks formed are continuous and without defects, and instability zones where the single tracks formed show either undercuts or humping, especially at higher scanning speeds and laser powers.
2. The use of a larger spot size is possible at the expense of the maximum optimal scanning speed, that is, the optimal scanning speed range is wider for a smaller spot size (i.e. 0.4-1.2 m/s), and narrows down for a larger spot size (i.e. 0.4-0.5 m/s).
3. In terms of stability zones, the results obtained with and without powder concur, that is, the optimal range for continuous tracks formed without undercuts or humping is almost the same in both cases.
4. Increasing the laser power density more than 19.9 kW/mm^2 accelerates the onset of defects.
5. The use of a higher laser power and larger spot size results in wider and deeper melt pools, which could be positive for the process efficiency, but numerical simulation showed that higher laser power resulted in longer molten pool that provoked instabilities. Excessive energy input leads to suppression of molten pool and spatter formation.
6. The effect of laser power density and scanning speed on the size of the solidified track is contradictory. Higher scanning speeds reduce the width and remolten depth, whereas increasing the power density increases the width and remolten depth.
7. There is no significant difference in the microhardness of the solidified track for the various parametric conditions investigated.
8. The microhardness of the solidified tracks was comparable to the hardness of the substrate material used.

5.2 Recommendations for future work

The experimental part of this study showed that it is possible to upscale SLM process parameters. However, further studies should be done in order to get more accurate understanding of the building process by:

1. Examining the surface morphology of each layer manufactured using the optimal parameters established in this study. Here the effect of changing the hatch spacing and layer thickness on the roughness should also be evaluated.
2. Investigating the effect of these two spot sizes (i.e. 80 and 240 μm) on the actual build rate. It was shown that the optimal scanning speed is higher when using the smaller spot size and narrows down for the larger spot size. Therefore, it is important to establish whether using the larger spot size has any significant effect on the actual build rate of the part.
3. Further modelling the process in order to obtain a better understanding of the phenomena that lead to the formation of defects.
4. Investigating the microstructure and mechanical properties of 3D parts. Although single track experiments provide us with a fundamental understanding of the building process, the hardness measurements obtained cannot be used to estimate the final properties of the part. This is because constant re-melting occurs during manufacturing of 3D parts which can affect the final microstructure and mechanical properties of the part build.

REFERENCES

- Aboulkhair, N.T., Everitt, N.M., Ashcroft, I. and Tuck, C., 2014. Reducing porosity in AlSi10Mg parts processed by selective laser melting. *Additive Manufacturing*, 1, pp.77-86.
- Abrahams, R.A., 2010. The Development of High Strength Corrosion Resistant Precipitation Hardening Cast Steels. Doctoral dissertation, The Pennsylvania State University. https://etda.libraries.psu.edu/files/final_submissions/5061
- Antony, K. and Arivazhagan, N., 2015. Studies on energy penetration and Marangoni effect during laser melting process. *Journal of Engineering Science and Technology*, 10(4), pp.509-525.
- Antony, K., Arivazhagan, N. and Senthilkumaran, K., 2014. Studies on wettability of stainless steel 316L powder in laser melting process. *Journal of Engineering Science and Technology*, 9(5), pp.533-540.
- Antony, K.C., 1963. Aging reactions in precipitation hardenable stainless steel. *Journal of Metals*, 15, pp.922-927.
- ASTM Committee A01 on Steel, 2004. "ASTM A564/A564M Standard Specification for Hot-Rolled and Cold-Finished Age-Hardening Stainless Steel Bars and Shapes", *ASTM International*.
- ASTM Committee A01 on Steel, 2004. "ASTM A747 - Standard Specification for Steel Castings, Stainless, Precipitation Hardening", *ASTM International*.
- ASTM E 385-11e1 Standard practice for Knoop and Vickers hardness of materials. *Annual book of ASTM standards*.
- Averyanova, M., Cicala, E., Bertrand, P. and Grevey, D., 2012. Experimental design approach to optimize selective laser melting of martensitic 17-4 PH powder: part I-single laser tracks and first layer. *Rapid Prototyping Journal*, 18(1), pp.28-37.
- Badrossamay, M. and Childs, T.H.C., 2006. Layer formation studies in selective laser melting of steel powders. In *Proc. SFF Symposium*, Texas USA, (pp. 268-279).
- Barlow, L.D., 2010. The effect of austenitising and tempering parameters on the microstructure and hardness of martensitic stainless steel AISI 420, Doctoral dissertation, University of Pretoria. <https://repository.up.ac.za/handle/2263/29839>
- Beuselink, L., Govers, G., Poesen, J., Degraer, G. and Froyen, L., 1998. Grain-size analysis by laser diffractometry: comparison with the sieve-pipette method. *Catena*, 32(3), pp.193-208.
- Bremen, S., Meiners, W. and Diatlov, A., 2012. Selective laser melting. *Laser Technik Journal*, 9(2), pp.33-38.

- Buchbinder, D., Schleifenbaum, H., Heidrich, S., Meiners, W. and Bültmann, J., 2011. High power selective laser melting (HP SLM) of aluminum parts. *Physics Procedia*, 12, pp.271-278.
- Cacace, S., Demir, A.G. and Semeraro, Q., 2017. Densification mechanism for different types of stainless steel powders in Selective Laser Melting. *Procedia CIRP*, 62, pp.475-480.
- Chandrasekhar, S., 2013. *Hydrodynamic and hydromagnetic stability*. Courier Corporation.
- Cheruvathur, S., Lass, E.A. and Campbell, C.E., 2016. Additive manufacturing of 17-4 PH stainless steel: post-processing heat treatment to achieve uniform reproducible microstructure. *Journal of Metals*, 68(3), pp.930-942.
- Childs, T.H.C., Hauser, C. and Badrossamay, M., 2004. Mapping and modelling single scan track formation in direct metal selective laser melting. *CIRP Annals-Manufacturing Technology*, 53(1), pp.191-194.
- Christien, F., Le Gall, R. and Saindrenan, G., 2003. Phosphorus grain boundary segregation in steel 17-4PH. *Scripta Materialia*, 48(1), pp.11-16.
- Ciurana, J., Hernandez, L. and Delgado, J., 2013. Energy density analysis on single tracks formed by selective laser melting with CoCrMo powder material. *The International Journal of Advanced Manufacturing Technology*, 68(5-8), pp.1103-1110.
- Cory, J., 1997. "17-4PH Hardness vs. Chemistry", in *SFSA T&O Proceedings*.
- Cunat, P.J., 2004. Alloying elements in stainless steel and other chromium-containing alloys. *Euro Inox, 2004*, pp.1-24.
- Dahotre, N.B. and Harimkar, S., 2008. *Laser fabrication and machining of materials*, Springer Science & Business Media.
- Dai, D. and Gu, D., 2015. Tailoring surface quality through mass and momentum transfer modeling using a volume of fluid method in selective laser melting of TiC/AlSi10Mg powder. *International Journal of Machine Tools and Manufacture*, 88, pp.95-107.
- Das, S., 2003. Physical aspects of process control in selective laser sintering of metals. *Advanced Engineering Materials*, 5(10), pp.701-711.
- David, S.A. and Vitek, J.M., 1989. Correlation between solidification parameters and weld microstructures. *International Materials Reviews*, 34(1), pp.213-245.
- de Oliveira, M.P., Calderón-Hernández, J.W., Magnabosco, R., Hincapie-Ladino, D. and Alonso-Falleiros, N., 2017. Effect of Niobium on Phase Transformations, Mechanical Properties and Corrosion of Supermartensitic Stainless Steel. *Journal of Materials Engineering and Performance*, 26(4), pp.1664-1672.
- Dieter, G.E. and Bacon, D.J., 1986. *Mechanical metallurgy*, 3, New York: McGraw-Hill.

Facchini, L., 2010. Microstructure and mechanical properties of biomedical alloys produced by Rapid Manufacturing techniques. Doctoral dissertation, University of Trento. http://eprints-phd.biblio.unitn.it/193/1/PhD_thesis_Luca_Facchini.pdf

Frostevarg, J. and Kaplan, A.F., 2014. Undercut suppression in laser-arc hybrid welding by melt pool tailoring. *Journal of Laser Applications*, 26(3), p.031501.

Gibson, I., Rosen, D. and Stucker, B., 2014. *Additive manufacturing technologies: 3D printing, rapid prototyping, and direct digital manufacturing*. Springer.

Gong, H., Gu, H., Zeng, K., Dilip, J., Pal, D., Stucker, B., Christiansen, D., Beuth, J. and Lewandowski, J.J., 2014. Melt pool characterization for selective laser melting of Ti-6Al-4V pre-alloyed powder. In *Solid Freeform Fabrication Symposium*, pp. 256-267.

Gratton, A., 2012. Comparison of mechanical, metallurgical properties of 17-4PH stainless steel between direct metal laser sintering (DMLS) and traditional manufacturing methods. *2012 NCUR proceedings*.

Gu, H., Gong, H., Pal, D., Rafi, K., Starr, T. and Stucker, B., 2013. Influences of energy density on porosity and microstructure of selective laser melted 17-4PH stainless steel. In *2013 Solid Freeform Fabrication Symposium*, pp. 474.

Guo, Z., Sha, W. and Vaumousse, D., 2003. Microstructural evolution in a PH13-8 stainless steel after ageing. *Acta Materialia*, 51(1), pp.101-116.

Hebert, R.J., 2016. Metallurgical aspects of powder bed metal additive manufacturing. *Journal of Materials Science*, 51(3), pp.1165-1175.

Hsiao, C.N., Chiou, C.S. and Yang, J.R., 2002. Aging reactions in a 17-4 PH stainless steel. *Materials Chemistry and Physics*, 74(2), pp.134-142.

Hu, Z., Zhu, H., Zhang, H. and Zeng, X., 2017. Experimental investigation on selective laser melting of 17-4PH stainless steel. *Optics & Laser Technology*, 87, pp.17-25.

Jerrard, P.G.E., 2011. Selective laser melting of advanced metal alloys for aerospace applications. Doctoral dissertation, University of Exeter. <https://ore.exeter.ac.uk/repository/handle/10036/3576>

Karalekas, D. and Rapti, D., 2002. Investigation of the processing dependence of SL solidification residual stresses. *Rapid Prototyping Journal*, 8(4), pp.243-247.

Kelbassa, I., Gasser, A., Meiners, W., Backes, G., Müller, B., 2012. High speed LAM. In *proceedings of the 37th International MATADOR*, University of Manchester.

Kempen, K., Thijs, L., Yasa, E., Badrossamay, M., Verheecke, W. and Kruth, J.P., 2011. Process optimization and microstructural analysis for selective laser melting of AlSi10Mg. In *Solid Freeform Fabrication Symposium*, 22, pp. 484-495.

Kempen, K., Vrancken, B., Buls, S., Thijs, L., Van Humbeeck, J. and Kruth, J.P., 2014. Selective laser melting of crack-free high density M2 high speed steel parts by baseplate preheating. *Journal of Manufacturing Science and Engineering*, 136(6), p.061026.

Khairallah, S.A., Anderson, A.T., Rubenchik, A. and King, W.E., 2016. Laser powder-bed fusion additive manufacturing: Physics of complex melt flow and formation mechanisms of pores, spatter, and denudation zones. *Acta Materialia*, 108, pp.36-45.

Koo, B.S., 2013. Simulation of Melt Penetration and Fluid Flow Behavior during Laser Welding. Doctoral dissertation, Lehigh University.

<https://preserve.lehigh.edu/cgi/viewcontent.cgi?article=2319&context=etd>

Kopf, R., Schlesinger, L., Peters, S. and Lanza, G., 2016. Adjusting the Factory Planning Process when Using Immature Technologies. *Procedia CIRP*, 41, pp.1011-1016.

Kou, S., 1987. *Welding metallurgy*. New York: John Wiley & Sons.

Kruth, J.P., Wang, X., Laoui, T. and Froyen, L., 2003. Lasers and materials in selective laser sintering. *Assembly Automation*, 23(4), pp.357-371.

Kurzynowski, T., Chlebus, E., Kuźnicka, B. and Reiner, J., 2012. Parameters in selective laser melting for processing metallic powders. In *SPIE LASE*, pp. 823914-823914.

Kusuma, C., Ahmed, S.H., Mian, A. and Srinivasan, R., 2017. Effect of Laser Power and Scan Speed on Melt Pool Characteristics of Commercially Pure Titanium. *Journal of Materials Engineering and Performance*, 26(7), pp.3560-3568.

Lee, H., Lim, C.H.J., Low, M.J., Tham, N., Murukeshan, V.M. and Kim, Y.J., 2017. Lasers in additive manufacturing: A review. *International Journal of Precision Engineering and Manufacturing-Green Technology*, 4(3), pp.307-322.

Li, R., Liu, J., Shi, Y., Wang, L. and Jiang, W., 2012. Balling behavior of stainless steel and nickel powder during selective laser melting process. *The International Journal of Advanced Manufacturing Technology*, 59(9-12), pp.1025-1035.

Liu, Y., Yang, Y. and Wang, D., 2016. A study on the residual stress during selective laser melting of metallic powder. *The International Journal of Advanced Manufacturing Technology*, 87(1-4), pp.647-656.

Mahmoudi, M., Elwany, A., Yadollahi, A., Thompson, S.M., Bian, L. and Shamsaei, N., 2017. Mechanical properties and microstructural characterization of selective laser melted 17-4 PH stainless steel. *Rapid Prototyping Journal*, 23(2), pp.280-294.

Mani, M., Feng, S., Lane, B., Donmez, A., Moylan, S. and Fesperman, R., 2015. *Measurement science needs for real-time control of additive manufacturing powder bed fusion processes*. US Department of Commerce, National Institute of Standards and Technology.

Marandel, J., Michel, H. and Gantois, M., 1975. Coherent precipitation and age hardening mechanisms in ferritic and martensitic alloys. *Metallurgical Transactions A*, 6(3), pp.449.

- Matilainen, V., Piili, H., Salminen, A., Syvänen, T. and Nyrhilä, O., 2014. Characterization of process efficiency improvement in laser additive manufacturing. *Physics Procedia*, 56, pp.317-326.
- Matilainen, V.P., Piili, H., Salminen, A. and Nyrhilä, O., 2015. Preliminary investigation of keyhole phenomena during single layer fabrication in laser additive manufacturing of stainless steel. *Physics Procedia*, 78, pp.377-387.
- Mazumder, J., 1993. *Fundamentals of Laser Welding: ASM metals handbook*, 6, ASM International.
- Mercelis, P. and Kruth, J.P., 2006. Residual stresses in selective laser sintering and selective laser melting. *Rapid Prototyping Journal*, 12(5), pp.254-265.
- Miyamoto, I., Park, S.J. and Ooie, T., 2003. Precision microwelding of thin metal foil with single-mode fibre laser. In *Proceedings of SPIE*, 5063, pp. 297-302.
- Miyamoto, I., Park, S.J. and Ooie, T., 2004. High speed micro welding by single-mode fibre laser. In *Proceedings of the 4th LANE*, pp. 55-66.
- Mower, T.M. and Long, M.J., 2016. Mechanical behavior of additive manufactured, powder-bed laser-fused materials. *Materials Science and Engineering: A*, 651, pp.198-213.
- Murr, L.E., Martinez, E., Hernandez, J., Collins, S., Amato, K.N., Gaytan, S.M. and Shindo, P.W., 2012. Microstructures and properties of 17-4 PH stainless steel fabricated by selective laser melting. *Journal of Materials Research and Technology*, 1(3), pp.167-177.
- Nakagawa, H. and Miyazaki, T., 1999. Effect of retained austenite on the microstructure and mechanical properties of martensitic precipitation hardening stainless steel. *Journal of materials science*, 34(16), pp.3901-3908.
- Nishiyama, Z., 1978. *Martensitic Transformation*, 1, New York: Academic Press.
- Niu, H.J. and Chang, I.T.H., 1999. Instability of scan tracks of selective laser sintering of high speed steel powder. *Scripta Materialia*, 41(11), pp.1229-1234.
- Okamoto, M., 1962. The Role of Si in 17-4 PH Type Stainless Steel. *Transactions of the Japan Institute of Metals*, 3(2), pp.51-56.
- Okunkova, A., Volosova, M., Peretyagin, P., Zhirnov, I., Podrabinnik, P., Fedorov, S.V. and Gusarov, A., 2016. Study of laser beam modulation influence on structure of materials produced by additive manufacturing. *Advanced. Material. Letters*, 7, pp.111-115.
- Pinkerton, A.J., 2016. Lasers in additive manufacturing. *Optics & Laser Technology*, 78, pp.25-32.
- Rack, H.J., 1981. *Physical and mechanical properties of cast 17-4 PH stainless steel*. Sandia National Labs, USA.

- Rafi, H.K., Pal, D., Patil, N., Starr, T.L. and Stucker, B.E., 2014. Microstructure and mechanical behavior of 17-4 precipitation hardenable steel processed by selective laser melting. *Journal of Materials Engineering and Performance*, 23(12), pp.4421-4428.
- Ready, J.F. and Farson, D.F. eds., 2001. *LIA handbook of laser materials processing*, pp. 223-262, Orlando: Laser Institute of America.
- Reichelt, R., 2007. Scanning electron microscopy. In *Science of microscopy*, pp. 133-272.
- Sabau, A.S. and Porter, W.D., 2008. Alloy shrinkage factors for the investment casting of 17-4PH stainless steel parts. *Metallurgical and Materials Transactions B*, 39(2), pp.317-330.
- Schleifenbaum, H., Diatlov, A., Hinke, C., Bültmann, J., Voswinckel, H., 2011. Direct photonic production: towards high speed additive manufacturing of individualized goods. *Production Engineering*, 5(4), pp. 359-371.
- Seifi, M., Salem, A., Beuth, J., Harrysson, O. and Lewandowski, J.J., 2016. Overview of materials qualification needs for metal additive manufacturing. *Journal of Metals*, 68(3), pp.747-764.
- Shamsaei, N., Yadollahi, A., Bian, L. and Thompson, S.M., 2015. An overview of Direct Laser Deposition for additive manufacturing Part II: Mechanical behavior, process parameter optimization and control. *Additive Manufacturing*, 8, pp.12-35.
- Shi, X., Ma, S., Liu, C., Chen, C., Wu, Q., Chen, X. and Lu, J., 2016. Performance of high layer thickness in selective laser melting of Ti6Al4V. *Journal of Materials*, 9(12), p.975.
- Shifeng, W., Shuai, L., Qingsong, W., Yan, C., Sheng, Z. and Yusheng, S., 2014. Effect of molten pool boundaries on the mechanical properties of selective laser melting parts. *Journal of Materials Processing Technology*, 214(11), pp.2660-2667.
- Smurov, I., Doubenskaia, M., Grigoriev, S. and Kotoban, D., 2014. Selective laser melting and direct metal deposition: from process fundamentals towards advanced products. In *Laser Optics*, pp. 1.
- Soderstrom, E. and Mendez, P., 2006. Humping mechanisms present in high speed welding. *Science and Technology of Welding and Joining*, 11(5), pp.572-579.
- Song, B., Zhao, X., Li, S., Han, C., Wei, Q., Wen, S., Liu, J. and Shi, Y., 2015. Differences in microstructure and properties between selective laser melting and traditional manufacturing for fabrication of metal parts: A review. *Frontiers of Mechanical Engineering*, 10(2), pp.111-125.
- Starr, T.L., Rafi, K., Stucker, B. and Scherzer, C.M., 2012. Controlling phase composition in selective laser melted stainless steels. *Power (W)*, 195, pp.195.
- Steen, W.M. and Mazumder, J., 2010. *Laser Material Processing*. London: Springer.
- Storti, F. and Balsamo, F., 2010. Particle size distributions by laser diffraction: sensitivity of granular matter strength to analytical operating procedures. *Solid Earth*, 1(1), pp.25.

Tavares, S.S.M., Pardal, J.M., Martins, T.R.B. and da Silva, M.R., 2017. Influence of Sulfur Content on the Corrosion Resistance of 17-4PH Stainless Steel. *Journal of Materials Engineering and Performance*, 26(6), pp.2512-2519.

Thomy, C., Seefeld, T. and Vollertsen, F., 2008. Humping effect in welding of steel with single-mode fibre laser. *Welding in the World*, 52(5-6), pp.9-18.

Vasudevan, M., Bhaduri, A.K., Raj, B. and Rao, K.P., 2003. Delta ferrite prediction in stainless steel welds using neural network analysis and comparison with other prediction methods. *Journal of Materials Processing Technology*, 142(1), pp.20-28.

Vrancken, B., Cain, V., Knutsen, R. and Van Humbeeck, J., 2014. Residual stress via the contour method in compact tension specimens produced via selective laser melting. *Scripta Materialia*, 87, pp.29-32.

Wang, J., Zou, H., Li, C., Qiu, S.Y. and Shen, B.L., 2006. The effect of microstructural evolution on hardening behavior of type 17-4PH stainless steel in long-term aging at 350 °C. *Materials Characterization*, 57(4), pp.274-280.

Wanjara, P. and Jahazi, M., 2008. Characterization of electron beam welded 17-4 PH stainless steel. *Canadian Metallurgical Quarterly*, 47(4), pp.413-435.

Yadollahi, A., Shamsaei, N., Thompson, S.M., Elwany, A. and Bian, L., 2015. Mechanical and microstructural properties of selective laser melted 17-4 PH stainless steel. In *ASME International Mechanical Engineering Congress and Exposition*, pp. V02AT02A014-V02AT02A014).

Yadroitsau, I., 2009. *Selective laser melting: Direct manufacturing of 3D-objects by selective laser melting of metal powders*. Saarbrücken: LAP Lambert Academic Publishing.

Yadroitsava, I., Els, J., Booyesen, G. and Yadroitsev, I., 2015. Peculiarities of single track formation from Ti6AL4V alloy at different laser power densities by selective laser melting. *South African Journal of Industrial Engineering*, 26(3), pp.86-95.

Yadroitsev, I. and Smurov, I., 2010. Selective Laser Melting Technology: from the single laser melted track stability to 3D parts for complex shape, *Physics Procedia*, 5, pp 551-560.

Yadroitsev, I. and Smurov, I., 2011. Surface morphology in selective laser melting of metal powders. *Physics Procedia*, 12, pp.264-270.

Yadroitsev, I., Bertrand, P., Antonenkova, G., Grigoriev, S. and Smurov, I., 2013. Use of track/layer morphology to develop functional parts by selective laser melting. *Journal of Laser Applications*, 25(5), pp.052003.

Yadroitsev, I., Gusarov, A., Yadroitsava, I. and Smurov, I. 2010. Single track formation in selective laser melting of metal powders. *Journal of Materials Processing Technology*, 210(12), pp. 1624-1631.

Yadroitsev, I., Krakhmalev, P. & Yadroitsava, I., 2015. Hierarchical design principles of selective laser melting for high quality metallic objects. *Additive Manufacturing*, 7, pp. 45-56.

Yadroitsev, I., Krakhmalev, P., Yadroitsava, I., Johansson, S. & Smurov, I., 2013. Energy input effect on morphology and microstructure of selective laser melting single track from metallic powder. *Journal of Materials Processing Technology*, 213(4), pp. 606-613.

Yadroitsev, I., Yadroitsava, I., Bertrand, P. and Smurov, I., 2012. Factor analysis of selective laser melting process parameters and geometrical characteristics of synthesized single tracks. *Rapid Prototyping Journal*, 18(3), pp.201-208.

Yan, W., Ge, W., Qian, Y., Lin, S., Zhou, B., Liu, W.K., Lin, F. and Wagner, G.J., 2017. Multi-physics modeling of single/multiple-track defect mechanisms in electron beam selective melting. *Acta Materialia*, 134, pp.324-333.

Yoo, W.D., Lee, J.H., Youn, K.T. and Rhyim, Y.M., 2006. Study on the microstructure and mechanical properties of 17-4 PH stainless steel depending on heat treatment and aging time. In *Solid State Phenomena*, 118, pp. 15-20.

<https://www.engineering.com/3DPrinting/3DPrintingArticles/ArticleID/15202/7-Issues-to-Look-Out-for-in-Metal-3D-Printing.aspx>, Accessed on 09/09/2017

<https://www.aircraftmaterials.com/data/alstst/17-4tube.html>, Accessed on 09/09/2017.

<https://www.upmet.com/products/stainless-steel/17-4-ph#Chemical-Properties>, Accessed on 09/09/2017.

<http://www.shimadzu.com/an/powder/support/practice/p01/lesson22.html> , Accessed on 5/10/2017.

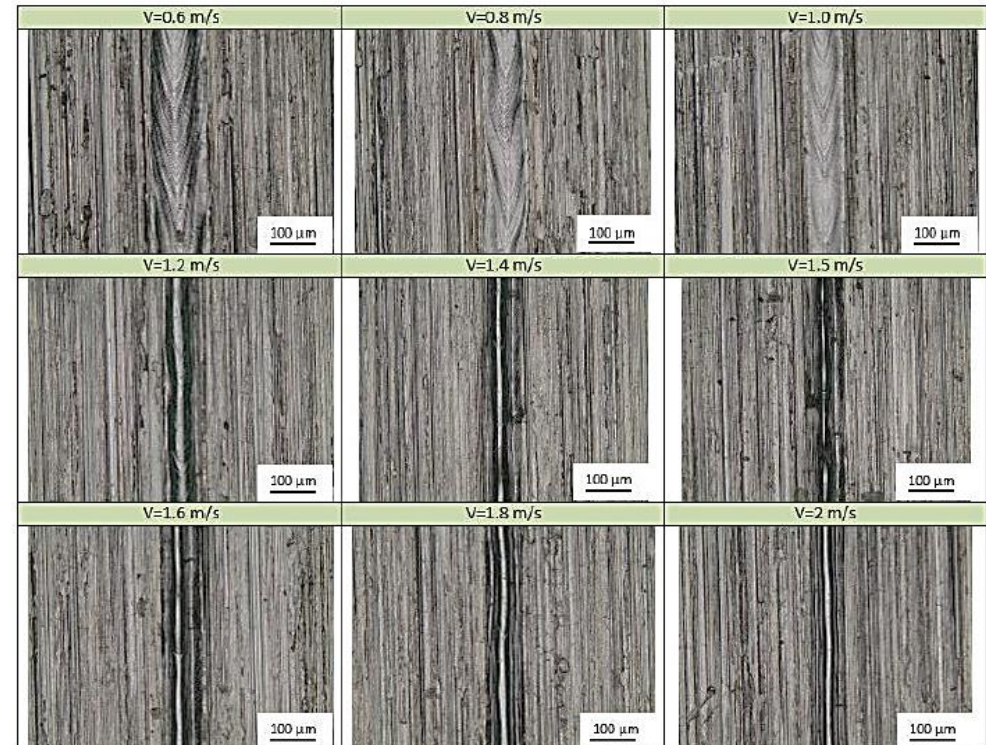
APPENDICES

Appendix I	Top views of the single tracks “ <i>No powder</i> ” case
Appendix II	Top views of the single tracks “ <i>Powder</i> ” case”
Appendix III	Cross-sections of single tracks “ <i>No powder case</i> ”
Appendix IV	Cross-sections of single tracks “ <i>Powder</i> ” case
Appendix V	Makoana, N.W., Moller, H., Burger, H., Tlotleng, M. and Yadroitsev, I., 2016. Evaluation of single tracks of 17-4PH steel manufactured at different power densities and scanning speeds by selective laser melting. <i>South African Journal of Industrial Engineering</i> , 27(3), pp.210-218. Paper also presented at the 17th Annual Conference of the Rapid Product Development Association of South Africa, held at Vaal University of Technology, 2-4 November 2016.
Appendix VI	Makoana, N.W., Moller, H., Louw, D. and Yadroitsev, I., 2017. Preliminary Investigation on Selective Laser Melting of 17-4PH Steel Using High Laser Powers of up to 1500W, in Proceedings <i>Frontiers in Optics 2017</i> , OSA Technical Digest (online) (Optical Society of America, 2017), paper JTu3A.43. Presented at OSA Frontiers in Optics + Laser Science Conference, Washington Hilton, Washington, District of Columbia, USA, 18-21 September 2017.

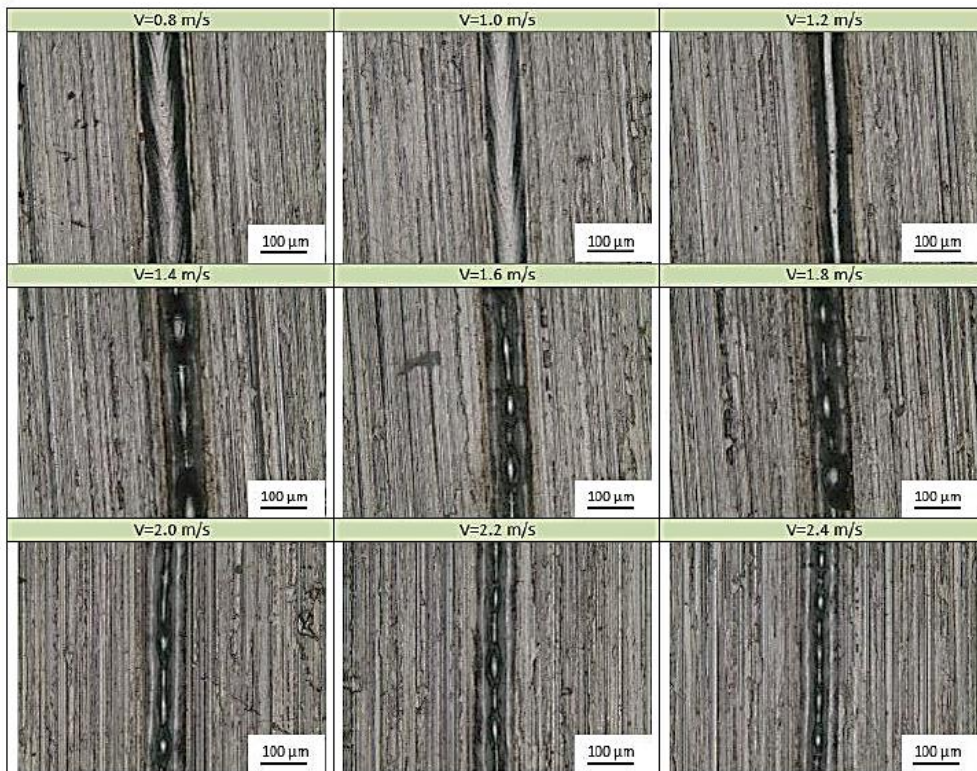
Appendix I: Top views of the single tracks “No powder” case

Laser power 100 W, scanning speed $V=0.4\text{-}1.4\text{ m/s}$, spot size $80\text{ }\mu\text{m}$, laser power density 19.9 kW/mm^2

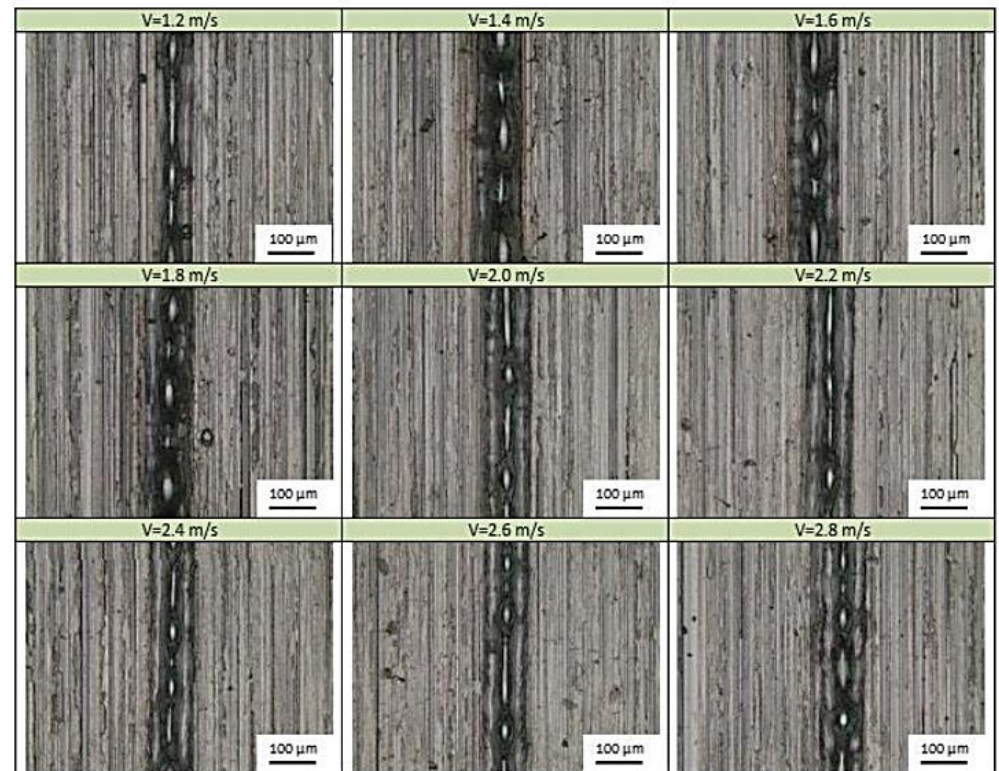
Laser power 150 W, scanning speed $V=0.6\text{-}2.0\text{ m/s}$, spot size $80\text{ }\mu\text{m}$, laser power density 29.8 kW/mm^2



Laser power 200 W, scanning speed $V=0.8-2.4$ m/s, spot size $80\ \mu\text{m}$, laser power density $39.8\ \text{kW}/\text{mm}^2$



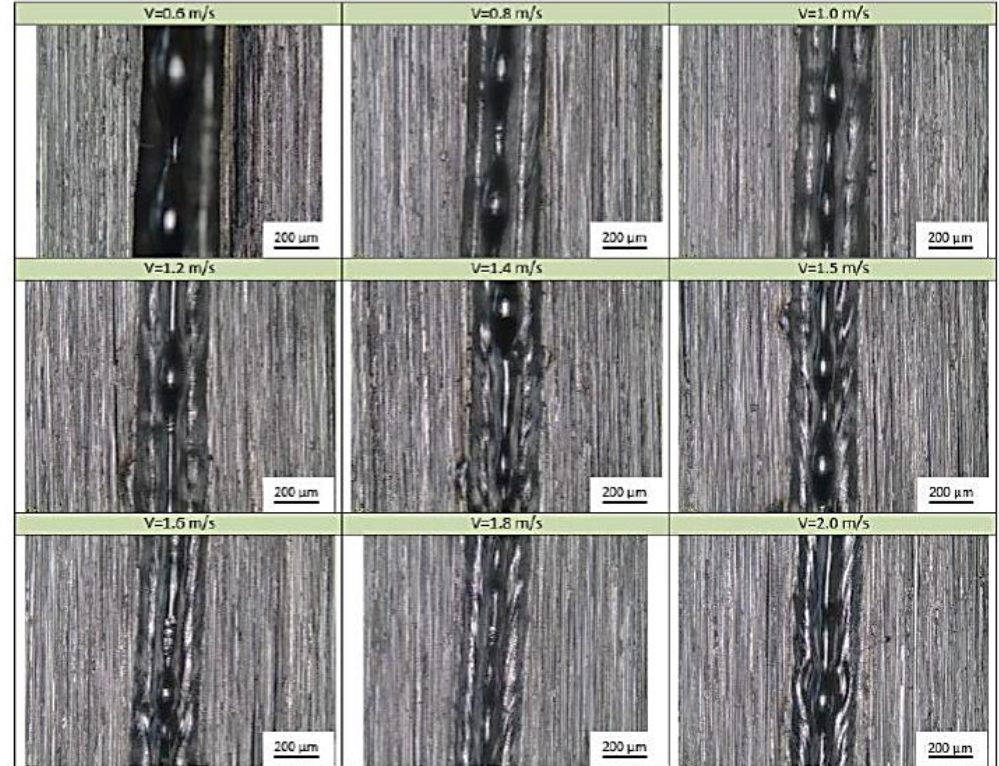
Laser power 300 W, scanning speed $V=1.2-2.8$ m/s, spot size $80\ \mu\text{m}$, laser power density $59.7\ \text{kW}/\text{mm}^2$



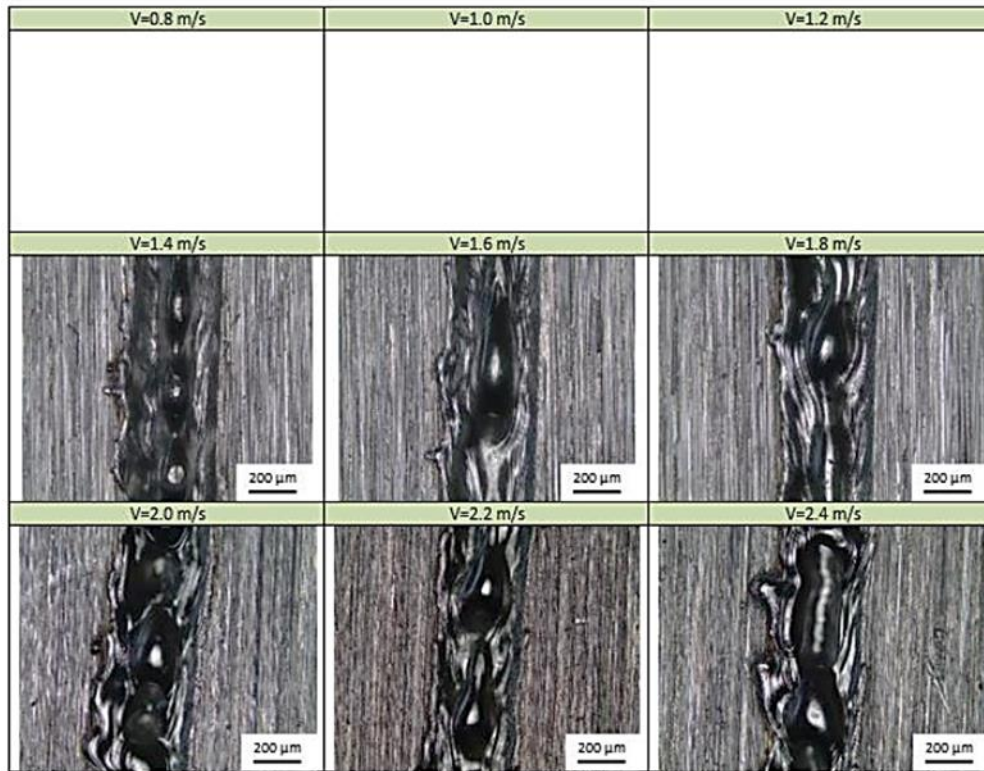
Laser power 900 W, scanning speed $V=0.4-1.4$ m/s, spot size $240\ \mu\text{m}$, laser power density $19.9\ \text{kW}/\text{mm}^2$



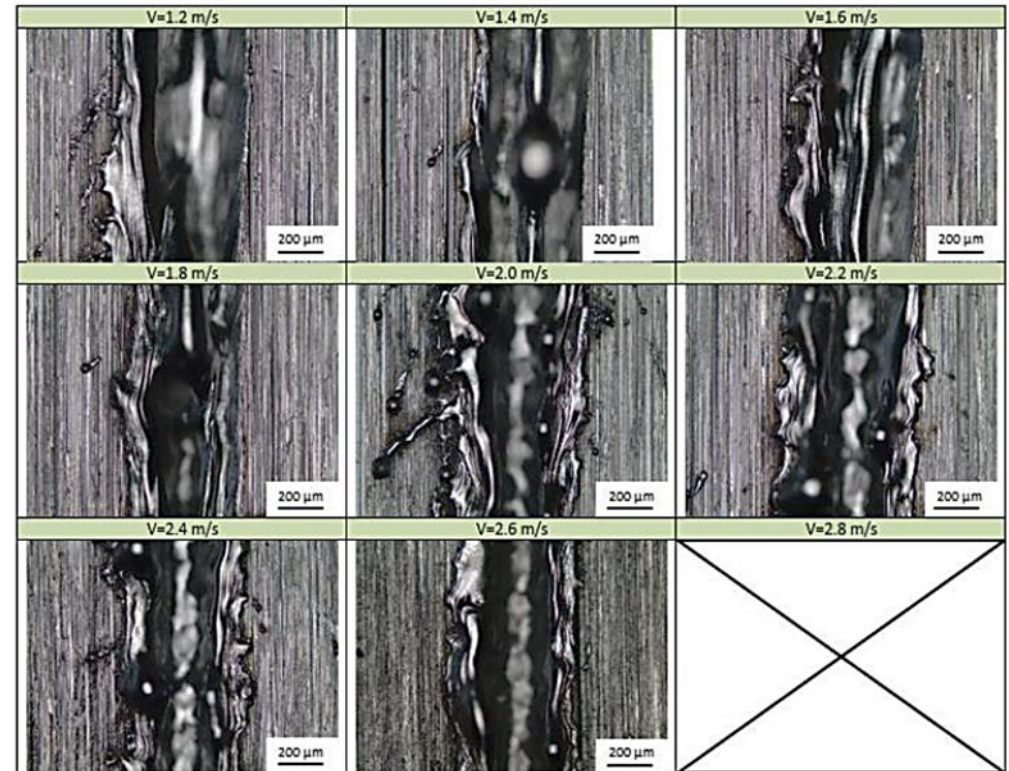
Laser power 1350 W, scanning speed $V=0.6-2.0$ m/s, spot size $240\ \mu\text{m}$, laser power density $29.8\ \text{kW}/\text{mm}^2$



Laser power 1800 W, scanning speed $V=0.8-2.4$ m/s, spot size $240\ \mu\text{m}$, laser power density $39.8\ \text{kW}/\text{mm}^2$



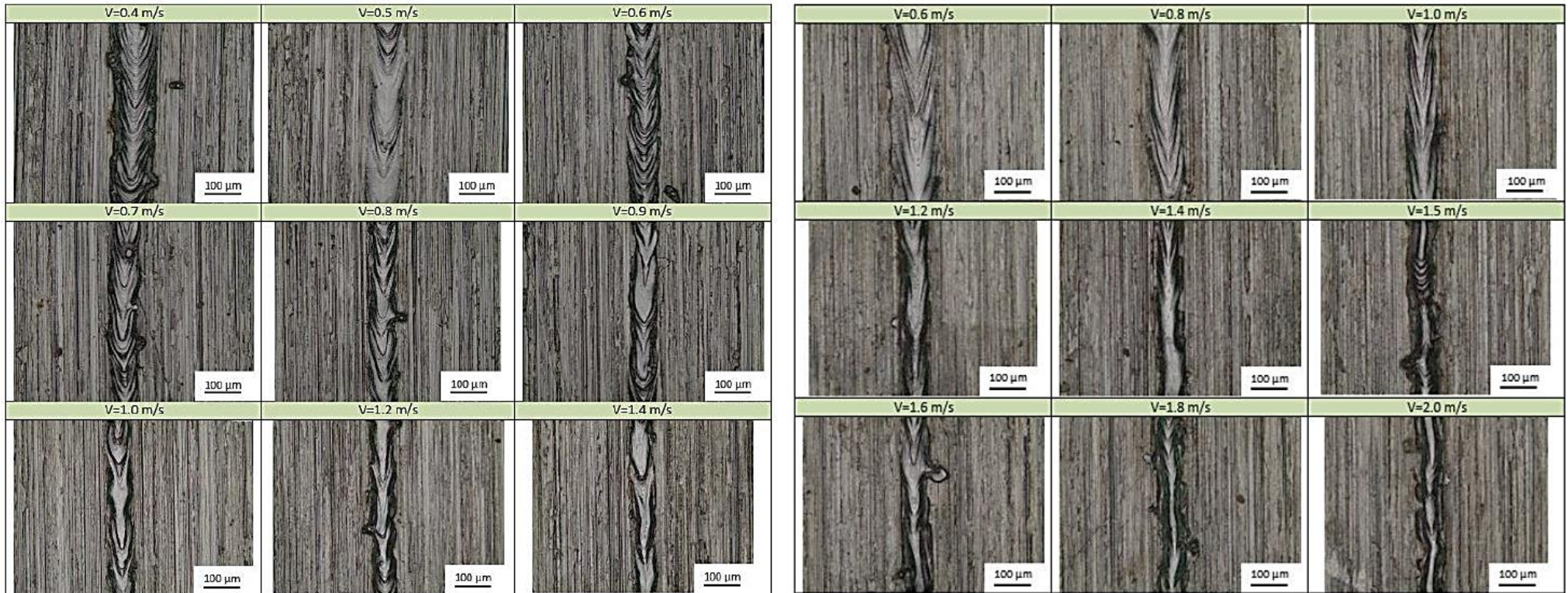
Laser power 2700 W, scanning speed $V=1.2-2.8$ m/s, spot size $240\ \mu\text{m}$, laser power density $59.7\ \text{kW}/\text{mm}^2$



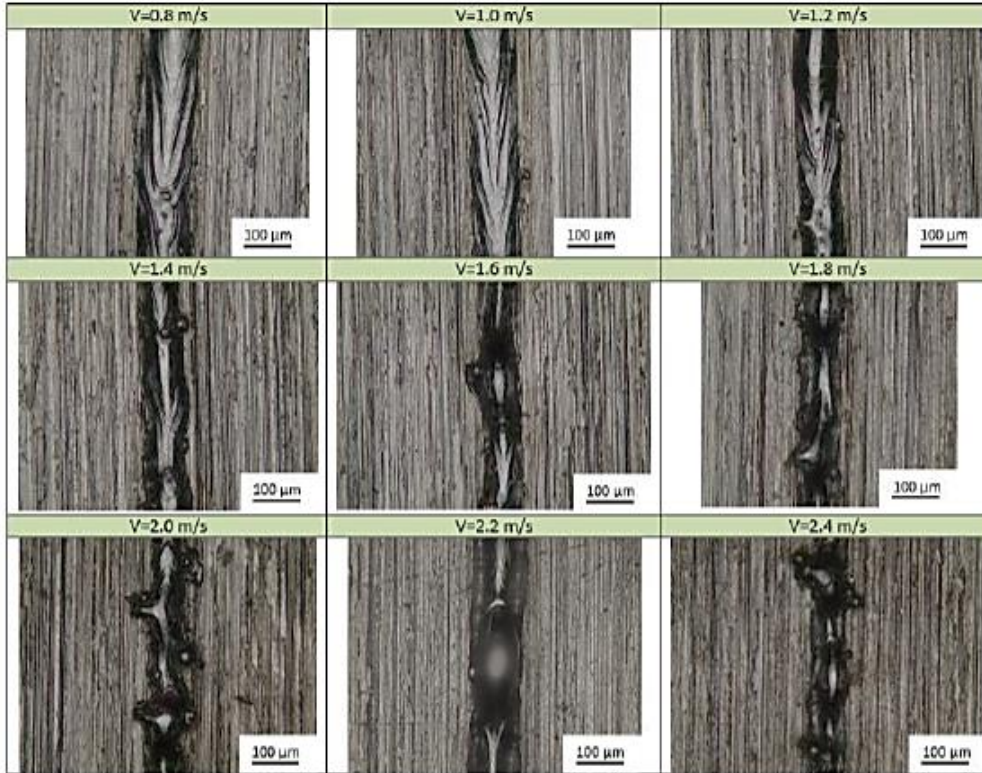
Appendix II: Top views of single tracks “Powder” case

Laser power 100 W, scanning speed $V=0.4-1.4$ m/s, spot size $80\ \mu\text{m}$, laser power density $19.9\ \text{kW}/\text{mm}^2$

Laser power 150 W, scanning speed $V=0.6-2.0$ m/s, spot size $80\ \mu\text{m}$, laser power density $29.8\ \text{kW}/\text{mm}^2$



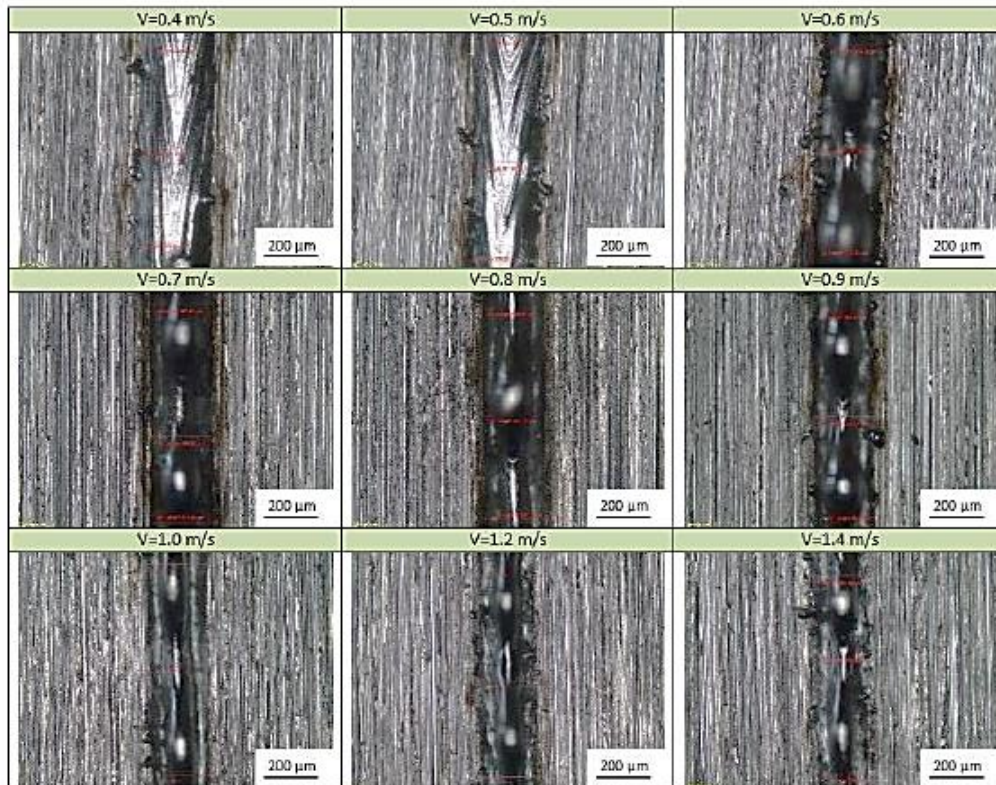
Laser power 200 W, scanning speed $V=0.8-2.4$ m/s, spot size $80\ \mu\text{m}$, laser power density $39.8\ \text{kW}/\text{mm}^2$



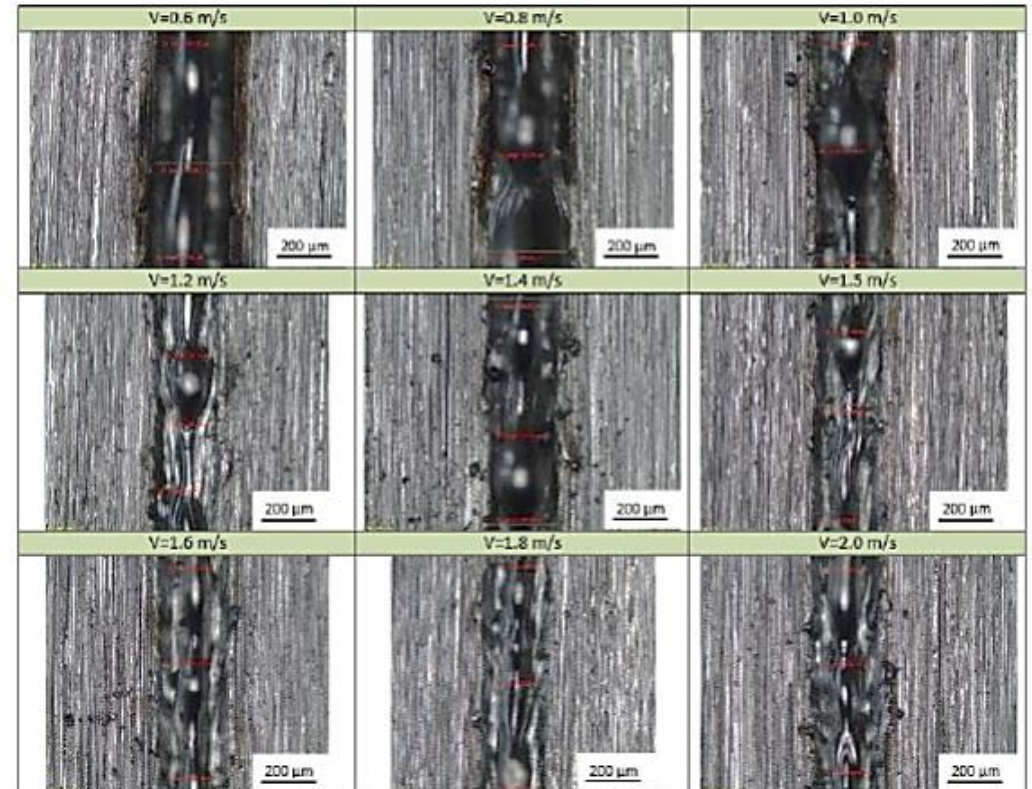
Laser power 300 W, scanning speed $V=1.2-2.8$ m/s, spot size $80\ \mu\text{m}$, laser power density $59.7\ \text{kW}/\text{mm}^2$



Laser power 900 W, scanning speed $V=0.4-1.4$ m/s, spot size 240 μm , laser power density 19.9 kW/mm^2

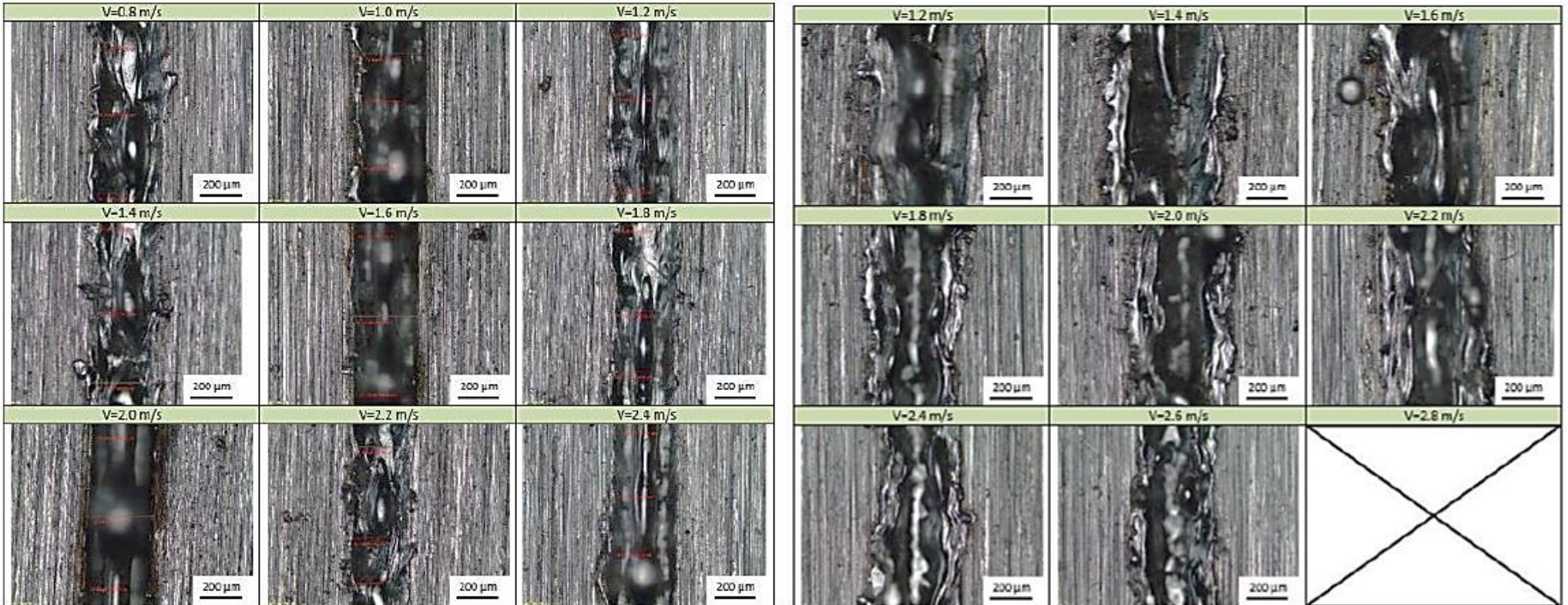


Laser power 1350 W, scanning speed $V=0.6-2.0$ m/s, spot size 240 μm , laser power density 29.8 kW/mm^2



Laser power 1800 W, scanning speed $V=0.8-2.4$ m/s, spot size 240 μm , laser power density 39.8 kW/mm^2

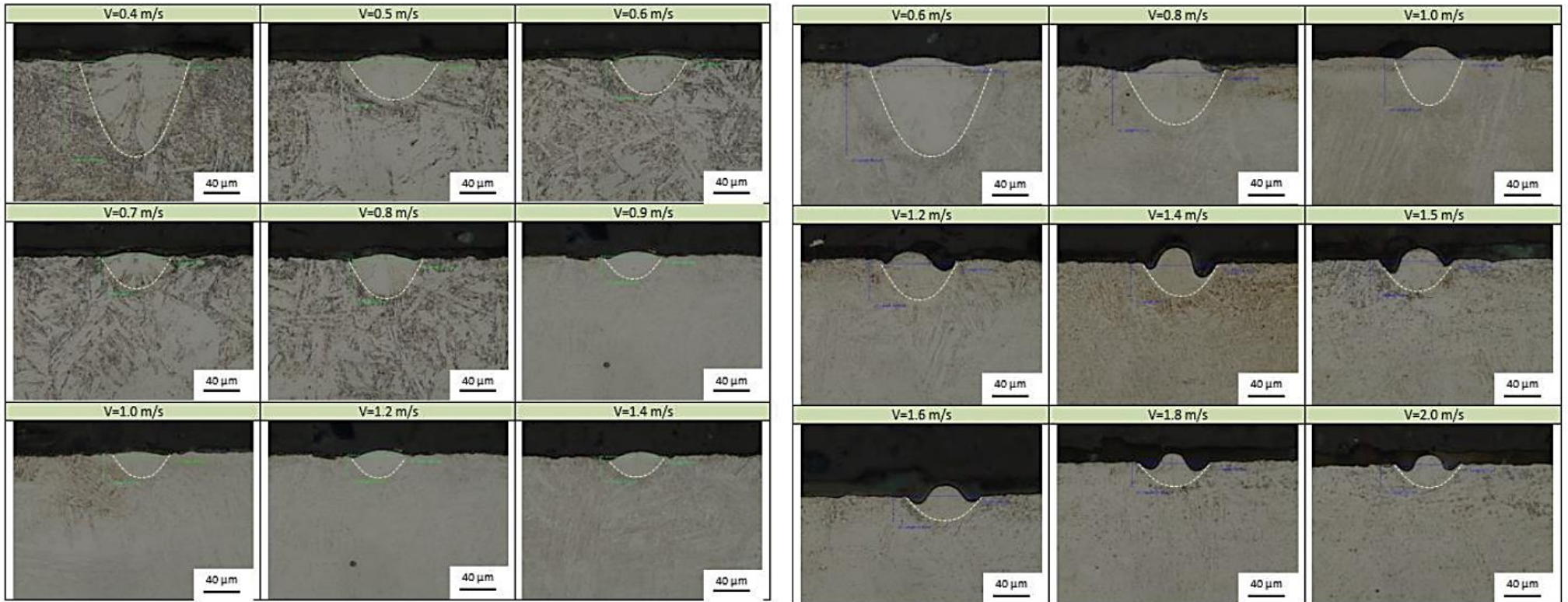
Laser power 2700 W, scanning speed $V=1.2-2.8$ m/s, spot size 240 μm , laser power density 59.7 kW/mm^2



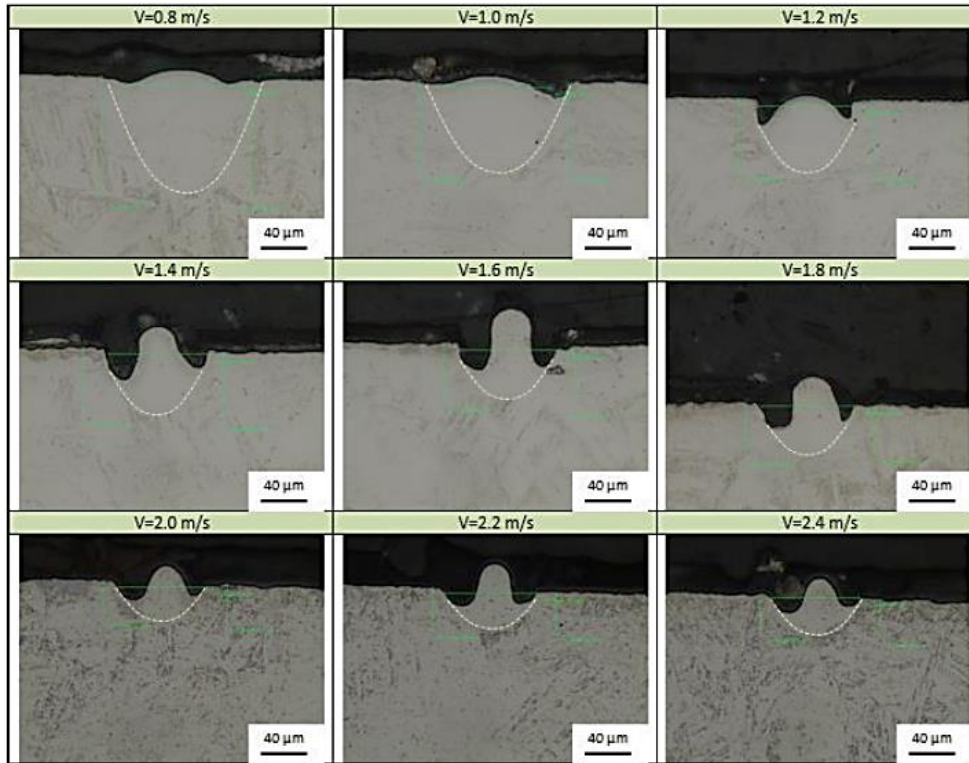
Appendix III: Cross-section views of single tracks “No Powder” case

Laser power 100 W, scanning speed $V=0.4-1.4$ m/s, spot size $80\ \mu\text{m}$, laser power density $19.9\ \text{kW}/\text{mm}^2$

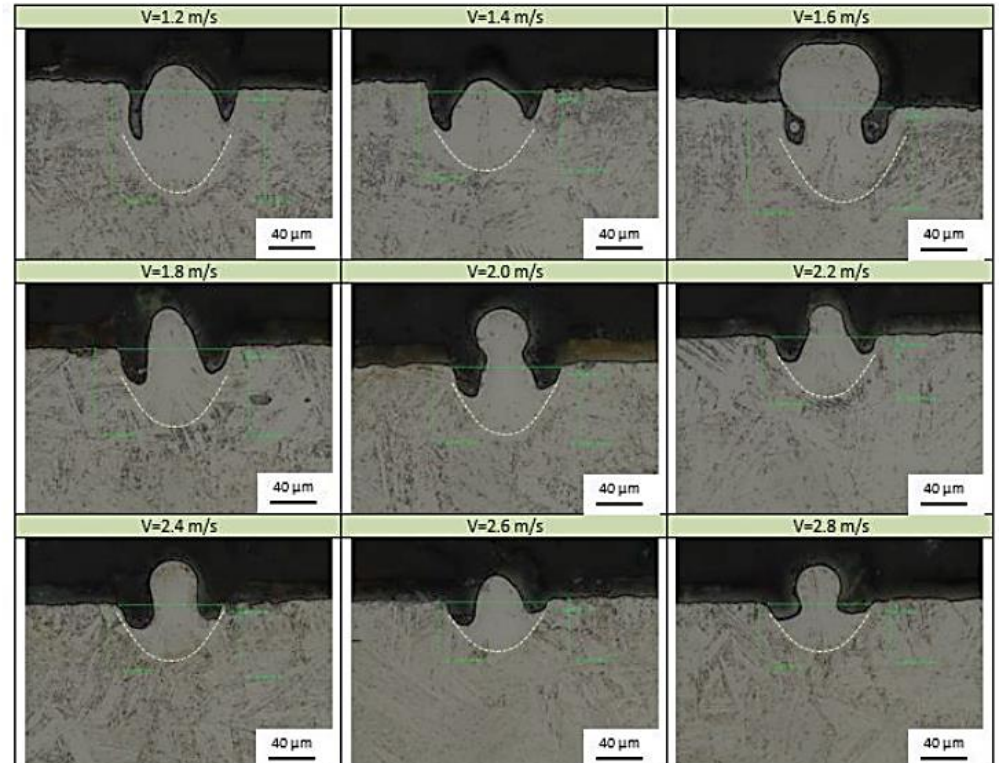
Laser power 150 W, scanning speed $V=0.6-2.0$ m/s, spot size $80\ \mu\text{m}$, laser power density $29.8\ \text{kW}/\text{mm}^2$



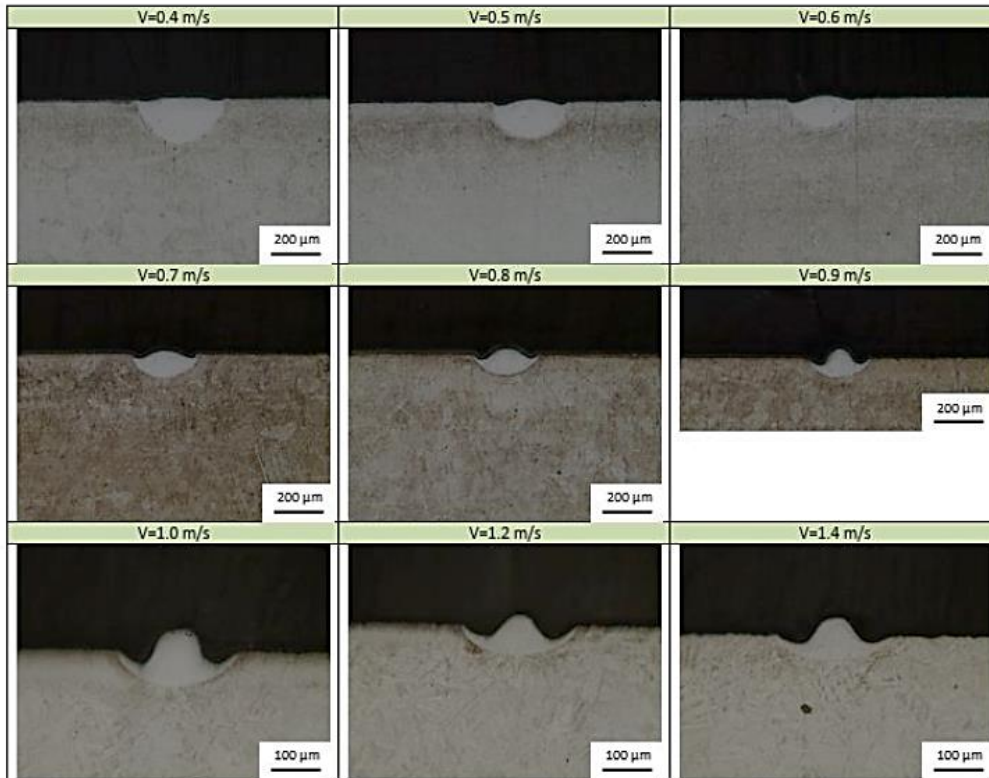
Laser power 200 W, scanning speed $V=0.8-2.4$ m/s, spot size $80\ \mu\text{m}$, laser power density $39.8\ \text{kW}/\text{mm}^2$



Laser power 300 W, scanning speed $V=1.2-2.8$ m/s, spot size $80\ \mu\text{m}$, laser power density $59.7\ \text{kW}/\text{mm}^2$



Laser power 900 W, scanning speed $V=0.4-1.4$ m/s, spot size $240\ \mu\text{m}$, laser power density $19.9\ \text{kW}/\text{mm}^2$

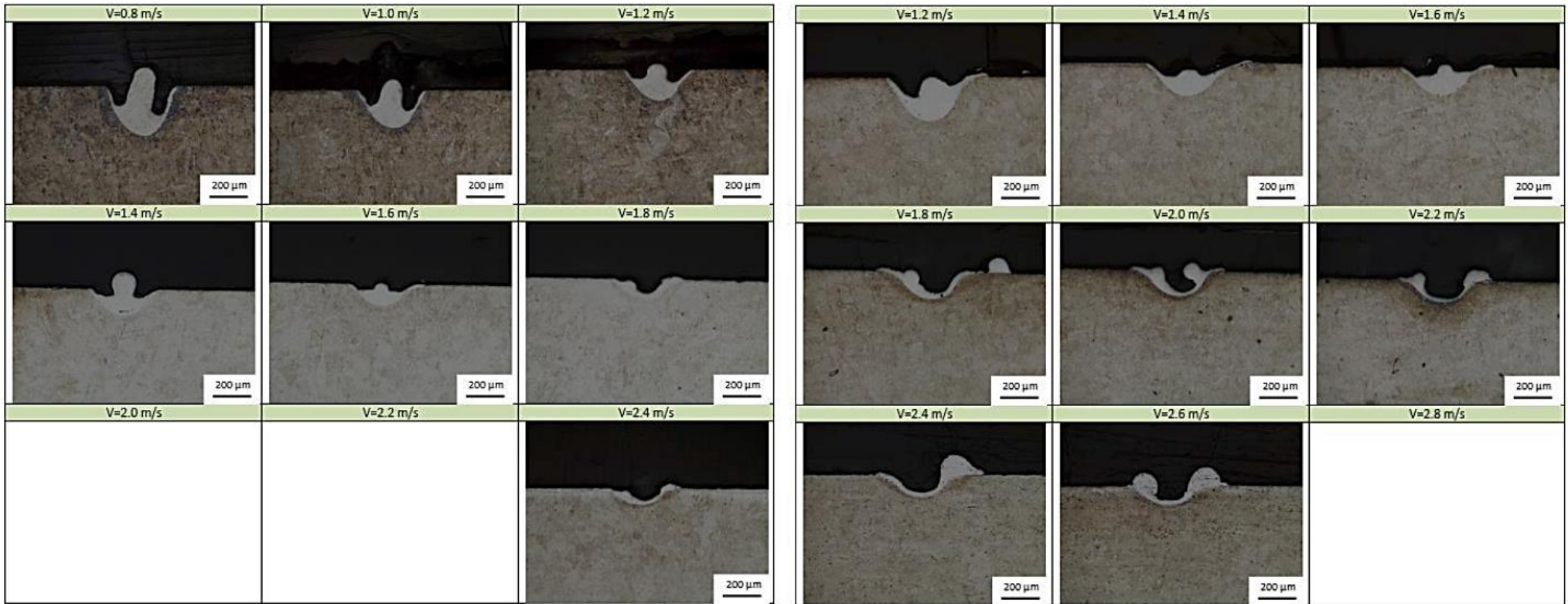


Laser power 1350 W, scanning speed $V=0.6-2.0$ m/s, spot size $240\ \mu\text{m}$, laser power density $29.8\ \text{kW}/\text{mm}^2$



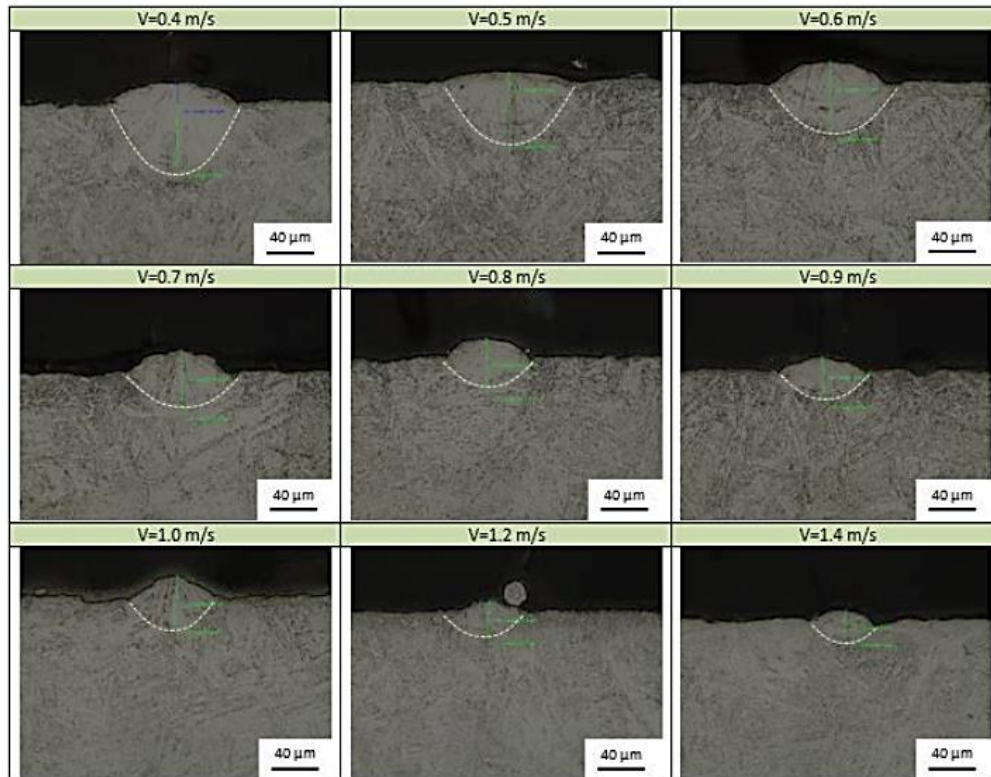
Laser power 1800 W, scanning speed $V=0.8-2.4$ m/s, spot size $240\ \mu\text{m}$, laser power density $39.8\ \text{kW}/\text{mm}^2$

Laser power 2700 W, scanning speed $V=1.2-2.8$ m/s, spot size $240\ \mu\text{m}$, laser power density $59.7\ \text{kW}/\text{mm}^2$

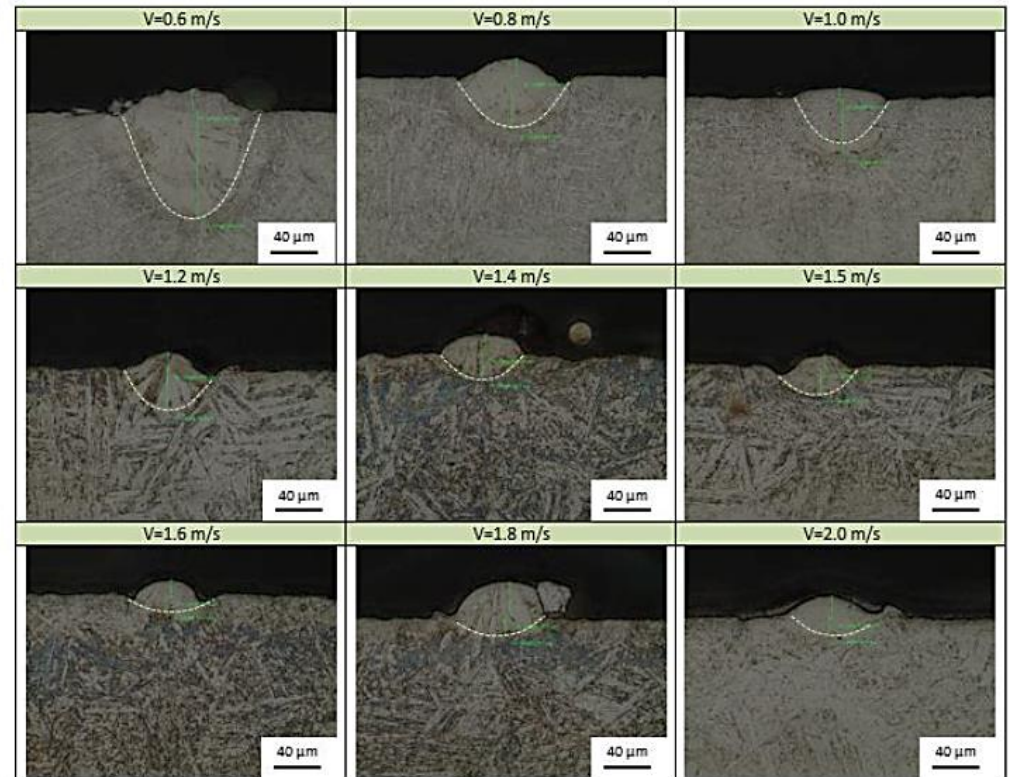


Appendix IV: Cross-section views of single tracks “Powder” case

Laser power 100 W, scanning speed $V=0.4-1.4$ m/s, spot size $80\ \mu\text{m}$, laser power density $19.9\ \text{kW}/\text{mm}^2$

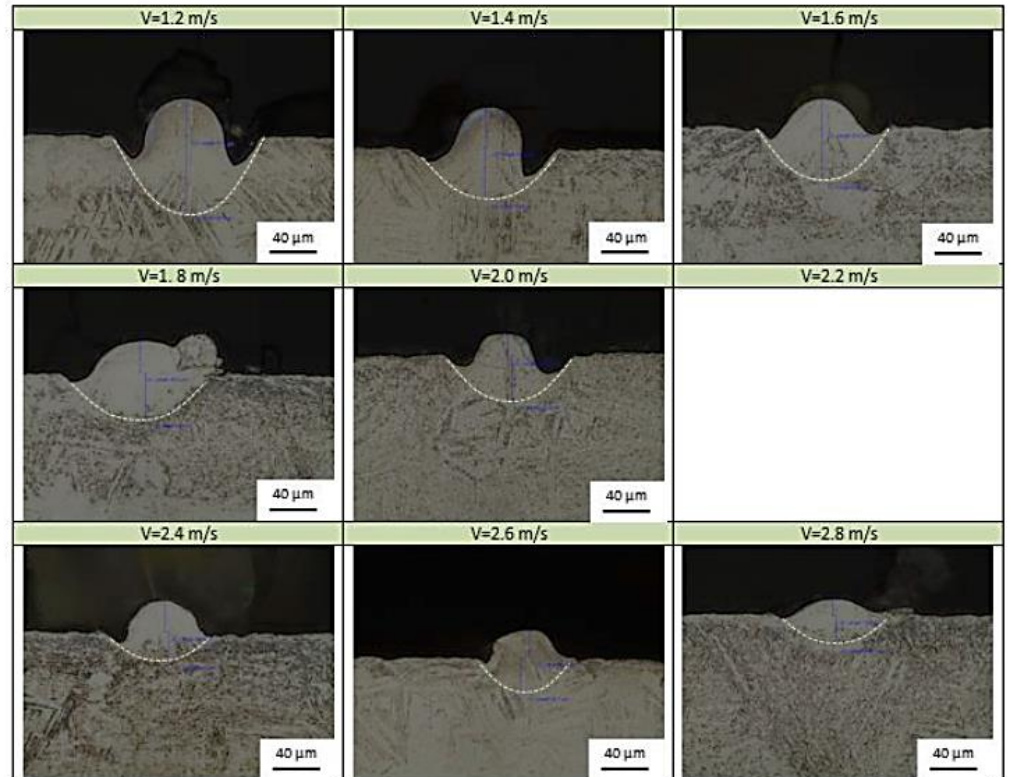
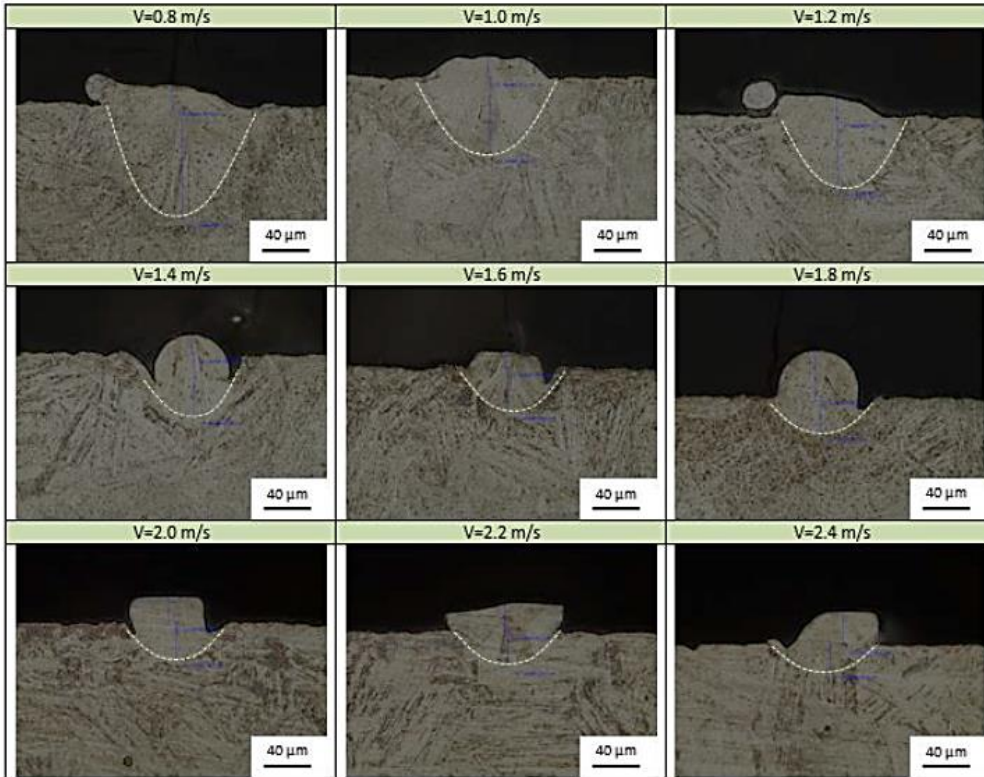


Laser power 150 W, scanning speed $V=0.6-2.0$ m/s, spot size $80\ \mu\text{m}$, laser power density $29.8\ \text{kW}/\text{mm}^2$

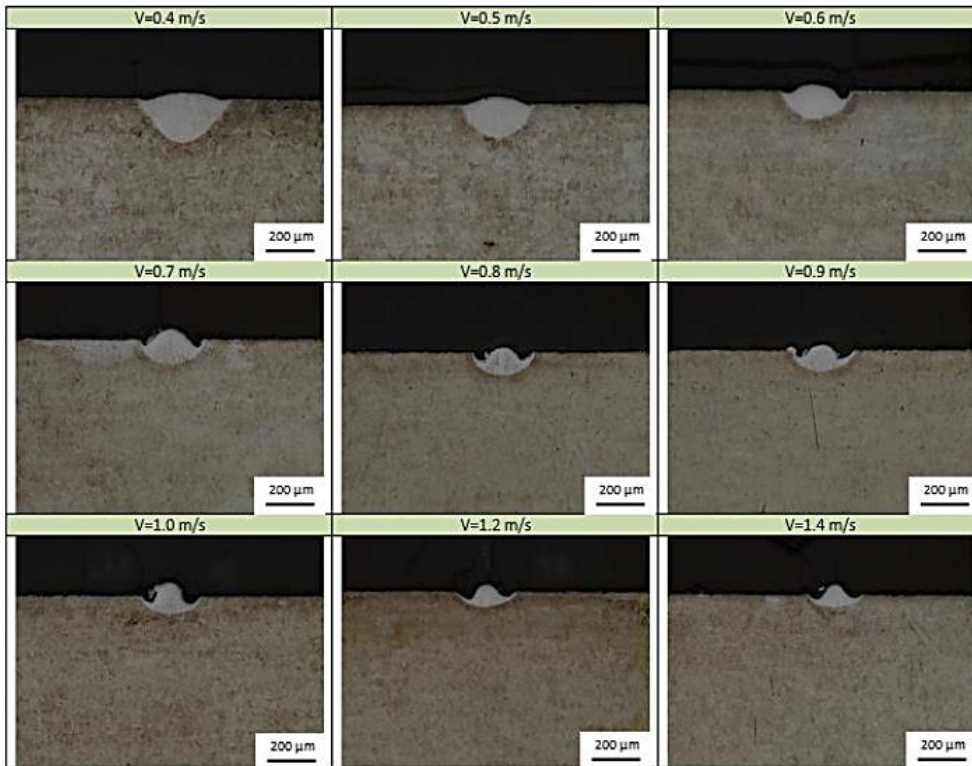


Laser power 200 W, scanning speed $V=0.8-2.4$ m/s, spot size $80\ \mu\text{m}$, laser power density $39.8\ \text{kW}/\text{mm}^2$

Laser power 300 W, scanning speed $V=1.2-2.8$ m/s, spot size $80\ \mu\text{m}$, laser power density $59.7\ \text{kW}/\text{mm}^2$



Laser power 900 W, scanning speed $V=0.4-1.4$ m/s, spot size $240\ \mu\text{m}$, laser power density $19.9\ \text{kW}/\text{mm}^2$



Laser power 1350 W, scanning speed $V=0.6-2.0$ m/s, spot size $240\ \mu\text{m}$, laser power density $29.8\ \text{kW}/\text{mm}^2$



Laser power 1800 W, scanning speed $V=0.8-2.4$ m/s, spot size $240\ \mu\text{m}$, laser power density $39.8\ \text{kW}/\text{mm}^2$



Laser power 2700 W, scanning speed $V=1.2-2.8$ m/s, spot size $240\ \mu\text{m}$, laser power density $59.7\ \text{kW}/\text{mm}^2$



Appendix V

South African Journal of Industrial Engineering November 2016 Vol 27(3) Special Edition, pp 210-218

EVALUATION OF SINGLE TRACKS OF 17-4PH STEEL MANUFACTURED AT DIFFERENT POWER DENSITIES AND SCANNING SPEEDS BY SELECTIVE LASER MELTING

N.W. Makoana^{1#}, H. Möller¹, H. Burger¹, M. Tlotleng¹ & I. Yadroitsev²

ARTICLE INFO

Article details

Presented at the 17th annual international conference of the Rapid Product Development Association of South Africa (RAPDASA), held from 2-4 November 2016 in Vanderbijlpark, South Africa

Available online 11 Nov 2016

Contact details

* Corresponding author
nmakoana@csir.co.za

Author affiliations

- 1 Council for Scientific and Industrial Research, National Laser Centre, Pretoria, South Africa
- 2 Department of Mechanical and Mechatronic Engineering, Central University of Technology, Free State, South Africa

The author was enrolled for a part-time MSc degree in the Department of Mechanical and Mechatronic Engineering, Central University of Technology, and is a contracted employee of the CSIR in Pretoria.

DOI

<http://dx.doi.org/10.7166/27-3-1668>

ABSTRACT

In Selective Laser Melting, the initial units produced are single tracks that overlap to create a single layer; from the sequence of layers, a 3D object is manufactured. The properties of the parts produced by SLM depend heavily on the properties of each single track and each layer formed by these tracks. This study evaluates the effect of processing parameters on the geometrical characteristics of single tracks manufactured from 17-4PH stainless steel powder. A single-mode continuous-wave ytterbium fibre laser was used to manufacture single tracks at laser powers in the range of 100-300 W with a constant spot size of ~80µm. The single tracks produced were subjected to standard metallographic preparation techniques for further analysis with an optical microscope. Deep molten pool shapes were observed at low scan speeds, while shallow molten pool shapes were observed at high scan speeds. At higher laser power densities, under-cutting and humping effects were also observed. The dimensions of single tracks processed without powder generally decrease with increasing scan speed at constant laser power. However, the geometrical features of the single tracks processed with powder revealed pronounced irregularities believed to be caused by non-homogeneity in the deposited powder layer.

OPSOMMING

Selektiewe lasersmelting produseer enkel bane wat mekaar oordek en vorm so 'n enkele laag. Daaropvolgende lae vorm dan 'n drie-dimensionele onderdeel. Die eienskappe van hierdie onderdeel word grootliks beïnvloed deur die eienskappe van elke baan en elke laag. Hierdie studie evalueer die effek van die prosesserings-parameters op die geometriese eienskappe van enkel bane wat van 17-4PH vlekvrystaal poeier vervaardig is. 'n Enkelmodus kontinue-golf ytterbium vesel laser is gebruik om die enkel bane te vervaardig. Die laser drywing het gewissel van 100 tot 300W met 'n konstante kolgrootte van ongeveer 80µm. Die enkel bane is dan aan standaard metallografiese voorbereidingsmetodes onderwerp sodat verdere analise met 'n optiese mikroskoop kon geskied. Die gesmelte poel vorms is bespeur teen lae skandeersnelhede, terwyl vlakgesmelte poel vorms by hoë skandeersnelhede gewaar is. By hoër laser drywingsdigtheid is ondersnyding en hobbelvorming waargeneem. Die dimensies van die enkel bane wat sonder poeier geprosesseer is, het oor die algemeen afgeneem met 'n toename in skandeersnelheid by konstante laserdrywing.

INTRODUCTION

Selective laser melting (SLM), also known as powder bed fusion (PBF) or direct metal laser sintering (DMLS), is an additive manufacturing process that uses a laser beam to melt powder particles in order to produce 3D structures layer-by-layer directly from a 3D CAD model. The CAD model is generated with computer software and then sliced into a finite number of layers. Based on this information, a computer-controlled laser beam selectively scans the powder bed according to a 2D cross-section of each layer in order to fuse the powder particles. The initial units produced are single tracks that create a single layer; from the sequence of layers a 3D object is manufactured [1]. The ability of this technology to create parts layer-by-layer means that complex geometries can be easily optimised and produced without the need for hard tooling. Forms can be created that would be impractical or unachievable in other processes. This technology is optimised for low-volume, high-value production, thus ensuring that the process is highly attractive for the aerospace and medical industries, among others. In the aerospace industry, part designs are optimised for low weight and high strength; thus SLM provides the design freedom that is missing from traditional manufacturing methods.

Current additive manufacturing processes have a number of limitations that inhibit widespread use of the technology in the aerospace industry [2]. This includes the processing time of the current state-of-the-art technology. The processing time is divided into primary and auxiliary process times. The primary time is mainly the time needed to melt each single layer, whereas operations like a lowering of the substrate and powder deposition are part of the auxiliary process time [3]. The main influencing variables of the primary process time are layer thickness, scanning speed, and hatch spacing.

According to Yadroitsev *et al.* [5], the properties of parts manufactured by additive manufacturing depend a great deal on the properties of each single track and each layer, and on the strength of the connections between them. Numerous factors (direct and indirect parameters) affect the SLM process. However, the principal factors that affect the SLM process are laser power, wavelength, spot size, scanning speed, hatch spacing, and powder layer thickness [6].

Stainless steel 17-4PH is a precipitation hardening alloy that is characterised by an outstanding combination of high strength, good corrosion resistance, and good mechanical properties up to 300°C. Because of these attractive properties, this alloy is widely-used in the aerospace industry to produce components that require high strength and good corrosion properties at high temperatures. Although the SLM parts of 17-4PH have been studied before, most published work focuses on the microstructure and the mechanical properties of 3D parts.

Averyanova *et al.* [11] investigated the effect of processing parameters on single tracks and single layers manufactured from 17-4PH, using the experimental design approach to a maximum laser power of 50 W and a constant spot size of $\varnothing 70 \mu\text{m}$. However, no work has been done to evaluate single tracks of 17-4PH processed at laser powers and spot sizes beyond these. Schleifenbaum *et al.* [4] and Yadroitsava *et al.* [6] highlighted that the application of high-power lasers and big spot size increases the build rate of SLM. Thus the aim of this study is to evaluate the geometrical characteristics of single tracks of 17-4PH steel processed at higher laser powers and bigger spot size.

MATERIALS AND METHODS

Powder material

Stainless steel 17-4PH powder supplied by EOS GmbH was used to conduct the experiments, with the nominal composition of the powder as follows: Cr 15.0-17.5%, Ni 3.0-5.0%, Cu 3.0-5.0%, Si 1.0% max, Mn 1.0% max, C 0.07% max, Nb and Ta 0.15% max, P 0.04% max, and S 0.03% max. The powder was gas-atomised, and most particles were found to have a high sphericity and smooth surfaces (Figure 1).

The particle size distribution was determined using Microtac Bluewave/S3500-SDC, a laser diffraction particle size analyser. The 10th, 50th, and 90th percentiles of equivalent diameters were $D_{10} = 26.3 \mu\text{m}$, $D_{50} = 35.5 \mu\text{m}$, and $D_{90} = 52.8 \mu\text{m}$. The substrates used in the experiments had a similar composition to that of the powder.

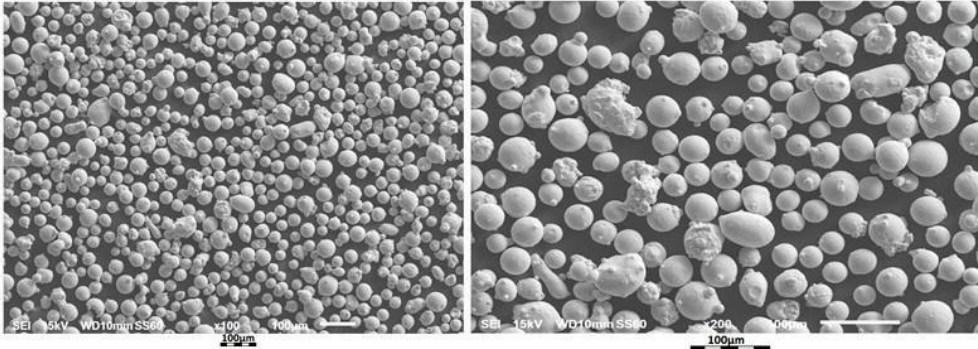


Figure 1: SEM micrographs of 17-4PH powder at different magnifications

Experimental procedure

An EOSINT M280 system equipped with a single-mode continuous-wave Ytterbium fibre laser, operating at 1075 nm wavelength and spot size of 80 µm, was used to produce single tracks at different laser powers and scan speeds (19.9-59.7 kW/mm²) on the 17-4PH substrate. The processing chamber was filled with a nitrogen protective atmosphere to minimise oxidation. Table 1 shows the parameters that were employed.

Table 1: Design of the experiments.

Laser power, W	100	150	200	300
Scanning speed, m/s	0.4	0.6	0.8	1.2
	0.5	0.8	1	1.4
	0.6	1	1.2	1.6
	0.7	1.2	1.4	1.8
	0.8	1.4	1.6	2.0
	0.9	1.5	1.8	2.2
	1.0	1.6	2	2.4
	1.2	1.8	2.2	2.6
	1.4	2	2.4	2.8

The powder layer thickness was kept constant at 50 µm. The single tracks manufactured were subjected to standard metallographic preparation techniques for further analysis with an optical microscope. Modified Fry's reagent (150 ml H₂O + 50 ml HCl + 25 ml HNO₃ + 1 g CuCl₂) was used to reveal the microstructure at the cross-sections of the single tracks.

RESULTS AND DISCUSSION

Laser melting of the substrate

The substrate was first scanned with the laser beam without powder in order to evaluate the effect of the processing parameters shown in Table 1 on the geometry of SLM tracks. There are two distinctive modes in laser processing: conduction and keyhole modes. The main difference between these two modes is the power density (power/spot size area) applied to the processing area. In conduction mode, the power density applied is insufficient to cause significant vaporisation; heat is absorbed from the laser beam through the top surface of the metal. In keyhole mode, however, the power density is high enough not only to vaporise material, but also to open a hole in the melt pool [7]. The conduction mode is also characterised by a semi-cylindrical shape, while the keyhole or penetration mode is characterised by a deep narrow shape [8].

According to Yadroitsava *et al.* [6], laser power density and scanning speed play a significant role in the geometry and shape of the molten pool. The laser power density defines the temperature gradient, and the scanning speed determines the time of laser-matter interaction. Figure 2 shows cross-sections of SLM tracks processed at different laser powers. It can be seen that increasing the laser power at a constant scanning speed (1.4 m/s) results in deeper penetration (21.0 - 75.4

μm) and increased material displacement and removal. This is in accordance with the increased energy input per unit area.

The morphology of the SLM tracks processed at a constant laser power was affected by the change in scanning speed. This is mainly because the laser-material interaction time, related to the heat input, is decreased when increasing scanning speed, thus affecting the energy input per unit length. At low laser power (i.e., 100 W), the keyhole mode and a deep molten pool was observed at a low scan speed of 0.4 m/s (Figure 3). Higher laser powers above 100 W and scanning speeds above 1 m/s result in defects, as shown in Figure 4. The SLM tracks processed at the highest laser power revealed a severe undercut and humping effect. Generally, the track width and penetration depth decreases as the scanning speed is increased at a constant laser power (Figure 5). This is in accordance with the decreased heat input at higher scanning speeds. This also implies that the amount of energy transferred into the material decreases as the scanning speed increases, thus reducing the size of the molten pool.

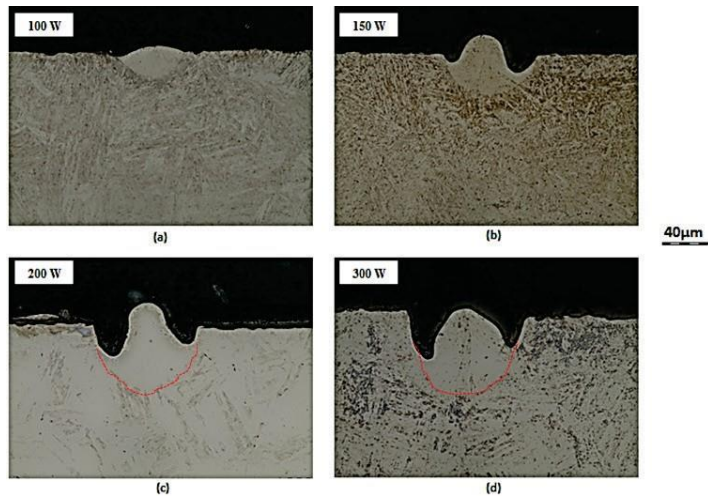


Figure 2: Cross-sections of SLM tracks processed at different laser powers and the same scanning speed (1.4 m/s)

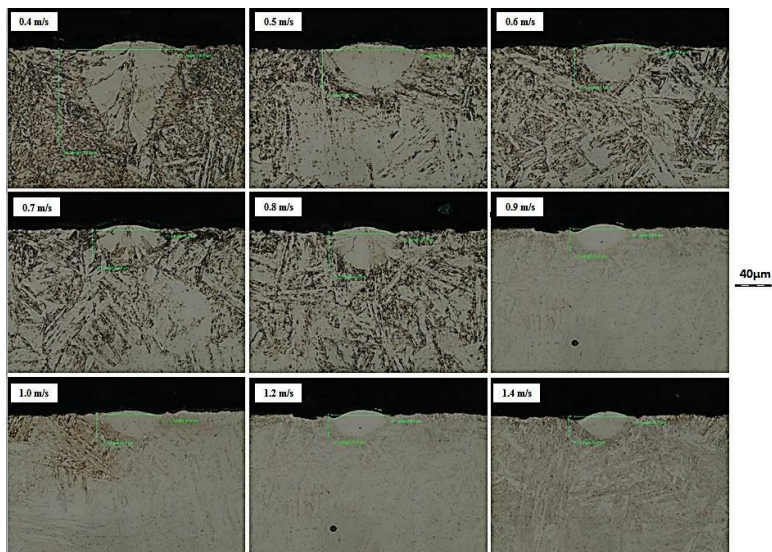


Figure 3: Cross-sections of SLM tracks processed at constant laser power (100 W) and varying scanning speeds

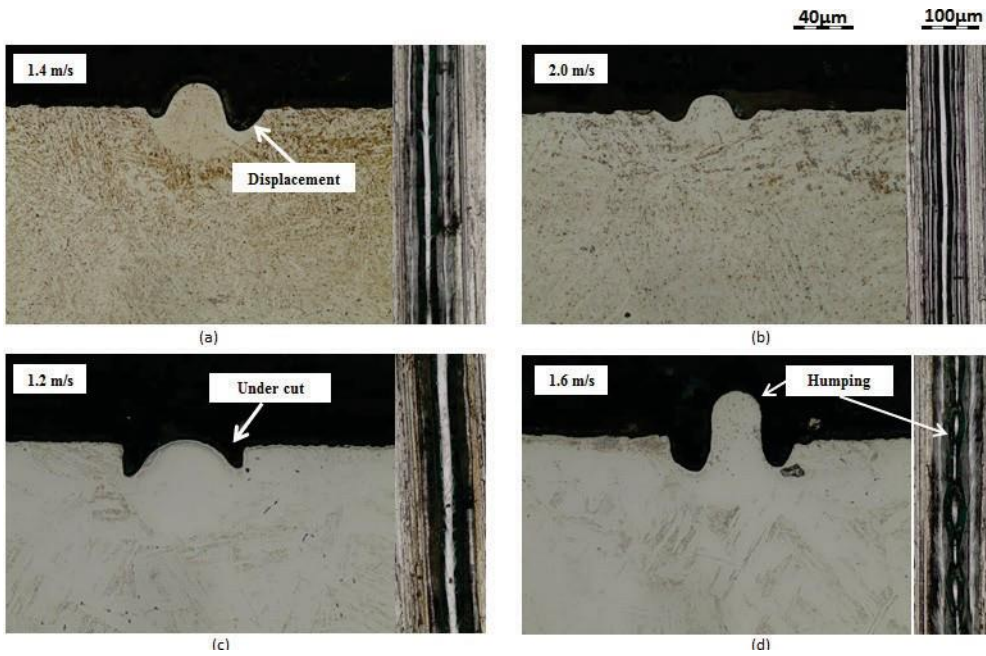


Figure 4: Cross-sections and top view images of SLM tracks processed at different laser powers and scanning speeds: (a) & (b) 150 W; (c) & (d) 300 W

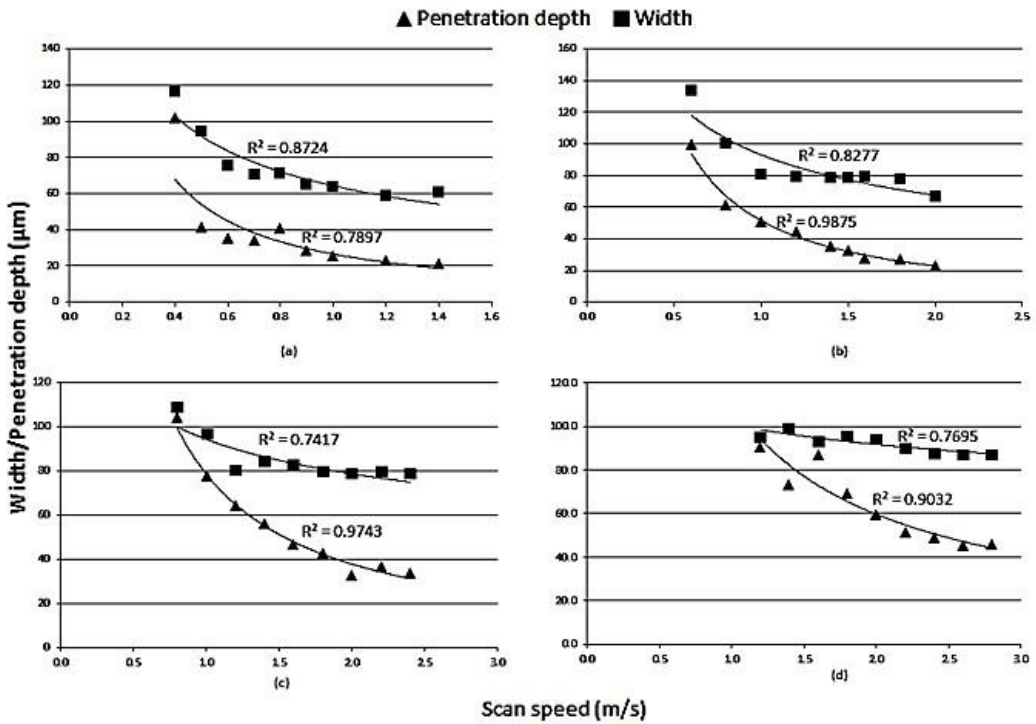


Figure 5: Width and penetration depth of SLM tracks processed at different laser powers of (a) 100 W; (b) 150 W; (c) 200 W; and (d) 300 W

Laser melting of powder

The essential operation of SLM is the laser beam scanning over the surface of a deposited powder layer in order to create a melt pool. As a result, the geometrical characteristics of single tracks processed from powder depend a great deal on the volume of material involved in the process [6]. In the second part of the experiments, the deposited powder layer was scanned with a laser beam in order to evaluate the geometrical characteristics of single tracks processed at different laser power and scanning speeds.

The effect of laser power on the geometrical characteristics of single tracks was analysed by comparing single tracks processed at a constant scanning speed (1.4 m/s). As in laser melting of the bulk material, increasing the laser power increases the energy input per unit area and thus increases the size of the molten pool (Figure 6). At a high laser power density, the input energy was also sufficient to cause significant vaporisation (Figures 6c & d).

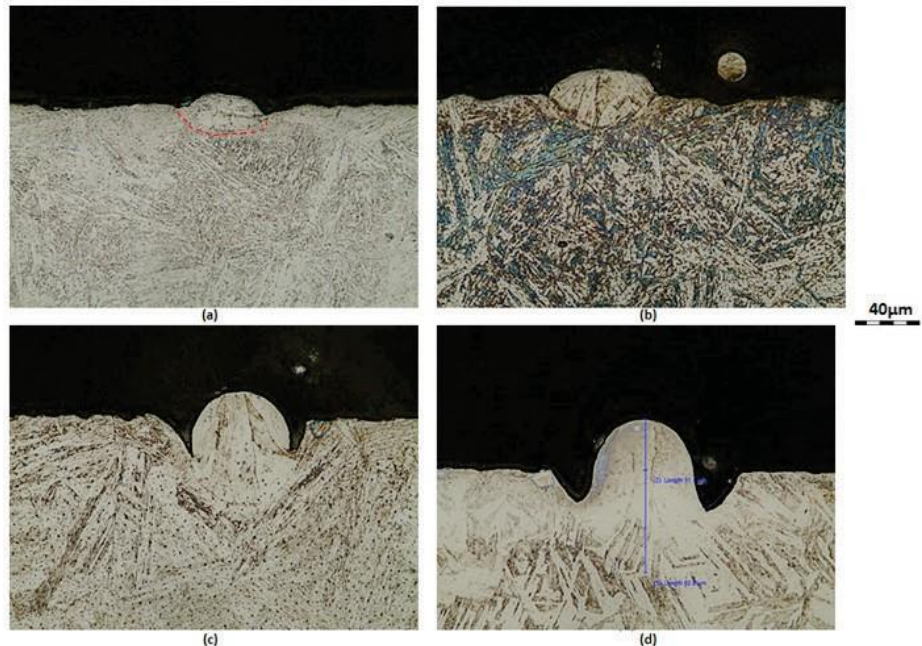


Figure 6: Cross-sections of single tracks processed at constant scanning speed and different laser powers: (a) 100 W; (b) 150 W; (c) 200 W; and (d) 300 W

The effect of scanning speed on the morphology of single tracks processed at constant laser power (100 W) was also evaluated (Figure 7). Generally, the track width and penetration depth decreases with increasing scan speed. The variation in track height was higher due to irregularities in the powder layer deposited on the substrate. A humping effect was observed at higher laser powers (>150 W) and scan speeds (>1.4 m/s). In addition, satellites were observed on the surface of some of the scanned tracks. Yadroitsev *et al.* [10] defined a satellite as a particle sticking to the surface of the scanned track that formed by spattering or partial re-melting of the powder in the peripheral zone of the laser spot. Re-melting of the sintered layers can help to reduce the number of satellites in 3D SLM objects.

The correlation between track dimensions and processing parameters (i.e., laser power and scanning speed) is graphically demonstrated in Figure 8. The coefficients of determination (R^2 values) for both track width and penetration depth decreases with increasing laser power, while the R^2 values for track height are low at all laser powers, except at 150 W where the track height is seen to increase with increasing scanning speed. These irregularities are believed to be caused by the non-homogeneity in the deposited powder layer and chaotic melt pool hydrodynamics at higher laser powers. The results also demonstrate that the layer thickness should be chosen according to the powder particle size

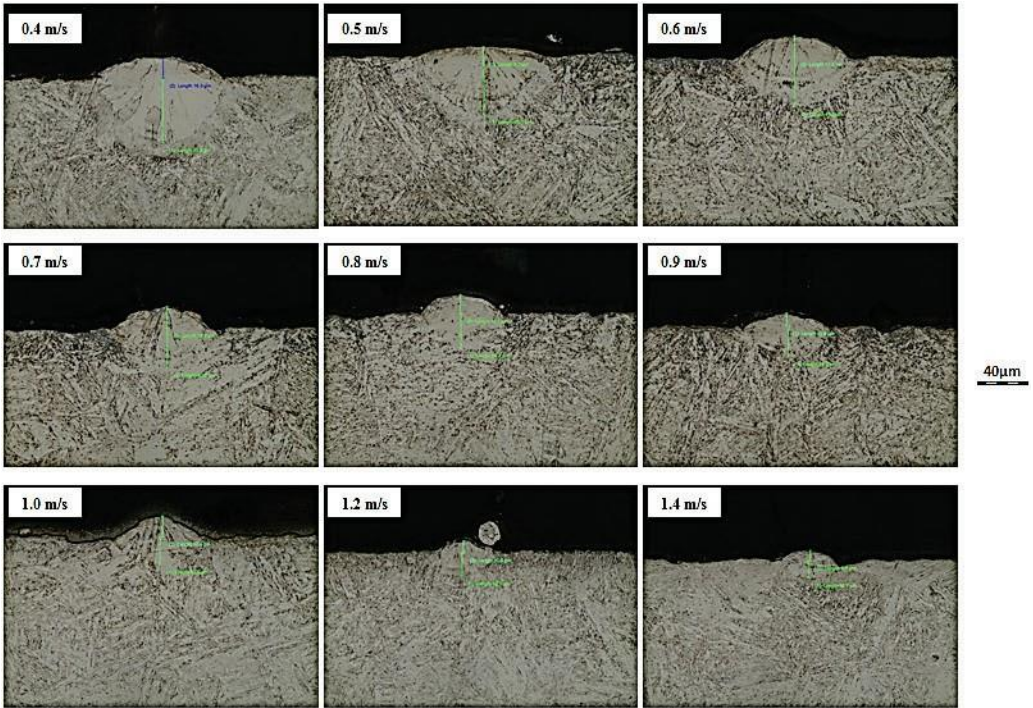


Figure 7: Single tracks processed at low laser power (100 W) and varying scanning speeds

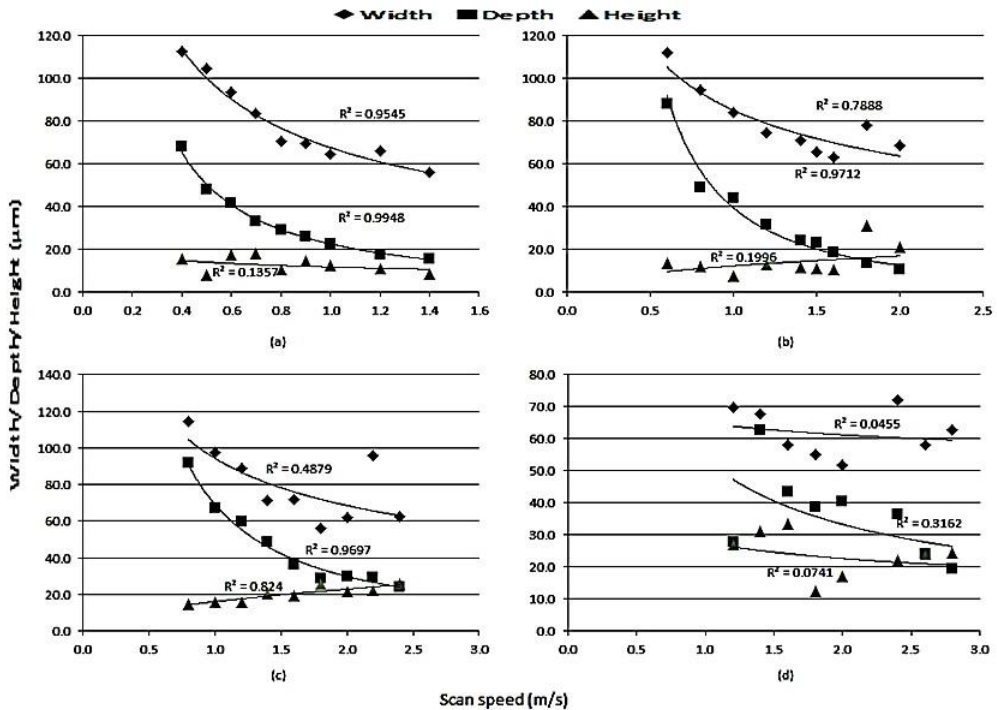


Figure 8: Track width, penetration depth, and height as a function of scanning speed at different laser powers: (a) 100 W; (b) 150 W; (c) 200 W; and (d) 300 W

The cohesion between successive layers plays an important role in the mechanical properties of SLM parts [6]. This is primarily dependent on the powder layer thickness and penetration depth. The penetration depth in this case refers to the depth of penetration into the substrate material/ previously sintered layer (re-melted depth). According to Kempen *et al.* [12], each synthesised layer must penetrate the layer below enough to successfully produce a consolidated single track. When the penetration depth is reduced at low laser power and high scan speeds, the chance of insufficient bonding between layers increases, while at high laser powers and low scan speeds, the deep molten pool and evaporation can provoke the formation of pores in the manufactured parts.

Therefore, our requirements for the SLM track to be included in the optimal process window are:

- The track must be continuous;
- The track must penetrate the previous layer enough to accomplish good cohesion of the layers (wetting of the layer underneath); and
- The track must be high enough to build up the part.

However, irregularities in the geometrical features of single tracks processed with powder make it difficult to draw any inferences about the optimal process window.

CONCLUSIONS

In this study, single tracks of 17-4PH steel processed at different laser powers and scanning speeds were evaluated. The results led to the following conclusions:

- 1) The dimensions (width and penetration depth) of single tracks processed with and without powder generally decrease with an increasing scan speed at a constant laser power;
- 2) Higher laser power densities provoke the formation of undercut and humping defects (with and without powder);
- 3) At constant laser power, keyholes with a deep molten pool shape were observed at low scanning speeds (with and without powder); and
- 4) Non-homogeneity in the deposited powder layer increases the variation in track dimensions (irregularities).

FUTURE WORK

Laser melting of powder should be repeated using fine powder ($D_{90} = 45 \mu\text{m}$), in order to improve the homogeneity of the deposited layer. It is believed that delivering a homogeneous layer will minimise irregularities in track morphology and track dimensions, and thus allow for the determination of an optimal process window.

An evaluation of single tracks processed at higher laser powers ($>900 \text{ W}$) and bigger spot size ($\varnothing 240 \mu\text{m}$) is needed. Laser power densities (laser power/spot area) should be maintained ($19.9\text{-}59.7 \text{ kW/mm}^2$) in order to make comparisons and identify the peculiarities of upscaling SLM of 17- 4PH steel.

ACKNOWLEDGEMENTS

This work was made possible by the support of the Central University of Technology and Aeroswift (collaborative work between the CSIR, Aerosud, and the Department of Science and Technology

REFERENCES

- [1] Yadroitsev, I. and Smurov, I. 2010. Selective laser melting technology: From the single laser melted track stability to 3D parts for complex shape. *Physics Procedia*, 5(2), pp. 551-560.
- [2] Keck, W. and Warner, M. 2016. *The significance of selective laser melting in commercial aircraft jet engine components*. University of Pittsburgh Swanson School of Engineering. Retrieved from <http://136.142.82.187/eng12/temp/papers/6236.docx>. (Accessed: 18 August 2016).
- [3] Matilainen, V., Piili, H., Salminen, A., Syvänen, T. and Nyrhila, O. 2014. Characterization of process efficiency improvements in laser additive manufacturing. *Physics Procedia*, 56(c), pp. 317-326.
- [4] Schleifenbaum, H., Diatlov, A., Hinke, C., Bültmann, J. and Voswinckel, H. 2011. Direct photonic production: Towards high speed additive manufacturing of individualized goods. *Production Engineering*, 5(4), pp. 359-371.
- [5] Yadroitsev, I., Gusarov, A., Ydroitsava, I. and Smurov, I. 2010. Single track formation in selective laser melting of metal powders. *Journal of Materials Processing Technology*, 210(12), pp. 1624-1631.

- [6] Yadroitsava, I., Els, J., Booyesen, G. and Yadroitsev, I. 2015. Peculiarities of single track formation from Ti6AL4V alloy at different laser power densities by selective laser melting. *South African Journal of Industrial Engineering*, 26(3), pp. 86-95.
- [7] Assuncao, E., William, S. and Yapp, D. 2012. Interaction time and beam diameter effects on the conduction mode limit. *Optics and Lasers in Engineering*, 50(6), pp. 823-828.
- [8] Walsh, C.A. 2002. *Laser welding – Literature review*. Materials Science and Metallurgy Department, University of Cambridge, England. Retrieved from http://www.msm.cam.ac.uk/phase-trans/2011/laser_Walsh_review.pdf. (Accessed: 22 August 2016).
- [9] Aboulkhair, N.T., Maskery, I., Tuck, C., Ashcroft, I. and Everitt, N.M. 2016. On the formation of AlSi10Mg single tracks and layers in selective laser melting: Microstructure and nano-mechanical properties. *Journal of Materials Processing Technology*, 230(2016), pp. 88-98.
- [10] Yadroitsev, I., Krakhmalev, P., Yadroitsava, I., Johansson, S. and Smurov, I. 2013. Energy input effect on morphology and microstructure of selective laser melting single track from metallic powder. *Journal of Materials Processing Technology*, 213(4), pp. 606-613.
- [11] Averyanova, M., Cicala, E., Bertrand, P. and Grevey, D. 2012. Experimental design approach to optimize selective laser melting of martensitic 17-4 PH powder: Part I – Single laser tracks and first layer. *Rapid Prototyping Journal*, 18(1), pp. 28-37.
- [12] Kempen, K., Thijs, L., Yasa, E., Badrossamay, M., Verheecke, W. and Kruth, J.P. 2011. Process optimization and microstructural analysis for selective laser melting of AlSi10Mg. In: *Proceedings of Annual International Solid Freeform Fabrication Symposium*, Texas, USA, pp. 484-495.

Appendix VI

Preliminary Investigation on Selective Laser Melting of 17-4PH Steel Using High laser Powers of up to 1500W

N.W. Makoana^{1,2}, H. Möller¹, D. Louw¹, & I. Yadroitsev²

¹Council for Scientific and Industrial Research, National Laser Centre, Pretoria, South Africa

²Department of Mechanical and Mechatronic Engineering, Central University of Technology, Free State, South Africa
nmakoana@csir.co.za

Abstract: High laser powers of up to 1500W were used to additively manufacture 17-4PH samples. Porosity was measured using quantitative image analysis technique, and all samples are fairly dense with a maximum of 0.42 percent porosity.

OCIS codes: (140.0140); (140.3390).

1. Introduction

Industrial applications of Additive Manufacturing (AM) platforms like Selective Laser Melting are still limited because of their long processing time. In an attempt to reduce the processing time, different techniques have been discussed and developed. One method is by utilizing high powered lasers with increased focused beam diameter in order to melt multiple layers at the same time [1]. Although 17-4PH stainless steel has been successfully manufactured by AM before, most of the machines utilised laser powers in the range of 200-400 W. The aim of this study was to investigate the processability of 17-4PH parts using higher laser powers of up to 1500W. This part of the study focused solely on measuring porosity.

2. Material and Methods

Stainless steel 17-4PH powder was used to conduct the experiments. The powder was gas-atomised, and most particles were found to have a high sphericity and smooth surfaces. Samples were manufactured using an in-house made AM set-up equipped with a multi-mode continuous wave Ytterbium fibre operating at a wavelength of 1071 nm and a focused laser beam diameter of approximately 240 μm . The energy densities used to manufacture the samples were varied between 100-185 J/mm^3 by changing the laser power, scan speed, and hatch spacing as shown in table 1. The formula used to calculate the energy density is shown in equation 1. The layer thickness was maintained constant at 50 μm . Samples produced were mounted and metallographically prepared using standard techniques. Images for each sample were taken using Olympus BX51M optical microscope equipped with Stream Essential software. For each sample, four images were taken at different locations to measure the percentage porosity using quantitative image analysis technique.

Table 1 –Processing parameters for sample manufacturing.

P (W)	1500	1250	1000	1500	1250	1000	1500	1250	1000
v (mm/s)	2500	2000	1500	2500	2000	1500	2500	2000	1500
h (mm)	0.12	0.12	0.12	0.096	0.096	0.096	0.072	0.072	0.072
$E_d(\text{J}/\text{mm}^3)$	100	104	111	125	130	139	167	174	185

$$E_d = P/(v \cdot h \cdot i) \quad (1)$$

where P is the laser power, v is the scanning speed, h is the scanning speed, and l is the layer thickness.

3. Results and discussion

Porosity is typically observed in AM parts and represents the most common defect, the degree of which can be altered via the laser processing parameters. The effect of energy density on porosity is graphically illustrated in

figure 1. It can be seen that the overall percentage porosity decreases with increasing the energy density, except at 139 J/mm³ where a noticeable increase in porosity is observed. The results also suggest that the samples are fairly dense, with a maximum of 0.42% porosity. The lowest porosity (i.e. 0.08%) is obtained with the energy density of 174 J/mm³. The corresponding micrographs of the samples are shown in figure 2. The black spots are pores that are created during the additive manufacturing process. Their distribution is fairly homogenous and can be formed due to several reasons such as decrease in solubility of the dissolved elements in the molten pool during cooling and solidification and evaporation of elements with a high vapour pressure [2]. Additionally, an insufficient surface quality can increase porosity as well. High roughness peaks and valleys that are formed after each layer can avoid the scraper to deposit a uniform powder layer, hence the energy density supplied may not be enough to melt the new layer completely since the depth of the powder in some regions might be thicker [3]. Non-homogeneity in the deposited powder layer as a result of imperfections or damaged scraper may also increase variation in porosity of the samples processed on the same substrate.

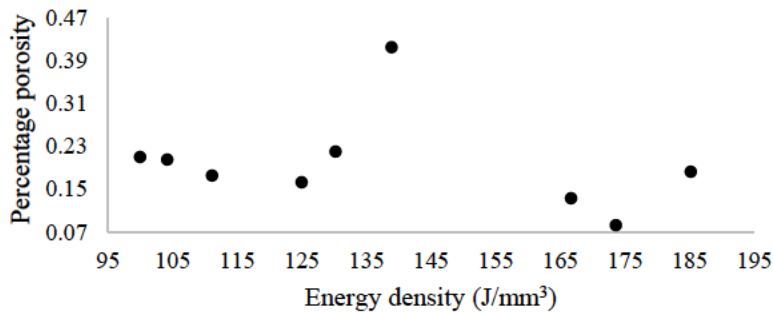


Figure 1 – Porosity versus energy density, data points are measured values of porosity from optical images on the side view

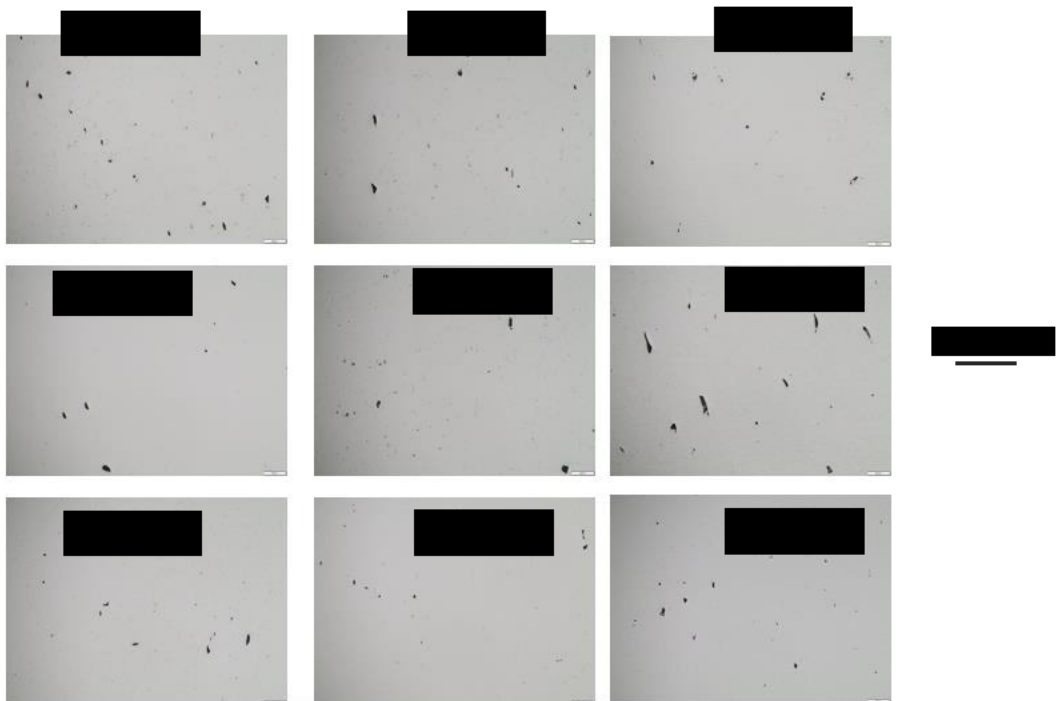


Figure 2 - Optical images showing porosity observed along the side view under various energy densities.

Conclusion

In this study we evaluated porosity in 17-PH samples that were manufactured at high laser powers of up to 1500W. Generally, the overall porosity decreases with increasing the energy density. All the samples revealed porosity levels of less than 1 percent. The lowest porosity of 0.08% was achieved at $174\text{J}/\text{mm}^3$. Within the parameters applied, all the samples are fairly dense with a maximum porosity of 0.42 percent. It was possible to process 17-4PH using high laser powers and increased beam size.

References

- [1]. Schleifenbaum, H., Meiners, W., Wissenbach, K. and Hinke, C., 2010. "Individualized production by means of high power Selective Laser Melting". *CIRP Journal of manufacturing science and technology*, 2(3), pp.161-169.
- [2] Kruth, J.P., Froyen, L., Van Vaerenbergh, J., Mercelis, P., Rombouts, M. and Lauwers, B., 2004. "Selective laser melting of iron-based powder". *Journal of Materials Processing Technology*, 149(1), pp.616-622.
- [3] Yasa, E. and Kruth, J.P., 2011. "Application of laser re-melting on selective laser melting parts". *Advances in Production Engineering and Management*, 6(4), pp.259-270.